Land-atmosphere Interaction: from Atmospheric Boundary Layer to Soil Moisture

Dynamics

by

Jun Yin

Department of Civil and Environmental Engineering
Duke University

Date:_____
Approved:

_____
John Albertson, Supervisor

_____
Amilcare Porporato

_____
Gabriel Katul

_____
J.R. Rigby

Dissertation submitted in partial fulfillment of
the requirements for the degree of Doctor of Philosophy in the Department of
Civil and Environmental Engineering in the Graduate School
of Duke University

2015

<u>ABSTRACT</u>

Land-atmosphere Interaction: from Atmospheric Boundary Layer to Soil Moisture

Dynamics

by

Jun Yin

Department of Civil and Environmental Engineering
Duke University

Date:_____
Approved:

_____
John Albertson, Supervisor

_____
Amilcare Porporato

_____
Gabriel Katul

_____
J.R. Rigby

An abstract of a dissertation submitted in partial
fulfillment of the requirements for the degree
of Doctor of Philosophy in the Department of
Civil and Environmental Engineering in the Graduate School of
Duke University

2015

# Abstract

Accurate modeling of land-atmosphere interaction would help us understand the persistent weather conditions and further contribute to the skill of seasonal climate prediction. In this study, seasonal variations in radiation and precipitation forcing are included in a stochastic soil water balance model to explore the seasonal evolution of soil moisture probabilistic structure. The theoretical results show soil moisture tends to exhibit bimodal behavior only in summer when there are strong positive feedback from soil moisture to subsequent rainfall. Besides the statistical analysis of soil moisture – rainfall feedback, simplified mixed-layer models, coupled with soil-plant-atmosphere continuum, are also used to study heat flux partitioning, cloud initiation, and strength of moist convection. Approximate analytical solutions to the mixed-layer model are derived by applying Penman-Monteith approach, which help explain the roles of equilibrium evaporation and vapor pressure deficit in controlling the diurnal evolution of boundary layer. Results from mixed-layer model also define four regimes for possible convection in terms of cloud/no-cloud formation and low/high convection intensity. Finally, cloud-topped mixed-layer model is developed to simulate the boundary-layer dynamics after the cloud formation, when the evaporative and radiative cooling other than surface heat flux may significantly contribute to the growth of the boundary layer.

To Panda Express:

Consistently receiving inspirational words from your fortune cookies makes me believe that I am capable of finishing this PhD study.

# Contents

# List of Tables

# List of Figures

# Acknowledgements

# 1. Introduction

Land-atmosphere interaction, through precipitation recycling and/or through atmospheric boundary-layer dynamics, could induce persistent weather conditions such as prolonged droughts or abnormally floods (Savenije 1995; Findell and Eltahir 1997, 2003b; D'Odorico and Porporato 2004; Dominguez et al. 2006; Dirmeyer and Brubaker 2007; Muller et al. 2009; Yin et al. 2014). When further coupling with ocean-atmosphere forcing, the interaction between atmospheric dynamics and surface hydrology, could play an important role in the local climate system and has received significant research attention (Betts et al. 1996; Koster et al. 2004; Guo et al. 2006; Koster et al. 2006; Schubert et al. 2008; Ferguson et al. 2010; Stéfanon et al. 2013). The research efforts on land-atmosphere interaction not only help understand the important feedbacks in the climate system but also help identify radiative forcing due to human activities such as land use and land cover change, which are essential to the study of climate change (Pinty et al. 1989; Pitman 2003; Pielke et al. 2007; Pielke et al. 2011; Mahmood et al. 2014).

However, the studies of land-atmosphere interaction, either through weather prediction models or from observations, show great uncertainties in terms of land-atmosphere coupling strength, soil moisture – rainfall feedback, and boundary-layer dynamics on convective rainfall (Findell and Eltahir 2003a, 2003b; Koster et al. 2003; Koster et al. 2004; Koster et al. 2006; Alfieri et al. 2008; Taylor et al. 2012). For example, while positive feedback from soil moisture to subsequent convection rainfall seems

possible due to the local precipitation recycling and the accumulation of low-level moist static energy (Rodriguez-Iturbe et al. 1991; Entekhabi et al. 1992; Juang et al. 2007a; Siqueira et al. 2009), drier soils also likely trigger convective rainfall in certain conditions (Gentine et al. 2013; Stéfanon et al. 2013). One of reason for the uncertainties in the data analysis from observations is that the relative weak signal of soil moisture to rainfall feedback is embedded in the strong signal of rainfall impacts on surface hydrology (Findell and Eltahir 1997; Salvucci et al. 2002; Yin et al. 2014). The uncertainties in the model simulations for the land-atmosphere interaction, especially from numerical weather prediction models, are associated with the complex modeling structure, which will always miss some high-dimensional components and thus cannot well interpreting the land-atmosphere coupling (Porporato 2009; Zhang et al. 2013). To overcome the first limitation in data analysis, accurate and abundant observational data and advanced statistical methods may be required to diagnose the soil moisture - rainfall feedbacks (Dirmeyer and Brubaker 2007; Findell et al. 2011). For the second limitation in climate modeling, simplified hydro-climatic models, which though could not make precise weather forecasting, can be used to interpret the essential physics in the land-atmosphere interaction (Ek and Mahrt 1994; Lyons 2002; Findell and Eltahir 2003b; Porporato 2009; Konings et al. 2010; Rigby et al. 2015).

Following this guideline, the work in this thesis studies the land-atmosphere interaction from both data analysis for soil moisture – rainfall relationship and modeling

boundary-layer dynamics using simplified mixed-layer models. Chapter 2 investigates the seasonal variation of radiation and precipitation forcing from soil moisture and precipitation observational data in Illinois to explore the evolution of soil moisture probabilistic structure. This study, though empirical, provides a clear perspective view of the general effects of seasonal variation of land-atmosphere interaction intensity on surface hydrology and local climate. After this empirical analysis, the following chapters focus on mixed-layer models, which have been extensively in the study of land-atmosphere interaction. Chapter 3 tries to find approximate analytical solutions, which allow us to identify the energy and moisture balances on the growth of the boundary layer in closed form. This analytical solutions help understand the roles of equilibrium evaporation and vapor pressure deficit in controlling the heat flux partitioning and boundary-layer dynamics. Chapter 4 continues to use the mixed-layer model to investigate the timing of cloud initiation and intensity of convection. The analysis explains that earlier emergence of cloud does not necessary indicate the convection is also stronger. Although the cloud-free mixed-layer model as used in chapter 3 and 4 can be efficient to model the boundary-layer dynamics and analyze the land-atmosphere interaction, it becomes invalid after the formation of the convective cloud. For this reason, chapter 5 begins to study the cloud-topped mixed-layer models and focus on the impacts of evaporative and radiative cooling on cloud-top entrainment rate. When the entrainment rate theoretically approaches infinity, the boundary layer becomes unstable,

leading to either cloud dissipation or deep convection. Final conclusions are

summarized in chapter 6.

# 2. Interplay of climate seasonality and soil moisture-rainfall feedback

This chapter is based on the article: Yin, J., Porporato, A., & Albertson, J. (2014). Interplay of climate seasonality and soil moisture-rainfall feedback. Water Resources Research, 50(7), 6053-6066.

## *2.1 Introduction*

Land-atmosphere interaction plays an important role in the climate system and has therefore received significant research attention. Through precipitation recycling, soil moisture may significantly contribute to the rainfall, especially in continental regions (Rodriguez-Iturbe et al. 1991; Entekhabi et al. 1992; Dominguez et al. 2006). Soil moisture may also interact with the atmosphere by controlling the partitioning sensible and latent heat fluxes thus influencing the dynamics of atmosphere boundary layer and the triggering of convective precipitation (Eltahir 1998; Santanello et al. 2005; Santanello et al. 2009; Siqueira et al. 2009; Konings et al. 2010). The long-term effect of such land-atmosphere interactions is the emergence of persistence and preferential states in soil moisture and hydro-climatic conditions, often reflected in a bimodal distributions of soil moisture and persistent hydro-climatic patterns (Rodriguez-Iturbe et al. 1991; D'Odorico and Porporato 2004; Porporato and D'Odorico 2004; Daly and Porporato 2007).

While the existence of land-atmosphere interaction and feedbacks is expected from a physical point of view, its presence is hard to detect in real data. The reason for this is that the strength of the land-atmosphere interaction is dominated by the strong effect of precipitation on soil moisture, while the opposite effect of soil moisture on precipitation is less direct and embedded within the complex meteorological and climatic fluctuations. As a result, while a state of precipitating atmosphere has a definite impact (increase) on soil moisture, it is likely, albeit uncertain, that higher soil moisture level will induce more subsequent precipitation. As a result, detection of land-atmosphere interactions from observations suffers from issues of causality detection (causality detection is especially hard in the presence of relatively weak and probabilistic interactions), as it is difficult to detect whether a certain soil moisture-rainfall temporal pattern is resulting from land-atmosphere feedback or simply due to an external rainfall forcing which produces same soil moisture evolution. Thus, in the absence of controlled, manipulative experiments on the land-atmosphere interaction, as would be achieved for example through large scale irrigation, the detection of land-atmosphere interaction has to rely on model analyses (either with detailed climate and hydrologic models or with simplified models, as done here) and currently remains an interesting and open research field (Findell and Eltahir 1997; Salvucci et al. 2002; Koster et al. 2004).

Rodriguez-Iturbe et al (1991); D'Odorico and Porporato (2004); Porporato and D'Odorico (2004); Daly and Porporato (2007) used relatively simple stochastic models to capture the propagation of hydrologic fluctuations of rainfall into soil moisture and plant system with the assumption of a soil moisture dependence of rainfall frequency. The analytical solutions of the stochastic model showed bimodal probability density functions (pdf) of soil moisture in agreement with field observations in the state of Illinois, suggesting the possible existence of positive cause-and-effect relationship between initial soil moisture and subsequent rainfall (D'Odorico and Porporato 2004). Because of mathematical difficulties, these stochastic models have been solved for steady-state conditions, thus representing averaged conditions during a growing season, in which potential evapotranspiration and feedback strength are assumed to be time-invariant. While this assumption helped explain the overall tendency of land-atmosphere interaction to induce preferential states, it neglects the dynamics of soil moisture seasonal transition and the important contribution from spring soil moisture to the subsequent summer precipitation in seasonal regimes.

Seasonal variability in rainfall and potential evapotranspiration, embedded within intra-seasonal and inter-annual rainfall variability leave a strong signature on the local hydrology, which may mask and interact with itself to shift the mode of soil moisture distribution, which may then combine to form a bimodal distribution for a period over wet and dry seasons (Teuling et al. 2005). This combined bimodal

distribution is completely driven by external forces and may be confused with the feedback-driven soil moisture preferential states. Moreover, the feedback from soil moisture, through the interaction with atmosphere boundary layer, primarily influences convective rainfall frequency (Findell and Eltahir 2003; Konings and Katul 2010). The deep convection links to the convective available potential energy (CAPE) which is seasonally varied and typically stronger in summer when higher solar radiation is able to intensify the land-atmosphere interaction and reduce the atmospheric stability. This interaction among the components of climate system indicates the strength of soil moisture-rainfall feedback may also have seasonality which might be consistent with the variation of solar radiation. The interplay of climate seasonality and land-atmosphere interaction may control the transition of soil moisture distribution between unimodality and bimodality and modeling this transition may further help understand climate persistence and the existence of soil moisture-rainfall feedback.

In this study, we follow the approach of D'Odorico and Porporato (2004) and Porporato and D'Odorico (2004) and model the effects of land-atmosphere interaction as a linear relationship between soil moisture and subsequently rainfall frequency. This soil moisture-rainfall feedback is assumed to be stronger in warmer seasons and weaker in colder seasons, in accordance with the seasonally varied CAPE. We focus on the seasonal variations of soil moisture and rainfall frequency by presenting their evolution of mean values and the whole distribution as well. We analyze the influence of land-

atmosphere interaction on rainfall seasonality and identify the control of the feedback on soil moisture preferential states and climate persistence.

## *2.2 Climate Seasonality*

To study the climate seasonality and the strength of soil moisture - rainfall feedback, we focus on the well-studied data from Illinois where long-term biweekly soil moisture observations are available along with other hydro-climatic data. The soil moisture data from 1981 to 2004 at 19 stations across the state of Illinois are available from the Illinois State Water Survey (ISWS) Water and Atmospheric Resources Monitoring Program (WARM). Companion precipitation data for each of the station are also available from the National Climatic Data Center (NCDC).

D'Odorico and Porporato (2004) showed that the average rainfall frequency ($\lambda$) has a relatively strong correlation with its antecedent soil moisture conditions (*s*) in summer and can be modeled as a linear function ($\lambda$ =*as+b*). However, it is likely that this dependence becomes weak outside the summer season, when the intensity of land-atmosphere interaction tends to decline.

To explore this effect we repeated and updated the analysis of D'Odorico and Porporato (2004), extending it to all four seasons. The results, presented in Figure 1, show the relationship between soil moisture averaged across 19 stations throughout the Illinois and the subsequent rainfall frequency in Peoria. The soil moisture sample data

are grouped into 8 bins, each of which contains more than 5% of the sample data and thus the corresponding average rainfall frequency could well represent the rainfall condition. We verified that changing binning does not change the general shape of the seasonal variation of rainfall frequency and depths, reported in Figure 2. Based on these results, the average rainfall depth does not seem to change seasonally, while average rainfall frequency is a strongly seasonal quantity which will be modeled as

$$\lambda(s,t) = a(t)s + b(t),$$ (1)

where the periodic coefficient $a(t)$ may be thought to be related to the soil moisture – rainfall feedback strength, which is higher when rainfall is triggered more frequently under the same soil moisture condition, while the coefficient b represents rainfall events that are not affected by the feedback. Since the feedback from soil moisture primarily influences convective rainfall frequency, one could imagine that $a(t)$ is linked to convective rainfall, while the constant b to frontal rainfall.
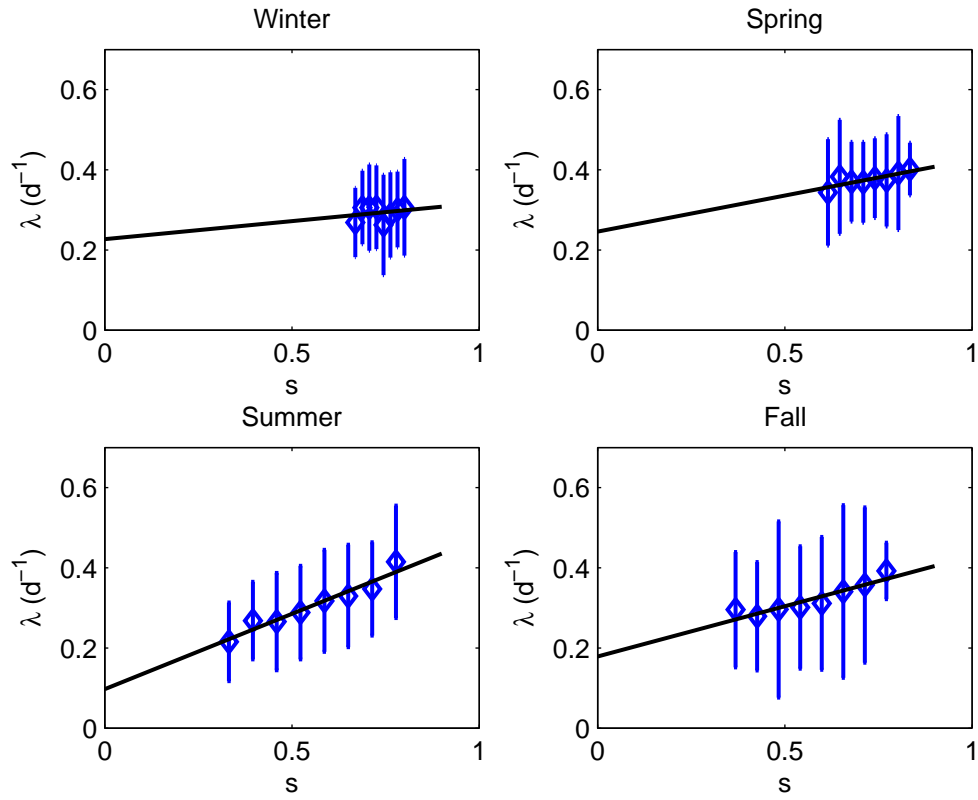
**Figure 1: Relationship between soil moisture (averaged over top 50cm and across 19 stations throughout Illinois) and rainfall frequency dependence at Peoria in winter (DJF), spring (MAM), summer (JJA), and fall (SON). The error bars represent one standard deviation of the rainfall frequency within each bin.**
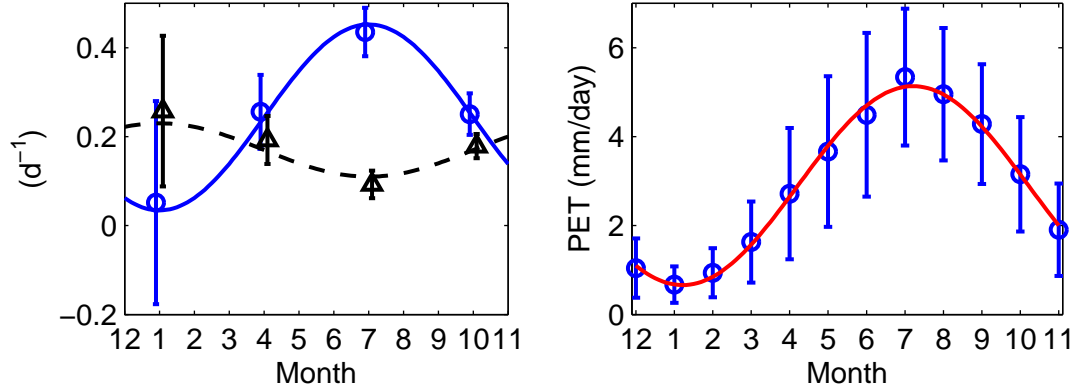
**Figure 2: (Left) Parameters from linear relationship between soil moisture and rainfall frequency in each season. Circles and triangles represent coefficients *a*(*t*) and b(t) regressed in Figure 1, error bars represent one standard deviation of the estimates; Solid and dash lines are the corresponding fitted functions. (Right) Seasonal variation of PET. Circles represent PET from the data in Peoria Illinois averaged in each month and solid line is the fitted sine function.**

The seasonal variation of the feedback strength is then simply modeled as a sine function which peaks in July and the non-feedback part of rainfall frequency (coefficient *b*) is kept as a constant (Figure 2 Left). Such dependencies capture the primary influence of climate seasonality on the intensity of land-atmosphere interaction.

Potential evapotranspiration (PET) is controlled by radiation and atmospheric temperature as defined by Priestley and Taylor (1972),

$$PET = \alpha \frac{\Delta}{\Delta + \Gamma} Q \times \frac{1}{\rho_w L_v}, \tag{2}$$

where $\alpha$ is a coefficient which usually is about 1.26, $\Delta$ is the temperature-dependent slope of saturation vapor pressure, $\Gamma$ is the psychrometric constant, $L_v$ is the latent heat of vaporization, $\rho_w$ is water density, and $Q$ is the net available radiation. PET thus

12

varies seasonally according to radiation and temperature. These are the main drivers of transpiration, boundary-layer growth, and the subsequent potential triggering of convective precipitation. We estimate PET with (2) and the data from Peoria, Illinois (1989 to 2012, ISWS WARM program). Based on the resulting monthly averaged PET, plotted in Figure 2 (right), we decided to model PET as a sine function, similarly to the SMRF strength parameter ($a(t)$) in Figure 2 (left). This similarity is also consistent with our conjecture that the strength of the SMRF is indeed related to the available energy driving evaporation and the atmosphere boundary layer (ABL) growth.

## 2.3 Stochastic SMRF model

To analyze theoretically the interplay between seasonal forcing and SMRF, we extend the stochastic soil moisture model with state-dependent average rainfall frequency, proposed by D'Odorico and Porporato (2004) and Porporato and D'Odorico (2004), to include seasonal PET forcing and the seasonally varying form of $\lambda(s)$. The stochastic component in this model captures the uncertainties of the atmospheric circulation, while the deterministic component can be used to model the average hydro-climatic processes over a large spatial area. In this model, the soil water balance at the daily time scale within the root zone ($Z_r$) is expressed as,

$$nZ_r \frac{ds}{dt} = P(s,t) - ET(s,t) - L(s) , \qquad (3)$$

where, $s$ is relative soil saturation, $n$ is the porosity, $P$ is rate of rainfall infiltration, $ET$ and $L$ are evapotranspiration and deep infiltration, respectively, which are modeled as

$$ET(s,t)+L(s,t)=\begin{cases} E_{max}\dfrac{s-s_w}{s*-s_w} & s_w \le s \le s* \\ E_{max} & s* < s \le s_{fc} \\ E_{max}+K_s\dfrac{\exp[\beta(s-s_{fc})]-1}{\exp[\beta(1-s_{fc})]-1} & s_{fc} < s \le 1, \end{cases} \qquad (4)$$

where $s*$ is the onset of plant water stress, $s_w$ is wilting point, $s_{fc}$ is field capacity, $K_s$ is the

saturated hydraulic conductivity, $\beta$ is a parameter of the soil moisture retention curve

(Laio et al. 2001) and $E_{max}$ is the evapotranspiration for the subject vegetation in well-

watered conditions. The effects of leaf area index ($\xi$) and PET are incorporated into $E_{max}$

(Al-Kaisi et al. 1989),

$$E_{max} = [1-\exp(-c\xi)]PET, \qquad (5)$$

where, the appropriate values for parameter $c$ and the leaf area index for Illinois can be

found in Al-Kaisi et al. (1989) and Teuling et al. (2005). $E_{max}$ is controlled by radiation as

in equation (2) and is one of the primary external climatic forces determining the

intensity of SMRF along with the average rainfall frequency parameter $a(t)$. Rainfall

occurrence is modeled as a marked Poisson process with arrival rate (i.e., average

frequency) $\lambda(s,t)$, which depends on both soil moisture and time. The rainfall depth is

assumed to be an exponentially distributed random variable with stationary mean depth

equal to $nZ_r/\gamma$.

Under the above assumptions, the equation for the temporal evolution of the soil

moisture probability density function $p(s,t)$ is (Porporato and D'Odorico 2004;

Rodríguez-Iturbe and Porporato 2005),

14

$$\frac{\partial p(s,t)}{\partial t} = \frac{\partial}{\partial s}[p(s,t)\rho(s,t)] - \lambda(s,t)p(s,t) + \int_0^s \lambda(z,t)p(z,t)b(s-z;z)dz \tag{6}$$

where, $\rho(s,t) = (L+ET)/nZ_r$, and

$$b(y,s) = \gamma \exp[-\gamma y] + \delta(y-1+s)\int_{1-s}^{\infty} \gamma \exp[-\gamma u]du$$

where $\delta(\cdot)$ is the Dirac delta function. Equation (6) cannot be solved analytically due to the time varying coefficients. In the following sections we will study its behavior by employing suitable analytical approximations and numerical simulations.

## *2.4 Dynamics of Mean soil moisture and rainfall frequency*

Mean soil moisture and rainfall frequency, defined as the expectation values at anytime of a typical year, will show the seasonal pattern of the hydro-climatic dynamics.

With seasonally varied feedback strength and PET as in Figure 2 and other soil property parameters in D'Odorico and Porporato (2004), pdf of soil moisture evolution for several years is numerically solved with certain arbitrary initial condition. This initial condition is finally forgotten after a few months due to the relatively short memory of soil moisture. The solution repeats each year in accordance with the periodical forces from the seasonally varied PET and feedback strength.

Mean soil moisture in a one-year period is calculated from the solution of pdf and shown in Figure 3. Soil is wet in winter and dries down in summer which could be partially explained by the seasonal variation of PET. Higher PET in summer is possible

to take away more water and keep the soil dry. The dry soil is then recovered and back into wet condition in winter due to the relatively lower evapotranspiration. Mean rainfall frequency can be simply calculated from the mean soil moisture by equation (1) due to its linearity. As shown in Figure 3, mean rainfall frequency rises in summer mainly due to the increasing strength of soil moisture feedback. However, these two increasing speeds are not completely synchronized and mean rainfall frequency reaches maximum value before feedback strength peaks. Abundant soil water storage in spring is available for precipitation recycling and convective rainfall is triggered more frequently. The same situation happens in fall when feedback strength decreases more drastically than mean rainfall frequency due to the gradually accumulated soil water which is again ready for the land-atmosphere interaction. This pattern of rainfall frequency, shifted by soil moisture-rainfall feedback, is consistent with the rainfall pattern in Illinois which peaks in late spring and gradually decreases the following summer. In this respect, the observed rainfall seasonality is not exclusively controlled by external climate forces but also influenced by internal land-atmosphere interaction.
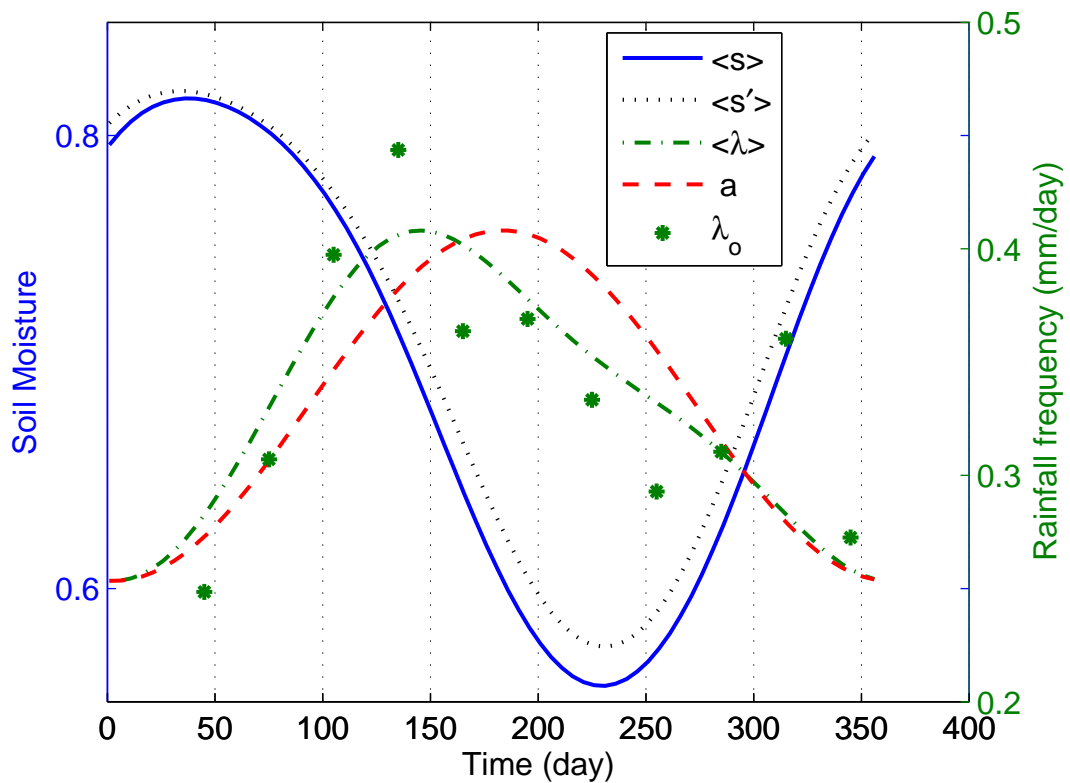
**Figure 3. Seasonal variation of mean soil moisture and rainfall frequency.**
**Solid line is for modeled soil moisture ($\langle s \rangle$), dash-dot line is for modeled average**
**rainfall frequency ($\langle \lambda \rangle$), and dash line is the parameter *a* linearly scaled into the**
**range of mean soil moisture. As a comparison, dotted line is the soil moisture ($\langle s' \rangle$)**
**from the non-feedback model simulation when average rainfall frequency is**
**independent of soil moisture but has the same rainfall seasonality as $\langle \lambda \rangle$. Star points**
**are observed rainfall frequency ($\lambda_o$).**

Besides the mean values of these climate variables, their full distribution may

further present the potential modality which otherwise cannot be viewed.

## 2.5. Emergence of soil moisture bimodal behavior

The emergent of a dry and a wet mode in the soil moisture pdf will be symptoms of preferential states and the transition from unimodal to bimodal will be indication of a stochastic transition to a regime dominated by land-atmosphere feedbacks.

The soil moisture pdf evolution in a one-year period is plotted in Figure 4, illustrating the pdf shape variation in each season. As shown in inset B-B, the pdf of soil moisture is unimodal in spring due to the weak feedback strength. Later in the summer, the feedback becomes strong enough to induce bimodal distribution of soil moisture as presented in inset A-A. Eventually, the distribution turns back into unimodality when the feedback strength fades away in the following winter. The thick solid lines in Figure 4 are the local maxima of pdf, which clearly split into two in summer and then joins back in late fall and winter.
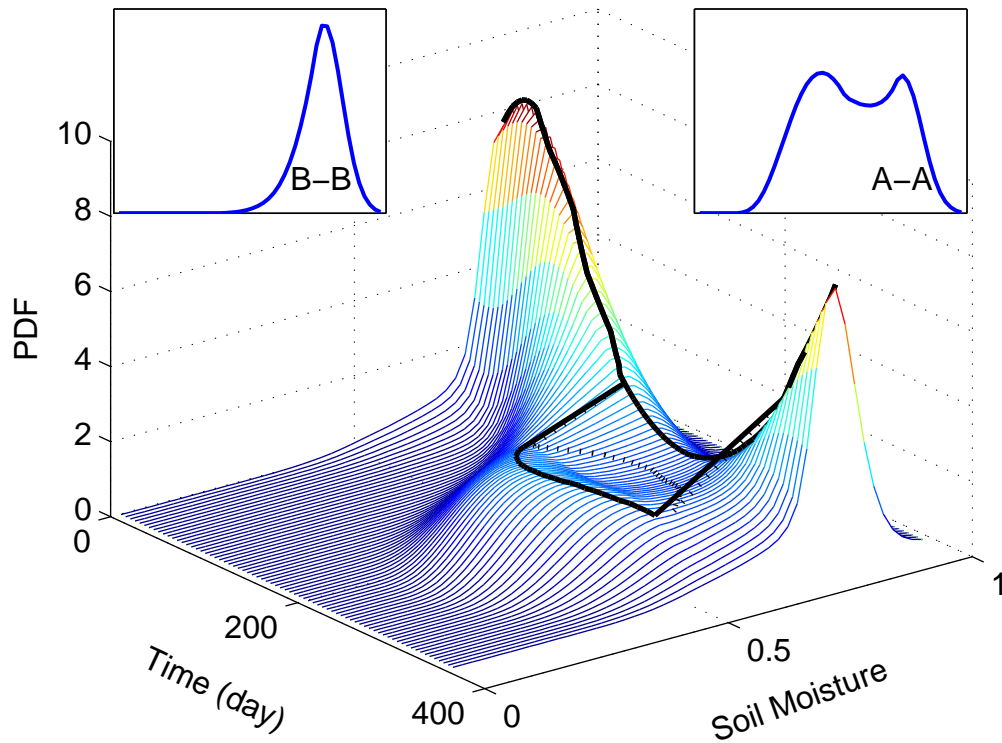
**Figure 4. PDF of soil moisture from the feedback model simulation in 3D plot (top) and contour plot (bottom). Thick solid lines and thick dotted lines are local maxima and minima of PDF at the corresponding time. Insets A-A and B-B are the soil moisture PDF at day 250 and day 100, respectively.**

To isolate of the effect of soil moisture-rainfall feedback, it is interesting to investigate the pdf when rainfall feedback is excluded and average rainfall frequency is only time-dependent. For comparison, this time-dependent average rainfall frequency was assumed to be the same as the rainfall seasonality from the feedback model as in Figure 2. Solutions of this non-feedback model are shown in Figure 5. The soil moisture distribution is unimodal most of the time except at spring-to-summer and summer-to-fall seasonal transition time, when the soil moisture is likely to experience sharp wet-to-

19

dry and dry-to wet shift. Intersection A-A and B-B, typically representing spring and summer pdf, are clearly unimodal.

The seasonal variation of rainfall exclusively from external forces in this non-feedback model can shift soil moisture mode, which may then combine to form a bimodal distribution as explained in Teuling et al (2005). To test this type of bimodality, pdf from May to September are averaged and presented in the inset MJJAS in Figure 5. This overall pdf, showing soil moisture preferential states, is completely driven by external climate forces and is accounted for by the extreme wet mode in late spring and extreme dry mode in early fall. This bimodal distribution is clearly different from the solution in the feedback model in Figure 4. The interplay of climate seasonality and soil moisture-rainfall feedback is able to maintain bimodal behavior of soil moisture for the whole warm seasons, while climate seasonality without the feedback only shift the mode of unimodal soil moisture distribution.
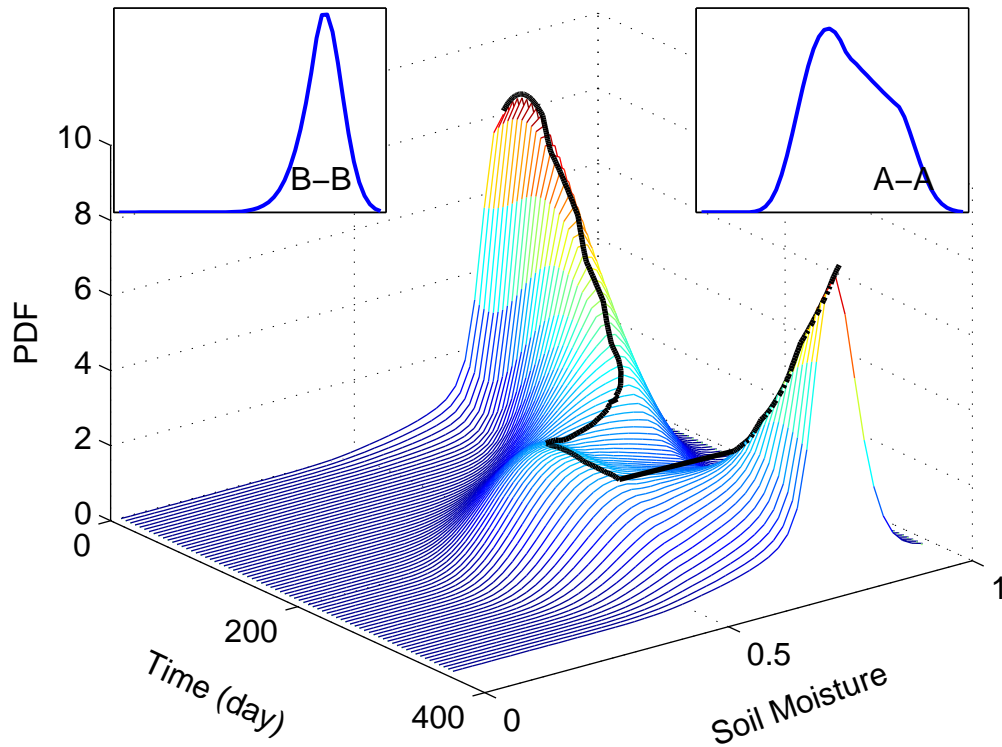
**Figure 5. As in Figure 4, but for the non-feedback model.**

## *2.6. Theoretical transient Analysis of mean trajectories.*

The stochastic representation of rainfall introduces noise into the water balance

equation (3) and thus the soil moisture is modeled as a random variable. While the soil

moisture distribution can only be solved by numerical methods, it is possible to gain

some analytical insight by studying the evolution of mean soil moisture ($\langle s \rangle$), which is

the expectation of random variable soil moisture ($s$) at any give time ($t$).

The rate of change of mean soil moisture ($d\langle s \rangle_t / dt$), representing the expected soil moisture evolution direction, can be obtained by multiplying equation (6) and $s$ and integrating over the whole range of $s$ (Laio et al. 2002),

$$\frac{d\langle s \rangle_t}{dt} = \int_0^1 \frac{\lambda(u,t)}{\gamma} p(u,t) du - \int_0^1 p(u,t) \rho(u) du - \int_0^1 \frac{\lambda(u,t)}{\gamma} p(u,t) \exp[-\gamma(1-u)] du \qquad (7)$$

The general form of equation (7) still cannot be solved analytically, but can assist in studying the slope of mean trajectory in the following special case which should receive particular attention.

To study the transient behavior of the stochastic water balance system, it is interesting to throw an imaginary particle (representing soil moisture) at any time into any location of the system and observe its immediate trajectory. A comprehensive map (in spatial and temporal dimensions) of this trajectory will help identify the possible locations towards which the particle is most likely to move, and thus the possible modes of the particle's location.

Assuming this particle is thrown at $t=t_0$ to the location $s=s_0$,

$$p(s, t = t_0) = \delta(s - s_0) \qquad (8)$$

By taking equation (8) into (7), the initial rate of change of the mean trajectory of this particle is found to be,

$$\frac{d\langle s \rangle_t}{dt}\bigg|_{s=s_0, t=t_0} = \frac{\lambda(s_0, t_0)}{\gamma} - \rho(s_0, t_0) - \frac{\lambda(s_0, t_0)}{\gamma} \exp[-\gamma(1 - s_0)] \qquad (9)$$

These three terms on the right hand side of equation (9) can be interpreted as the expectation of rainfall, the deterministic term of evapotranspiration and deep infiltration, and expectation of runoff, respectively. The sum of the three forces is the slope of mean trajectory, representing the primary moving direction of the particle at time $t=t_0$ and location $s=s_0$. Positive or negative slope indicates the particle is more likely to move upward (soil moisture increases) or downward (soil moisture decreases), respectively. A flat slope of zero value represents an equilibrium point, at which the particle has equal potential to move in two directions. An equilibrium, towards which its neighbor particles are most likely to move, would have a local maximum probability and is therefore referred to as a stable equilibrium. Conversely, an equilibrium, away from which its neighbor particles are most likely to move, would have a local minimum probability and is referred to as an unstable equilibrium. A system with two stable equilibriums and one unstable equilibrium may exhibit a bimodal state, while a system with only one stable equilibrium may have a unimodal state. The characteristics of equilibriums, identified from the slope of mean trajectory, play an important role in the development of the noise-induced preferential states.

The driving forces, in terms of slope of the mean trajectory as in equation (9), is calculated and presented in Figure 6. The cliff in the green surface is accounted for by the large amount of runoff when soil moisture is extreme wet. The pit in the middle of the green surface is formed by the stronger soil moisture-rainfall feedback in the warm

seasons, which compensate parts of the water loss. This cliff-pit surface, representing the

driving forces, crosses the horizontal plane with one intersection line and one

intersection circle. The intersection line is constituted of stable equilibrium points, and

the intersection circle is composed of half unstable and half stable equilibrium points.

These characteristics of equilibrium points will help identify the potential modality of

soil moisture distribution at any given time. For example, intersection B-B in Figure 6

has one stable equilibrium point, which is corresponding to the unimodal shape of the

intersection B-B in Figure 4. Intersection A-A in Figure 6 has two stable and one unstable

equilibriums, consistent with the bimodal shape of intersection A-A in Figure 4.
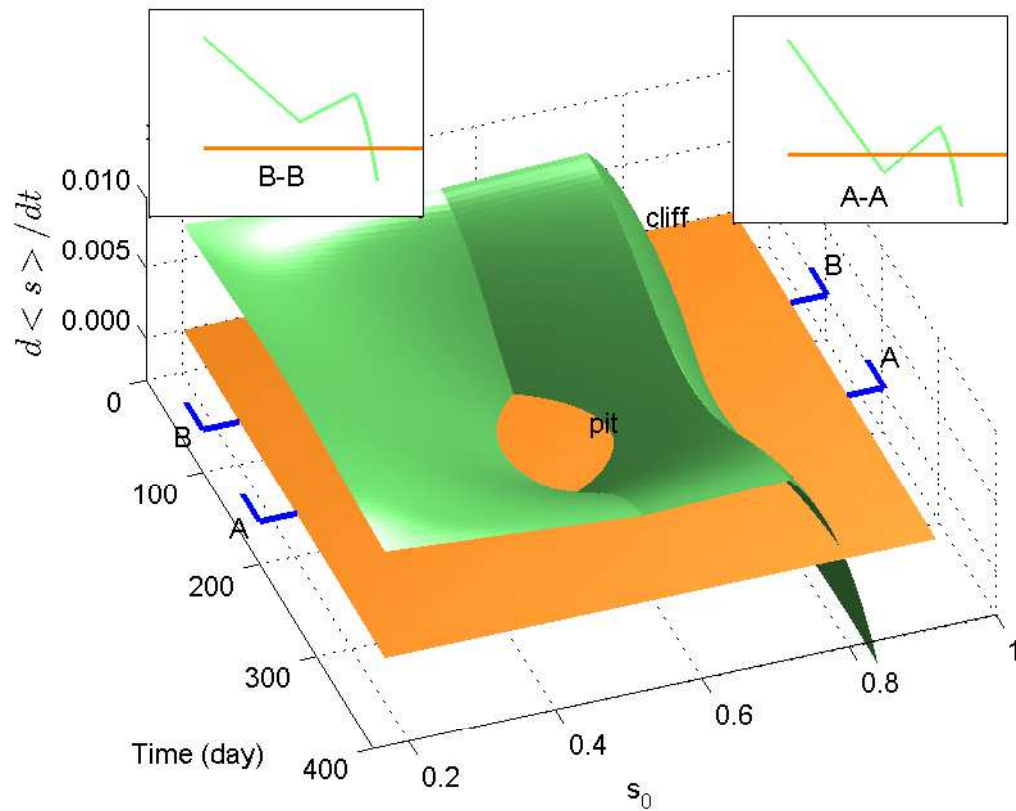
**Figure 6. Intersection of slope of mean trajectory and horizontal plane at 0. The inset A-A is the intersection at day 200, which has two stable and one unstable equilibriums. The inset B-B is the intersection at day 100 with one stable equilibrium point.**

## *2.7. Dynamical system analogy: periodically forced pitchfork bifurcation*

The average behavior of specific trajectories at a point described analytically in

the previous section suggests that the macroscopic dynamics of the soil moisture

stochastic processes with soil moisture-rainfall feedback is similar to a periodically

forced supercritical pitchfork bifurcation.

25

Supercritical pitchfork bifurcations with two different parameters are shown in Figure 7. The one on the left has two stable equilibriums A and B, towards which $s$ with negative value and with positive value will move, respectively. The shape of this symmetric pitchfork bifurcation resembles to the asymmetric slope of mean trajectory in the inset A-A of Figure 6, where there are also two stable equilibriums corresponding to the bimodal distribution in the inset A-A of Figure 4. Figure 7 (right), showing a similar shape as the inset B-B of Figure 6, has one stable equilibrium point O which attracts all points other than itself, corresponding to the unimodal distribution in the inset B-B of Figure 4. In a course of a year, the periodical forces of PET and feedback strength drive the slope of mean trajectory to change its number of equilibriums from one in spring to two in summer and back to one in late fall and winter. This switch is similar to the supercritical pitchfork bifurcation with parameters periodically changed between the two scenarios as in Figure 7.
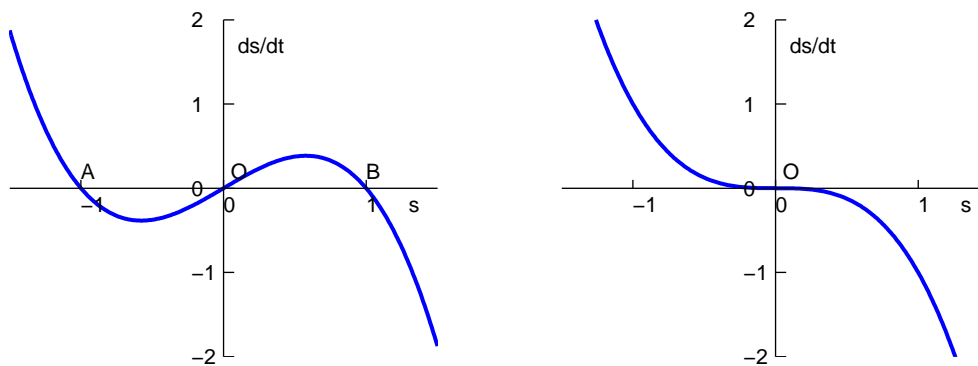


**Figure 7. Phase portrait of supercritical pitchfork bifurcation ds/dt=rs-s³. (Left) r=1. There are two stable equilibriums (A, B) at s=1 and -1; and one unstable equilibrium at s=0. (Right) r=0. There is only one stable equilibrium (O) at s=0.**

In our stochastic feedback model, extra noises act on the periodical forced nonlinear asymmetric supercritical pitchfork bifurcation system. Other than deterministically move toward one of the attractor points, the system responses to the disturbance from the noises and even occasionally jumps from one stable equilibrium zone to another, eliciting unimodal and bimodal pdf during the periodical transition of the hydro-climatic forces.

## 2.8. Bimodality from Observation

The soil moisture-rainfall feedback has the potential to give rise to bimodal soil moisture distributions during the late spring/early summer months. Using the soil moisture data observed in Peoria, here we perform a nonparametric test from Silverman (1981) to check this possibility.

The statistics test the window width of the kernel density estimates which is the sum of kernel functions (e.g. normal distribution) placed at the observations. The window width of the kernel function, controlling smooth effects of the data, needs to be large enough to obtain a unimodal estimate from a multimodal sample, or needs to be small enough to obtain a multimodal estimate from a unimodal sample. A critical widow width is found if the estimated density is in the transition between unimodal and bimodal shapes. The test compares the critical window widths from both the sample and

the smoothed bootstrap simulations to accept or reject the null hypothesis of unimodality (Silverman 1981). The critical window widths of the soil moisture samples in each summer month from observations are smaller than that from 1000 smoothed bootstrap simulations, rejecting the null hypothesis of unimodality.

The previous results also point to the fact that great care should be taken when analyzing visually for bimodality in soil moisture distributions and that statistically sound tests should be applied. To this regard, Teuling et al (2005) did not find bimodality for each month, because they used too few bins (5 bins) to derive the empirical distribution from samples. Wide bins can obviously give a unimodal estimate of empirical pdf from bimodal data, because the number of local maxima of estimated pdf is a decreasing function of bin width similar to the window width of the kernel function (Silverman 1981).

Figure 8 shows the histograms of the estimated empirical soil moisture distribution in August in Peoria, Illinois. Multimodality can be clearly recognized from 9-bin pdf but cannot from 5-bin pdf, whose wide bins smooth the bimodal shape of the distribution and make it looks unimodal. Empirical distribution of soil moisture in June and July also show bimodalities when bin number is more than 5.

Figure 8 also presents the models' pdf which is bimodal when soil moisture – rainfall feedback is considered. The match between 9-bin empirical pdf and the

modeling pdf with consideration of feedback is fairly good, especially considering that

no calibration is performed.
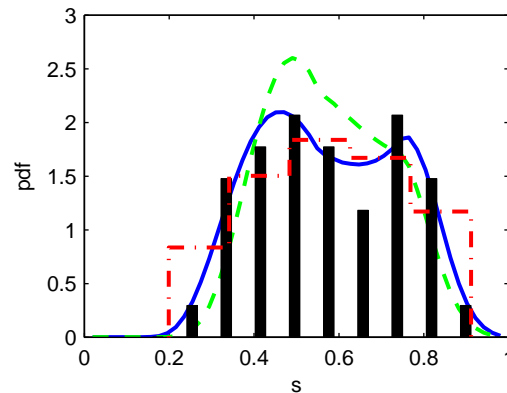


**Figure 8. Soil moisture pdf in August. Solid histograms are estimated empirical distribution from top 50cm daily soil moisture in Peoria Illinois. Dash-dotted histograms are the same empirical estimation but with only 5 bins. Solid line and dashed line are from the modeling pdf in the middle of August with and without consideration of soil moisture - rainfall feedback, respectively.**

The distribution of soil moisture samples, bimodal in each month during

summer, cannot be explained merely by external climatic force of rainfall seasonality.

This consistent soil moisture bimodal behavior emerges only if the dependence of

rainfall frequency on soil moisture becomes significant in warm seasons, corroborating

the hypothesis that the preferential state of soil moisture is a consequence of soil

moisture-rainfall feedback.

Thus, the interplay of climate seasonality and land-atmosphere interaction is

found to be able to generate consistent bimodal distribution during warm seasons,

providing additional evidence of the existence of soil moisture-rainfall feedback.

## 2.9. Climate persistence due to soil moisture feedback

Because of the soil moisture–rainfall feedback, spring or early summer soil moisture conditions will influence the precipitation in the following summer. To explore such persistence in climate, we use the joint pdf of soil moisture between early and middle summer,

$$p(s'',t'';s',t') = p(s'',t''|s',t')p(s',t') \qquad (10)$$

where, $p(s',t')$ is stationary pdf in early summer ($t=t'$), which is already calculated and presented in Figure 4, and $p(s'',t''|s',t')$ is conditional probability in middle summer ($t=t''$) when early summer ($t=t'$) soil moisture is $s=s'$, which can be numerically solved by (6).

We compare the joint pdf from models with and without soil moisture-rainfall feedback as in Figure 9. The spindle-like contour on the left indicates stronger correlation exists during this period, and the square-shaped one on the right implies a weaker dependence. Soil with shallow root zone depth of 50 cm has an approximately 20-day transitional period between wet and dry modes and is supposed to have short memory without consideration of soil moisture feedback (Teuling, Uijlenhoet, and Troch 2005). However, this feedback can enhance and sustain the effects of initial soil moisture during the period of warm seasons. Figure 9 also shows that two local maxima in the contour map can be recognized when the feedback exists, and only one local maximum

30

can be identified when the feedback does not. The two peak areas on the left, indicating

greater likelihoods, are corresponding to the transition from wet to wet mode and from

dry to dry mode. This transition illustrates how the soil moisture distribution is evolved

from a weak bimodality (at day 160) to a strong one (at day 200) under the feedback

system. The triangle peak area on the right comes from the system without feedback,

simply showing the seasonal transition from wet to dry mode.
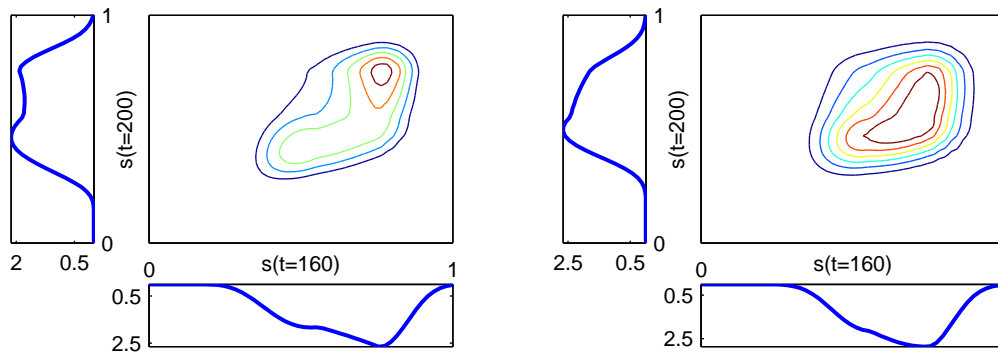


**Figure 9. Joint PDF of soil moisture between day 160 and day 200 with (left) and without (right) consideration of feedback**

## *2.10. Conclusions*

In this study, we build a stochastic water balance model with consideration of

climate seasonality and soil moisture-rainfall feedback to explain the seasonal transition

of soil moisture distribution and climate persistence in Illinois. The modeled average

rainfall frequency peaks in late spring when both the soil condition and the feedback

strength are suitable enough to trigger convective rainfall most frequently. This rainfall

frequency, consistent with the observed rainfall pattern in Illinois, is controlled by both

external climate forces and internal land-atmosphere interaction. The soil moisture

distribution is unimodal in winter and spring, becomes bimodal in summer due to the

increased feedback strength, and returns back to unimodal in the following fall. The

distribution is bimodal not only for the overall warm seasons but also for any time

during summer, consistent with the observation in Illinois. This continuous bimodality

in warm seasons, one of important evidence of land-atmosphere interaction, cannot be

simply explained only by external forces of rainfall seasonality. The joint pdf of soil

moisture indicates it is highly possible that wet soil keeps wet and dry soil keeps dry

during the warm seasons. The preferential states of soil moisture and persistent climate

pattern, in agreement with observation, support the hypothesis that soil moisture-

rainfall feedback exists.

# 3. Approximate Analytical Solution to Diurnal Atmospheric Boundary-Layer Growth under Well-Watered Conditions

This chapter is based on the article: J.R. Rigby, Yin, J., Albertson, J., Porporato, A. (2015). Approximate Analytical Solution to Diurnal Atmospheric Boundary-Layer Growth Under Well-Watered Conditions. Boundary-Layer Meteorology.

## *3.1 Introduction*

Mixed-layer models of the atmospheric boundary layer, developed by Betts (1973), Tennekes (1973) and many others, have long been used to analyze the land-atmosphere interaction. Despite their zero-dimensional simplification, mixed-layer models agree favorably with observations and results from large-eddy simulation. When coupled to land surface models such as soil-root-plant-atmosphere continuum (Daly et al. 2004), mixed-layer models provide an benchmark for a wide range of applications, from atmospheric pollutant transport to the understanding of eco-hydrological dynamics to parametrization schemes for large-scale climate models.

However, when coupled to the surface heat flux partitioning, even the simplest mixed-layer model does not permit analytical solutions, complicating any potential analysis and physical interpretation of the land-atmosphere interaction. To progress in this direction, we discuss approximate analytical solutions for the mixed-layer model. As a first attempt, we confine our study to well-watered condition, under which the

stomatal conductance and aerodynamic conductance are assumed to be constant during

the day.

## *3.2 Basic Equations of the Diurnal Convective ABL*

At the surface, energy flux partitioning is controlled by surface energy balance,

$$Q = H + \lambda E , \tag{11}$$

Where $Q$ is net available energy, $H$ is the sensible heat flux, $\lambda$ is the specific latent heat

of vaporization, and $E$ is the evaporative flux. The latter two energy flux can be

expressed as,

$$H = g_h c_p \rho (\theta_s - \theta) , \tag{12}$$

and,

$$E = g_e \rho (q_s^* - q) , \tag{13}$$

where $\rho$ is air density, $c_p$ is heat capacity at constant pressure, $q^*$ is saturation specific

humidity, $q$ and $\theta$ are specific humidity and potential temperature in the mixed layer.

The subscript s refers to the values at the surface. The conductances $g_h$ and $g_e$ typically

consist of series of canopy and atmosphere conductance,

$$g_h = 1/r_a , \tag{14}$$

and

$$g_e = 1/(r_a + r_s) , \tag{15}$$

where $r_a$ is aerodynamic resistance and $r_s$ is surface resistance.

The conservation of dry static energy in the mixed layer gives,

$$\rho c_p h \frac{d\theta}{dt} = H + \rho c_p [\theta_f(h) - \theta] \frac{dh}{dt} , \qquad (16)$$

and similarly, the conservation of the mass of water vapor in the mixed layer yields,

$$\rho h \frac{dq}{dt} = E + \rho [q_f(h) - q] \frac{dh}{dt} , \qquad (17)$$

where the subscript $f$ refers to the values of the free atmospheric profiles. To close the

above equations, the heat flux at the top of the boundary is assumed to be proportional

to the surface heat flux,

$$-(\overline{w'\theta'})_h = \beta(\overline{w'\theta'})_s , \qquad (18)$$

where the ratio $\beta$ ranges from 0.1 to unity with a typical value of 0.2 (Ball 1960; Stull

1976).

With assumptions of linear free atmospheric profiles (Tennekes 1973; Porporato

2009), the growth of the simplified boundary layer can be expressed as,

$$\frac{dh}{dt} = \frac{(1+2\beta)H(t)}{\rho c_p \gamma_\theta h} . \qquad (19)$$

Once the surface and free atmospheric conditions and the radiative forcing are specified,

equations (11)-(19) in conjunction with the Clausius-Clapeyron relation represent a

closed system of coupled, non-linear differential-algebraic equations for the idealized

diurnal mixed layer.

## 3.3 Penman-Monteith Approach and Equilibrium Bowen Ratio

To understand the coupling between surface heat partition and boundary-layer growth, it is important to analyze each component of fluxes as typically done in the Penman-Monteith or combination approach (Raupach 2001; Brutsaert 2005). Equation (13) can be written as,

$$E = E_{eq} + E_{vpd} = g_e \rho (q_s^* - q^*) + g_e \rho (q - q) , \qquad (20)$$

where $E_{eq}$ is equilibrium evaporation, and $E_{vpd}$ is evaporative flux due to vapor pressure deficit. With first-order approximation of saturation specific humidity relation, the equilibrium evaporation can be further expressed as,

$$E_{eq} = g_e \rho \varepsilon_r (\theta_s - \theta) . \qquad (21)$$

Consequently, the equilibrium Bowen ratio can be found as the ratio of sensible heat flux to the equilibrium evaporation (Priestley and Taylor 1972; McNaughton 1976; De Bruin 1983; Garratt 1992; Betts 1994),

$$Bo_{eq} = \frac{H}{\lambda E_{eq}} = \frac{g_h c_p \rho (\theta_s - \theta)}{\lambda g_e \rho (q_s^* - q^*)} = \frac{g_h c_p}{\lambda g_e \varepsilon_r} , \qquad (22)$$

This equilibrium Bowen ratio is also the upper limit of the Bowen ratio as $Q \to \infty$. Generally, when keeping all other variables fixed, the Bowen ratio increases with the increasing available energy and quickly reaches an upper limit ($Bo_{eq} = Bo_{max}$) (Porporato 2009).

To solve the mixed-layer model, we also need explicit expression for surface temperature as required in (12) and (13). To proceed in this way, equation (11) can be written as,

$$Q = \lambda g_e \rho (\tilde{q}_s^* - \tilde{q}) + \lambda g_e \rho (\tilde{q}_{\theta_{f0}}^* - q_{f0}) + g_h c_p \rho (\tilde{\theta}_s - \tilde{\theta}) , \tag{23}$$

where the notation tilde refers the variables are relative to surface values, i.e.

$$\tilde{q}_s^* = q^*(\theta_s) - q^*(\theta_{f0}) , \tag{24}$$

and,

$$\tilde{\theta}_s^* = \theta_s - \theta_{f0} . \tag{25}$$

Substitution the equilibrium Bowen ratio (22) into (23) gives the surface potential temperature,

$$\tilde{\theta}_s = \frac{Bo_{eq}}{1 + Bo_{eq}} \left( \frac{Q}{\rho g_h c_p} + \frac{\lambda g_e}{c_p g_h} \tilde{q} + \tilde{\theta} - \frac{\lambda g_e \Delta_{q0}}{g_h c_p} \right) , \tag{26}$$

where $\Delta_{q0}$ is the initial saturation specific humidity deficit. Substitution (26) into the combination of (11), (12), and (19) gives the following nonlinear ordinary differential equation,

$$\frac{dh}{\underbrace{dt}_{I}} = \underbrace{\frac{f(t)}{h}}_{II} + \underbrace{\frac{g(t)}{h^2}}_{III} + \underbrace{C}_{IV} , \tag{27}$$

where

$$f(t) = \frac{1+2\beta}{\rho c_p \gamma_\theta} \frac{Bo_{eq}}{1+Bo_{eq}} \left( Q(t) - \rho \lambda g_e \Delta q_0 \right)$$

$$g(t) = g_e \frac{1+2\beta}{\rho c_p \gamma_\theta} \frac{Bo_{eq}}{1+Bo_{eq}} \int_0^t Q(u) du \qquad (28)$$

$$C = \left( -\frac{1+2\beta}{1+Bo_{eq}} \right) g_h + \left( -\frac{c_p \gamma_\theta - \lambda \gamma_q (1+2\beta)}{2 c_p \gamma_\theta} \frac{Bo_{eq}}{1+Bo_{eq}} \right) g_e$$

The system is now reduced to an ordinary differential equations for boundary-layer

depth. This equation still resist analytical solution due to its strong nonlinearity. In the

following sections, we will try to find its approximate solution in more detail.

## *3.4 Approximate Analytical Solution*

Looking closer at the system, Figure 10 (left) shows each term in equation (27)

solved numerically. As can be seen, term I and II are almost parallel to each other with a

distance related to the sum of terms III and IV, which is small comparing with other

terms. By treating the sum of III and IV as a small perturbation, the zero-order

perturbation solution $h_0(t)$ of (27) is,

$$h_0(t) = \sqrt{2 \int_0^t f(u) du} , \qquad (29)$$

which is the solution by assuming the Bowen ratio is constant and equal to the

equilibrium Bowen ratio. For this reason, this zero-oder solution is also named

equilibrium solution ($h_{eq}$). This solution accounts for a particular heat flux partitioning,

where only equilibrium evaporation turns into latent heat flux. The first-order

perturbation solution for (27) is,

$$h_1(t) = C't, \tag{30}$$

which is the adjustment of the boundary layer height due to the vapor pressure deficit, which is neglected in the equilibrium solution. To estimate the constant C′ in (30), we need an estimation of term III in (27). Recalling that $g(t) = g_e \int f(u)du$, term III can be written as,

$$\frac{g(t)}{h^2} = \frac{g_e}{2}\left(\frac{h_{eq}(t)}{h}\right)^2, \tag{31}$$

In this form, as $h_{eq}/h$ approach 1, the term in brackets approaches $g_e/2$ and C′ is then approaches $g_e/2+C$. Since C is generally negative in value, and heq is larger than $h$, we can approximate C′ as,

$$C' = \frac{1}{2}\left(C + \frac{g_e}{2}\right). \tag{32}$$

In this way, the Penman-Monteith approach for the separation of evaporation is finally adopted in the boundary-layer system and facilitates the derivation of approximate analytical solutions. Figure 10 (right) shows the accuracy of using this approximate analytical solution. As can be seen, the equilibrium solution overestimate the boundary-layer growth due the over-partitioning sensible heat flux. The adjustment due the vapor pressure deficit can efficiently correct most of the bias in the equilibrium solutions.

With the analytical solutions for the boundary layer height, all other states in the ABL, such as potential temperature and specific humidity, can be derived correspondingly as have been done in Porporato (2009).

39
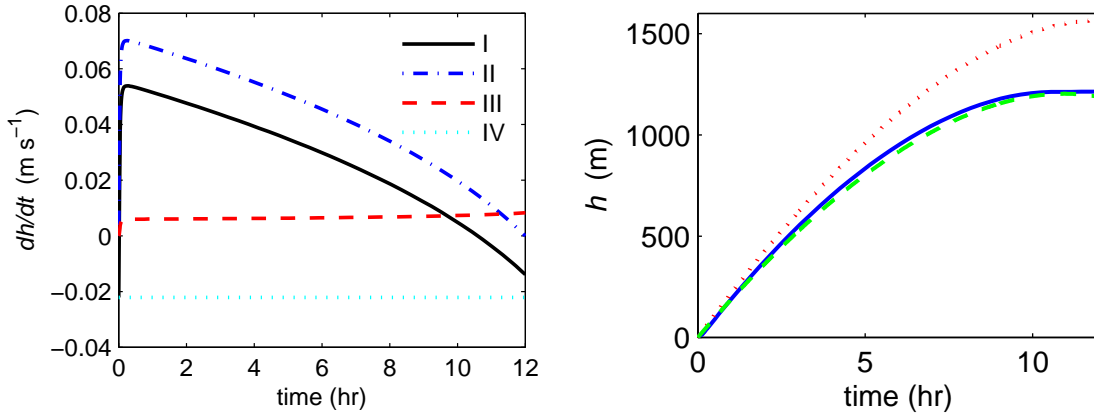
**Figure 10. (Left) Numerical simulation of the mixed-layer height growth rate of each term in equation (27). The parameters in these numerical simulations represent typical surface and atmospheric characteristics in warm seasons under well-watered condition. (Right) The mixed-layer height evolution predicted by the full numerical simulation (blue solid line), equilibrium solution (red dot line), and approximate analytical solution (green dash line).**

## *3.5 Model Testing*

To test the models and approximation methods, we use sounding profiles and surface heat flux data from the Atmospheric Radiation Measurement (ARM) Program (http://www.arm.gov/) at Central Facility in Southern Great Plains (CF-SGP). Radiosonde data in CF-SGP are often available in early morning (0530 local time) and late afternoon (1730 local time). Radiosonde measurements of temperature, pressure, and relative humidity were converted to profiles of potential temperature and specific humidity. Half-hour accumulated precipitation is measured by the Surface Meteorological Observation System (SMOS). Half-hour averaged soil moisture, surface

40

latent heat flux, and sensible heat flux are measured with an Energy Balance Bowen

Ratio Station (EBBR).

In CF-SGP, the vegetation is mainly grass and pasture. Under well-watered

condition, surface resistance $r_s$ is set to a typical value of 70 s m$^{-1}$, and aerodynamic

resistance $r_a$ (s m$^{-1}$) for the grass surface is approximated as $r_a=208/u_2$, where $u_2$ is the

wind speed at 2 m (Allen et al. 1998). Net available energy is modeled as $Q = Q_{max}[1-(t/t_0-$

$1)]$, where $t_0 = 6$ hr is the time of the midday.

Clear-sky days under well-watered conditions from 2002 to 2009 in summer

were chosen to test the model. The calibrated parameters for these ensemble mean

profiles, representing the typical atmospheric characteristics under well-watered

condition in continental temperate region in summer, were used to test the various

models and approximation methods. All these typical parameters are listed in Table 1.

**Table 1 Typical parameters for model testing derived from observations in CF-SGP**

| Variables | Value | Unit |
|:---:|:---:|:---:|
| $\gamma_\theta$ | 0.0065 | K m$^{-1}$ |
| $\theta_{f0}$ | 293 | K |
| $\gamma_q$ | $-3.3\times10^{-6}$ | kg kg$^{-1}$ m$^{-1}$ |
| $q_{f0}$ | 0.014 | kg kg$^{-1}$ |
| $Q_{max}$ | 493 | W m$^{-2}$ |
| $\beta$ | 0.2 | - |
| $u_2$ | 5.44 | m s$^{-1}$ |

To further test the approximation method, here we plot its solutions of ABL height at the end of the day against the full numerical simulations using the atmospheric parameters from the observations as in Figure 11. As can be seen, the approximation method can capture the essential ABL evolution under various climate conditions.
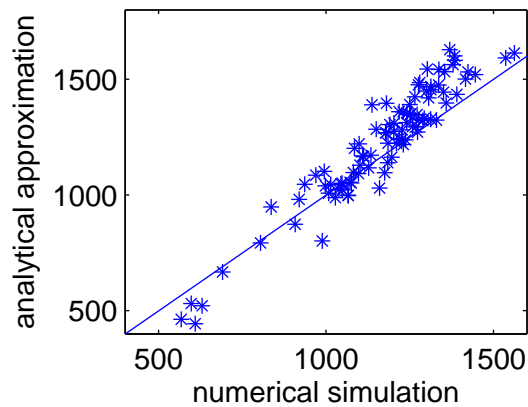


**Figure 11. ABL height at the end of the day (t = 12 *h*) predicted by analytical approximation (y-axis) and full numerical simulation (x-axis).**

To demonstrate the detail of diurnal evolution of the ABL, we compare the daytime Bowen ratios from observation with the ones from full numerical simulation and analytical approximation in two typical days in CF-SGP in Figure 12. The numerical simulation and the approximation follow the diurnal variation of the observed Bowen ratios, indicating the approximation can efficiently partition the sensible and the latent heat flux for the given available energy.
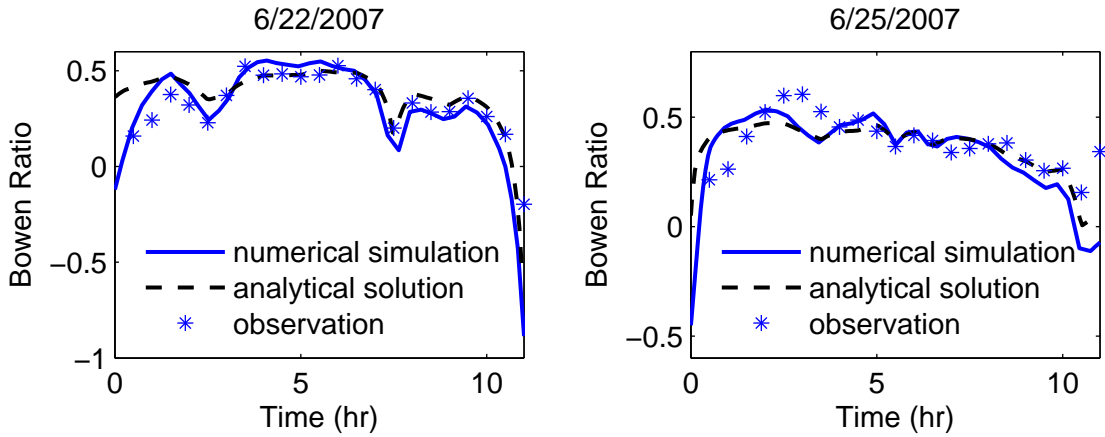
**Figure 12. Diurnal evolution of Bowen ratio from numerical simulations, analytical approximations, and observations on 22 June and 25 June 2007.**

## *3.6 Conclusions*

We have presented a theoretical investigation of a mixed-layer model for the diurnal convective boundary layer dominated by buoyancy-drive turbulence for which the potential temperature and specific humidity can be solved in terms of the boundary-layer height and time. We have further derived the differential equation for the growth of the boundary layer, in terms of $h(t)$ and $t$ only and shown using perturbation methods that the solution of Porporato (2009) assuming constant Bowen ratio represents the zero-order approximate solution to this differential equation. A closed form solution for the first-order approximation is derived here from which the entire system can be solved algebraically to first order for given net radiation function $Q(t)$. The structure of the solution results from the two components of evaporation (i.e. equilibrium evaporation

and evaporation due to vapour pressure deficit), allowing us to propagate into the ABL

growth the different effects of energy and moisture balances.

# 4. Land and atmospheric controls on initiation and intensity of moist convection: CAPE dynamics and LCL crossings

This chapter is based on the manuscript: J. Yin, J. Albertson, JR Rigby, and A.

Porporato (2015). Land and atmospheric controls on initiation and intensity of moist

convection: CAPE dynamics and LCL crossings. Water Resources Research (under

review)

## *4.1 Introduction*

Land-atmosphere coupling involves interacting processes among surface and

subsurface hydrology, vegetation, and atmospheric dynamics at different spatial and

temporal scales (Ek and Mahrt 1994; Brubaker and Entekhabi 1995; D'Odorico and

Porporato 2004; Scanlon and Albertson 2004). In particular, the soil water and surface

energy states affect the dynamics of the atmosphere through the surface latent-sensible

heat flux partitioning, while the atmospheric conditions influence the surface

evapotranspiration via environmental factors, such as radiative forcing, temperature,

wind speed, vapor pressure deficit and $CO_2$ concentration. These factors form

interesting feedback loops that control the relationships between surface hydrology and

atmospheric moist convection, and in turn play an important role on climatic and

ecohydrological processes (Betts et al. 1996; Findell and Eltahir 2003b; Koster et al. 2003;

Juang et al. 2007a; Betts 2009; Siqueira et al. 2009; Konings et al. 2010; Yin et al. 2014).

Several previous studies have analyzed the land-surface and free atmospheric controls on the initiation of moist convection and cloud formation focusing on the conditions leading the atmospheric boundary layer (ABL) to cross the lifting condensation level (LCL) (Ek and Mahrt 1994; Ek and Holtslag 2004; Juang et al. 2007a; Juang et al. 2007b; Konings et al. 2010; Gentine et al. 2013). In particular, simple mixed-layer models of the ABL have been effective in capturing these processes and elucidating the connection between the surface states and the ABL growth toward the LCL. For example, Siqueira et al. (2009) explored the linkage between soil moisture and initiation of moist convection by coupling a soil-plant hydrodynamics model to a simplified ABL model and found that when the soil is dry an external source of water (i.e. advection) is required to trigger moist convection. Gentine et al. (2013) found dry soil advantage and wet soil advantage regimes by investigating the relative humidity at the top of the boundary layer through a conceptual mixed-layer model.

It is important to note that the LCL crossing is a necessary but not sufficient condition for the initiation of deep convection. This is demonstrated, e.g., in the modeling study of Juang et al. (2007a) in which convective precipitation was always preceded by LCL crossing, while an LCL crossing only resulted in convective precipitation in 45% of cases. The reason for this is that the probability of occurrence and intensity of moist convection is controlled by the accumulation of convective available potential energy (CAPE) up to the time of LCL crossing (Emanuel 1994; Kirkpatrick et al.

46

2011). In particular, it has been shown that to trigger convective rainfall in the mid-latitude continental regions, CAPE typically must exceed 400 J kg$^{-1}$ (Battan 1973; Findell and Eltahir 2003b). Furthermore, the Storm Prediction Center (SPC) classifies atmospheric instability based on CAPE, as weak (CAPE < 1000 J kg$^{-1}$), moderate (CAPE ~ 1000-2500 J kg$^{-1}$), strong (CAPE ~ 2500-4000 J kg$^{-1}$), and extreme instability (CAPE > 4000 J kg$^{-1}$). Consequentially, CAPE can be used to efficiently interpret the atmospheric instability and diagnose severe thunderstorm environments (Dean et al. 2009).

It is reasonable to conclude that both the time of LCL crossing and the corresponding value of CAPE should be considered as indicators of subsequent moist convection. This changes the model condition from a simple binary crossing/no-crossing of the LCL to the combination of LCL crossing/no-crossing and a CAPE condition of greater/less than certain thresholds (e.g. 400 J kg$^{-1}$). That simple change creates four possible regimes rather than two. If those regimes were equiprobable one might expect LCL crossing to be followed by convective precipitation in about half of cases, which is similar to the results of Juang et al. (2007b). Interestingly, as we will demonstrate, the temporal evolution of CAPE, LCL, and the height of the ABL depend strongly on the combination of soil and atmospheric conditions, unveiling more complex pathways leading to deep convection, which clearly go beyond simple criteria based on the onset of condensation. For example, both wet and dry soils can trigger early moist convection, as demonstrated in Gentine et al. (2013), while wet soil almost always tends to have a

47

large magnitude of CAPE. As a result, early moist convection triggered by dry soils may be too weak to develop into deep convection. Therefore, we contend that special attention should be paid to the joint dynamics of the LCL and CAPE and their sensitivity to soil conditions for the understanding of the impacts of land-atmosphere coupling on convective precipitation.

In this study we embed a simple soil-plant model within a zero-dimensional mixed-layer model for the convective ABL (Garratt 1992; Porporato 2009) to simulate the diurnal development of the ABL up to the crossing of the LCL as needed to explore the patterns of LCL crossing time and CAPE evolution. This coupled model captures the essential feedbacks between the land surface and atmosphere within the growing ABL, including the partitioning of surface energy into sensible and latent heat fluxes, the effects of soil and plant water stress in controlling evapotranspiration, as well as the moisture and energy fluxes entrained from the free atmosphere, and allows for a simultaneous computation of the LCL and CAPE evolution as a function of surface (i.e. soil moisture) and free atmosphere conditions. We only focus on the boundary-layer dynamics before the LCL crossing by using the mixed-layer model, but preserve the investigation of the complicated cloud feedback in the cloud-topped boundary layer for future study. The chapter is organized as follows: section 2 introduces the ABL model, the soil-plant model, and the convection indicators. Section 3 presents the patterns of LCL crossing times and CAPE dynamics using a parameterization based on atmospheric

conditions in the Central Facility, Southern Great Plains. Final conclusions are

summarized in section 4. An appendix discusses the pseudo-adiabatic processes and the

analytical determination of the LCL evolution.


## 4.2 Model description

The essential dynamics of the ABL in the absence of clouds are described using a

simple zero-dimensional mixed-layer model, driven by the surface latent and sensible

heat flux and by entrainment of energy and moisture from the free atmosphere. The

surface heat flux partitioning is controlled by a soil-plant model which includes the

effects of soil moisture stress on vegetation. This coupled soil-plant-ABL model provides

the diurnal evolution of the temperature and the humidity in the mixed layer, from

which the LCL crossing time and CAPE evolution are computed.

*a. ABL model*

The simplified zero-dimensional mixed-layer models used in this study were

pioneered by Ball (1960), Lilly (1968), Betts (1973), Carson (1973), and Tennekes (1973) in

a series of classic studies of simplified models of the ABL. They assume that (1) the

boundary layer is well-mixed and thus the virtual potential temperature and specific

humidity are constant throughout the ABL, (2) the land surface and the atmosphere are

horizontally homogeneous without advection, and (3) the inversion above the ABL is

approximated by an instant jump for both temperature and humidity variables (Stull

1988; Garratt 1992; Porporato 2009) (see thick solid lines in Figure 10).

The governing equation for the virtual potential temperature in the boundary

layer is given as (Stull 1988)

$$\rho_a c_p h \frac{d\theta_{vBL}}{dt} = H_v + \rho_a c_p [\theta_{vf}(h) - \theta_{vBL}] \frac{dh}{dt}, \tag{33}$$

where $\rho_a$ is air density, $c_p$ is the specific heat of air, $h$ is the height of ABL, $H_v$ is the

virtual sensible heat flux (Garratt 1992; Brutsaert 1998), $\theta_{vBL}$ and $\theta_{vf}$ are the virtual

potential temperature within the boundary layer and in the free atmosphere,

respectively. The virtual potential temperature is slightly different from the potential

temperature due to the lighter density of water vapor than that of the dry air (Emanuel

1994),

$$\theta_v = \theta[1 + (R_v / R_d - 1)q - q_l], \tag{34}$$

where $R_v$ and $R_d$ are the gas constant for water vapor and dry air, respectively, and $q_l$ is

liquid water content, which is zero in this cloud-free ABL.

Similarly, the conservation of water vapor in the mixed layer gives

$$\rho_a h \frac{dq_{BL}}{dt} = E + \rho[q_f(h) - q_{BL}] \frac{dh}{dt}, \tag{35}$$

where $q_{BL}$ and $q_f$ are the specific humidity within the boundary layer and in the free

atmosphere, respectively, and $E$ is evapotranspiration. In the free atmosphere, the

temperature and humidity profiles may be assumed to be linear functions of height ($z$)

50

with slopes ($\gamma_{\theta_v}$, $\gamma_q$) and surface values ($\theta_{vf\,0}$, $q_{f0}$). When neglecting the morning

transition, the growth of the ABL can be modeled as (Tennekes 1973; Garratt 1992)

$$\frac{dh}{dt} = \frac{(1+2\beta)H_v}{\rho c_p \gamma_{\theta_v} h},$$
(36)

using a common closure assumption in which the ratio of entrainment sensible heat flux

to the surface sensible heat flux is assumed to be a constant, $\beta$, with typical value of 0.2

(Tennekes 1973; Stull 1976). The previous equations allow one to model the evolution of

the ABL once the surface fluxes are specified, as described next.

b. Soil-plant model

The surface sensible ($H$) and latent ($\lambda E$) heat fluxes are partitioned from the

available energy ($Q$) (Brutsaert 2005),

$$Q = H + \lambda E,$$
(37)

where $\lambda$ is the latent heat of water vaporization. The sensible heat flux ($H$) can be

further expressed as (Burke 1945),

$$H = g_a c_p \rho_a [\theta_s - \theta_{BL}],$$
(38)

where $c_p$ is specific heat of air, $\theta_s$ and $\theta_{BL}$ are the potential temperature at the surface

and in the boundary layer, and $g_a$ is the series conductance of leaf boundary layer and

atmospheric boundary layer. Likewise evapotranspiration is modeled as

$$E = \frac{g_a g_s}{g_a + g_s} \rho_a [q_s - q_{BL}],\tag{39}$$

where $q_s$ is the specific humidity at the evaporating surface, and $g_s$ is stomatal

conductance, which depends on both plant physiology and environmental conditions

(Ball et al. 1987). This is the link where the soil moisture conditions exert their role in the

land-atmosphere interaction. Specifically, the empirical approach of the Jarvis'

formulation is used here to model the stomatal conductance (Jarvis 1976; Daly et al.

2004)

$$g_s = g_{s\,max} f_Q(Q) f_{\theta_{BL}}(\theta_{BL}) f_{\psi_l}(\psi_l) f_{\delta q}(\delta q),\tag{40}$$

where $\delta q$ is saturation deficit of specific humidity, defined as

$$\delta q = q_{sat}(\theta_{BL}) - q_{BL},\tag{41}$$

where $q_{sat}$ is the saturation specific humidity, which is determined by the temperature in

the lower level of the boundary layer ($\theta_{BL}$), $g_{s\,max}$ is the maximum stomatal conductance,

$\psi_l$ is the leaf water potential, and $f_Q$, $f_{\theta_{BL}}$, $f_{\psi_l}$, and $f_{\delta q}$ are functions of corresponding

variables $Q$, $\theta_{BL}$, $\psi_l$, and $\delta q$, respectively. The water potential gradient from the soil to

the leaves drives the water flux into and through the plant,

$$E = g_{srp}(\psi_s - \psi_l),\tag{42}$$

where $\psi_s$ is the soil water potential, which is given by a Brooks-Corey type retention

curve (Rodríguez-Iturbe and Porporato 2005),

$$\psi_s = \overline{\psi}_s s^{-b}, \tag{43}$$

where $s$ is the soil moisture, $b$ is the exponent of the retention curve, and $\overline{\psi}_s$ is the soil water potential at saturation point (Clapp and Hornberger 1978). The soil-root-plant conductance $g_{srp}$ in (42) is the series equivalent of the soil-root conductance and plant conductance,

$$g_{srp} = \frac{L_{AI} g_p g_{sr}}{L_{AI} g_p + g_{sr}}, \tag{44}$$

where $L_{AI}$ is leaf area per unit ground area, $g_p$ is plant conductance in terms of unit leaf area, and $g_{sr}$ is soil-root conductance per unit ground area. The soil-root conductance is modeled as a simplified cylindrical root function (Katul et al. 2003; Rodríguez-Iturbe and Porporato 2005),

$$g_{sr} = \frac{K \sqrt{R_{AI} s^{-a}}}{\pi g \rho_w Z_r}, \tag{45}$$

where $g$ is gravitational acceleration, $\rho_w$ is water density, $K$ is hydraulic conductivity, $a$ is parameter that attenuates the reduction due to hydraulic conductivity under water stress conditions, and $R_{AI}$ is root area per unit ground area. The hydraulic conductivity and root area index are related to the soil moisture and are modeled as $K = K_s s^{2b+3}$ (Clapp and Hornberger 1978), where $K_s$ is the saturated hydraulic conductivity. The plant conductance drops when leaf water potential is low and this decrease is modeled as (Katul et al. 2003),

$$g_p = g_{p\,\text{max}} \exp\left[-\left(-\frac{\psi_l}{d}\right)^c\right], \tag{46}$$

where the parameters $c$ and $d$ depend on different types vegetation (see detail in Daly et al. (2004)). The essential components of land-atmosphere feedbacks can be efficiently simulated using the above coupled equations, once soil moisture conditions are specified in (43) – (46) along with boundary-layer conditions in (33) and (35) and radiation forcing in (37).

*c. Moist convection indicators*

The soil-plant-ABL model can be used to simulate the diurnal evolution of temperature and humidity within the mixed-layer. By comparing the buoyancy of an adiabatically lifted air parcel with that of the surrounding free atmosphere, suitable indicators of moist convection can thus be derived, as is customary in hydrometeorology (Stull 1988; Emanuel 1994; Tsonis 2002). For relatively small displacements, when the unsaturated air parcel is adiabatically lifted, the pressure decrease is small and no condensation takes place. As a result, the parcel follows a dry adiabatic process (see Appendix A), in which potential temperature and the specific humidity remain constant with height (dashed line in Figure 10), while the parcel temperature decreases according to the dry adiabatic lapse rate. For larger displacements, the adiabatic expansion produces stronger temperature drops, until the parcel temperature reaches the

saturation point at the LCL (see Appendix B and Figure 10). Further adiabatic lifting

above the LCL causes condensation, and the resulting temperature profile follows the

so-called moist adiabatic processes (see Appendix A and Figure 10).

Due to condensation the virtual potential temperature will continue to increase

as the parcel is lifted higher (thin solid line in Figure 10) such that eventually the virtual

potential temperature of the air parcel may exceed that of the surrounding air. At this

point, termed the level of free convection (LFC), the parcel becomes positively buoyant

with respect to the surrounding atmosphere and will continue to rise. Below the LFC,

adiabatic lifting results in negative buoyancy and inhibits the convection, while above

the LFC the situation is reversed, resulting in positive buoyancy. Further above, the

moist adiabat again crosses the surrounding temperature profile (see Figure 10) at the

level of neutral buoyancy (LNB), above which the buoyancy with respect to the free

atmosphere is again negative. The difference in virtual potential temperature between

the adiabatically lifted air parcel and the surrounding atmosphere is a measure of the

buoyant force on an air parcel. The total area of positive buoyancy between the LFC and

the LNB is thus a measure of buoyant potential energy termed the Convective Available

Potential Energy (CAPE),

$$CAPE(t) = \int_{z_{LFC}(t)}^{z_{LNB}(t)} g \frac{T_{v,p}(z,t) - T_{v,srd}(z,t)}{T_{v,srd}(z,t)} dz, \qquad (47)$$

where $T_{v,p}$ and $T_{v,srd}$ are the virtual temperature of the air parcel and the surrounding air,

respectively, and $z_{LFC}$ and $z_{LNB}$ are the height of LFC and LNB, respectively. Similarly, the

total negative buoyancy below the LFC will hold the rising air parcel and is defined as

convective inhibition (CIN),

$$CIN(t) = -\int_{z_0}^{z_{LFC}(t)} g \frac{T_{v,p}(z,t) - T_{v,srd}(z,t)}{T_{v,srd}(z,t)} dz \,,$$ (48)

where $z_0$ is the height at the earth surface.
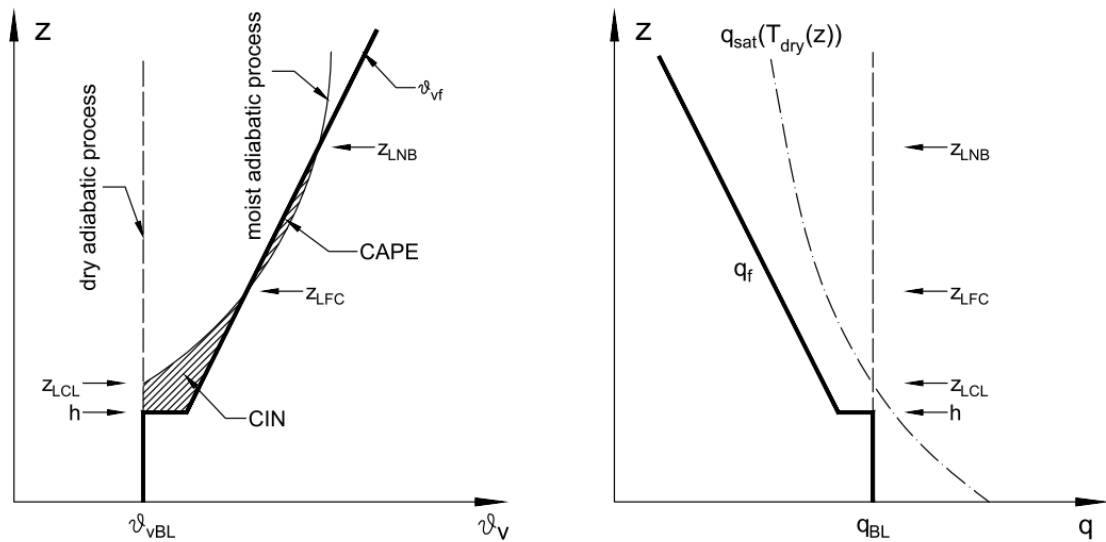


**Figure 13. Schematic representation of ABL model and moist convection indicators. Thick solid lines are vertical profiles of virtual potential temperature and specific humidity, thin dash lines are dry adiabatic process, thin solid lines are moist adiabatic process, and thin dash-dot lines are saturation specific humidity at the dry adiabatic temperature (Tdry).**

## *4.3 Results*

The ABL model of section 4.2 can be numerically solved to obtain the dynamics

of LCL and CAPE (as described in appendix and section 4.2). This model is

parameterized and analyzed with reference to a well-defined field experiment described next.

## 4.3.1 Study site

To analyze the land-atmosphere coupling and its effects on moist convection, we focus on summer conditions observed in the Central Facility, Southern Great Plains (CF-SGP), which is characterized by strong land-atmosphere interaction in the warm seasons (Koster et al. 2004).

Radiosonde data in the summer early morning (0530 local time) are used to find the slopes and surface values of the temperature and humidity profiles (Figure 14). As can be seen, the slopes and surface values are negatively correlated, indicating that unstable free atmosphere conditions tend to correspond to a warmer land surface, while wetter air in the lower atmosphere is associated to rapid decreases in upper atmosphere moisture. Similar correlations were also observed in other regions (Konings et al. 2010). Based on these observations, the surface values ($\theta_{vf0}$, $q_{f0}$) are modeled as linear functions of slopes ($\gamma_{\theta v}$, $\gamma_q$) to reduce the number of parameters describing the state of the free atmosphere.
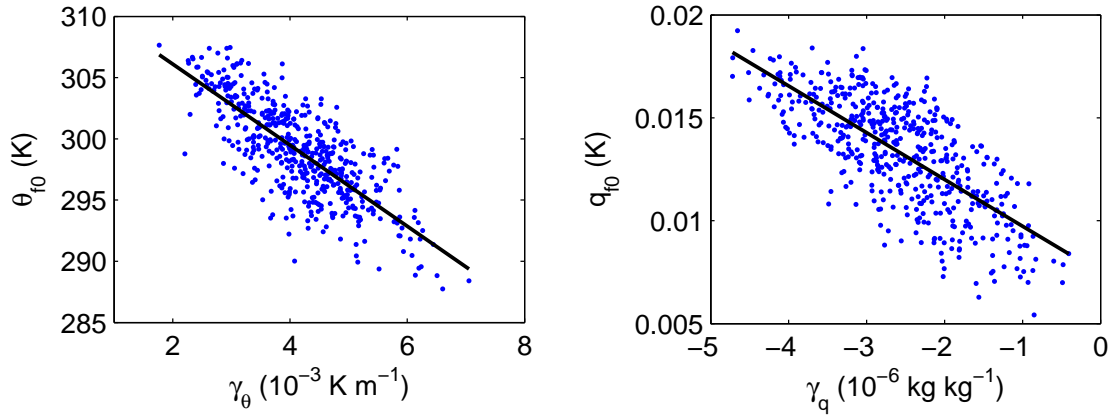
**Figure 14. Scatter plots of morning potential temperature surface value $\theta_{f0}$ versus lapse rate $\gamma_\theta$ (left), and morning humidity surface value $q_{f0}$ versus profile slope $\gamma_q$ (right).**

Surface heat fluxes in CF-SGP are measured at 30-min interval with an Energy Balance Bowen Ratio Station (EBBR). The available energy shows maximum values in the midday and minimum values in the early morning and late afternoon with a trend well approximated by a parabolic function, with peak value $Q_{max} = 490$ W m$^{-2}$ at midday ($t = 6$ hr) and zero value at $t = 0$ hr and $t = 12$ hr. The soil and vegetation parameters are the same as in Daly et al. (2004), representing the typical C3 plants and silt loam soil at CF-SGP.

### 4.3.2 Diurnal evolution

We first show the diurnal evolution of surface energy partitioning with typical free atmosphere conditions parameterized on July 18, 2009 (see Table 1), under different soil moisture conditions from well-watered to a condition near the wilting point. The

plants are assumed to begin closing stomata in response to water stress when soil

moisture is below $s* = 0.45$, and reach complete closure when soil moisture is below the

wilting point $s_w = 0.25$. As can be seen in Figure 15, the stomatal conductance generally

follows the variation of radiation under well-watered condition, while it decreases

sharply in midday in conditions of water stress. The transpiration shows a related

pattern with a flattening due to stomatal closure (Daly et al. 2004).
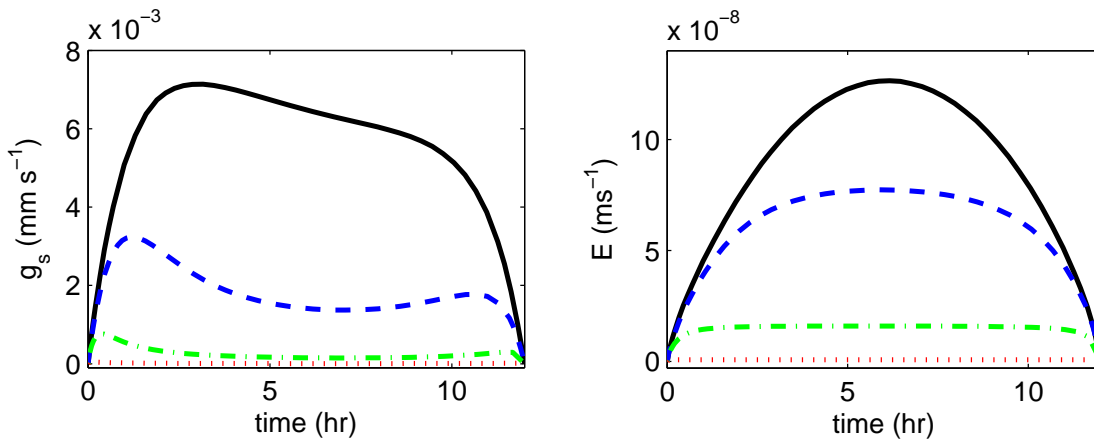


**Figure 15. Stomatal conductance and evapotranspiration for different soil moisture conditions s = 0.45 (solid line), s = 0.38 (dash line), s = 0.32 (dash-dotted line), and s = 0.25 (dotted line). The soil and vegetation parameters are the same as in Daly et al. (2004), and the atmospheric parameters are in Table 2.**

**Table 2 Atmospheric parameters in the early morning on July 18, 2009 at CF-SGP.**

| Variables | Value | Unit |
|-----------|-------|------|
| $\gamma_{\theta v}$ | 0.0033 | $K\ m^{-1}$ |
| $\theta_{vf0}$ | 298 | K |
| $\gamma_q$ | $-2.1 \times 10^{-6}$ | $kg\ kg^{-1}\ m^{-1}$ |
| $q_{f0}$ | 0.011 | $kg\ kg^{-1}$ |
| $Q_{max}$ | 490 | $W\ m^{-2}$ |

The soil moisture control on evapotranspiration via stomatal conductance affects the energy partitioning and thus the boundary-layer dynamics. Figure 16 shows the diurnal evolution of ABL, LCL, LNB, and LFC under various soil conditions. During the day, both ABL and LCL increase but end up crossing in the afternoon. On the contrary, the LFC goes down while the LNB moves up so that the distance between each other increases. Under drier soil condition, more sensible heat flux is added into the ABL which thus grows faster and crosses the LCL earlier. However, the distance between the LFC and LNB increases slower than under wetter soil conditions. Due to the continuous supply of water from the surface, the LCL stays low causing a faster increase in CAPE (Figure 17). This specific atmosphere could be classified as "dry soil advantage" atmosphere in terms of LCL crossing as earlier crossing is possible under dry soil condition, but could also be classified as "wet soil advantage" atmosphere in terms of CAPE as the simulations show higher CAPE under wet soil condition. This contrasting pattern will be further explored under more comprehensive atmospheric conditions.

Clouds may be assumed to develop as soon as the ABL crosses the LCL. At this time the state of ABL is critical for the following development of potential deep convection. For example, an early LCL crossing ensures that solar radiation is still available to sustain the continued convection. By investigating the timing of the initiation of moist convection, Gentine et al. (2013) found that both wet soil and dry soil may be conducive to early moist convection depending on atmospheric conditions, meaning that both positive and negative feedbacks could exist under particular atmospheric conditions. Other than the timing of moist convection, the amount of accumulated convective potential energy as CAPE at that time determines whether the ABL is well-prepared for the following development of deep convection. As a general rule of thumb, CAPE larger than $400 \text{JKg}^{-1}$ is required (Findell and Eltahir 2003b) and this empirical threshold will be used here as a criterion for deep convection along with the LCL crossing.
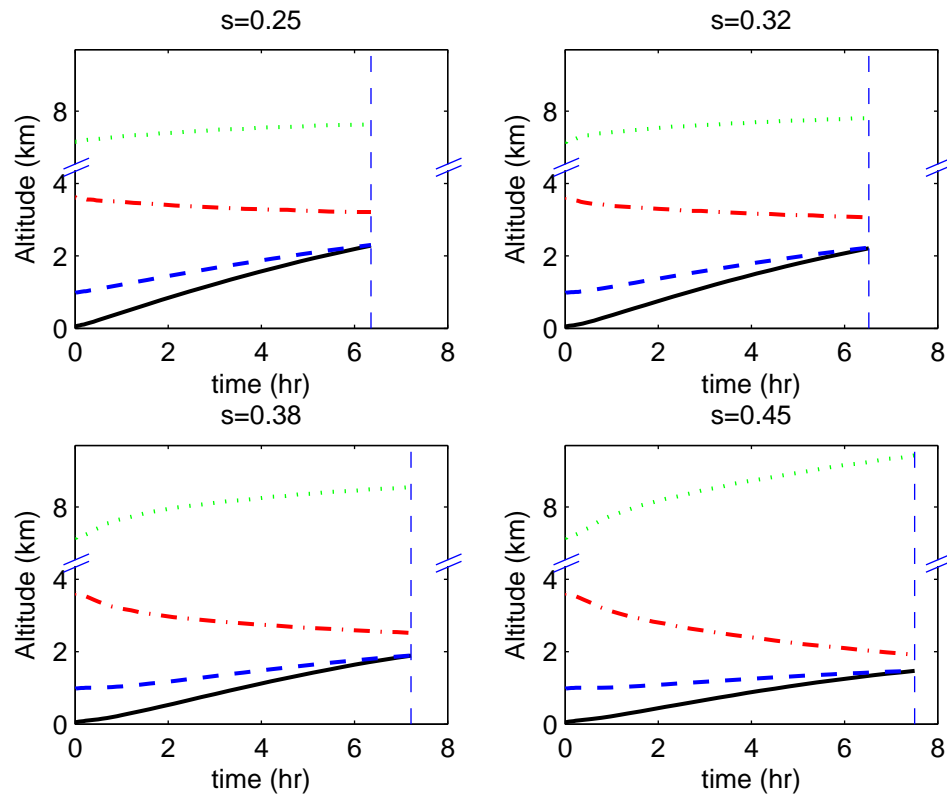
**Figure 16. ABL (black solid), LCL (blue dash), LFC (red dash-dot), and LNB (green dot) evolution under different soil moisture conditions. The vertical thin dash lines mark the LCL crossing time. Note that the y axis has been cut between 4 and 6 to facilitate comparison of the evolution of the different altitudes. Parameters are the same as in Figure 15.**
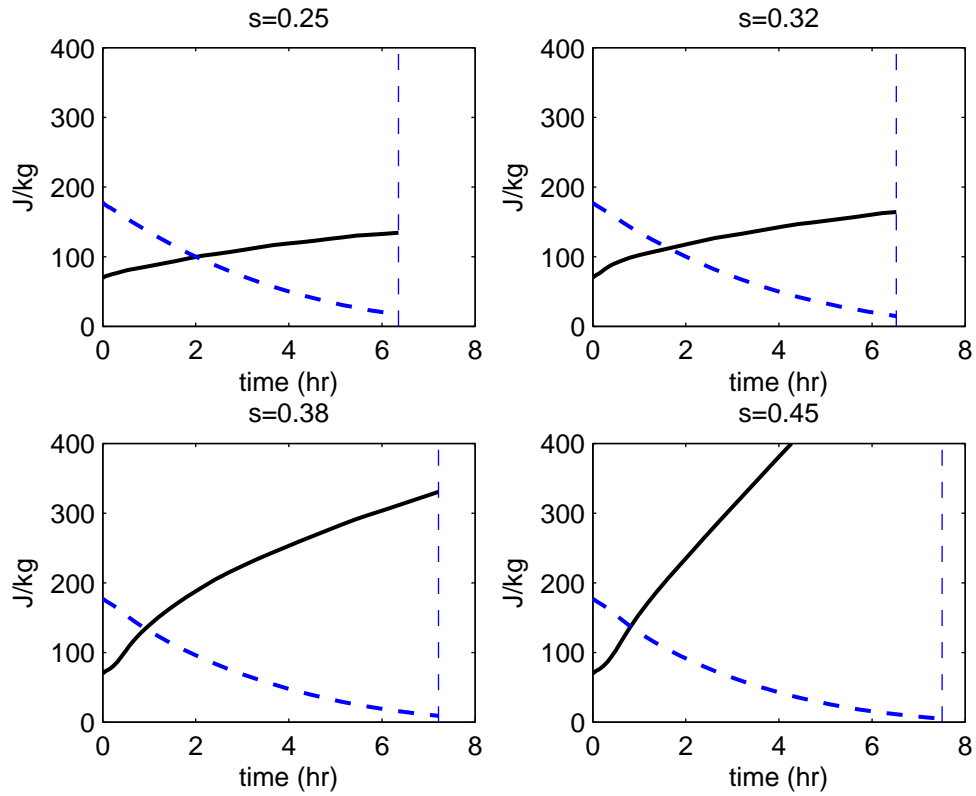
**Figure 17. CAPE (black solid) and CIN (blue dash) evolution under different soil moisture conditions. The vertical thin dash lines mark the LCL crossing time. Parameters are the same as in Figure 15.**

## 4.3.3 Soil moisture and atmosphere controls on moist convection: classification of different regimes

The previous section referred only to one specified atmospheric condition. In this

section we explore the effect of free atmospheric conditions. To constrain the parameter

space, we employ the linear relationship between slope and surface values for the free

atmospheric profiles presented in Figure 14, which allows us to account for a

comprehensive range of atmospheric conditions through the analysis of the parameters $\gamma_q$ and $\gamma_{\theta_v}$ under different soil moisture conditions.

Regimes for the conditions of the LCL crossing and the CAPE at the time of the crossing (or at the end of the day if there is no crossing) are presented in Figure 18 and Figure 19, and are summarized in Table 3. When atmospheric conditions are within regime I, the CAPE is larger than 400 J kg$^{-1}$ at the end of the day but the ABL does not cross the LCL. Within regime II, the CAPE is too low at the end of the day while ABL still does not cross the LCL. In regime III, ABL crosses the LCL but the CAPE is too low (<400 J kg$^{-1}$) at the crossing time. Only when the atmospheric conditions are within regime IV, is deep convection likely to be triggered, since the CAPE is large enough when the ABL crosses the LCL.

The analysis of these four regimes as a function of free atmospheric parameters for different soil moisture conditions is presented in Figure 18. In general, the four regimes map onto four quadrants, corresponding to unstable-and-dry, stable-and-dry, stable-and-wet, and unstable-and-wet atmosphere. Particularly in regime IV, when the lower atmosphere is stable (large $\gamma_{\theta_v}$) and moist (small $\gamma_q$), the ABL grows slowly but efficiently accumulates moisture, thus facilitating the LCL crossing (bottom right of regime IV), while with unstable and dry free atmosphere (dry near the surface but wet at higher elevations), the moist convection still can be triggered in the dry soil condition,

which partitions enough amount of sensible heat flux and thus accelerates the growth of

ABL to reach the LCL (top left of regime IV in *s* = 0.25 and *s* = 0.32).
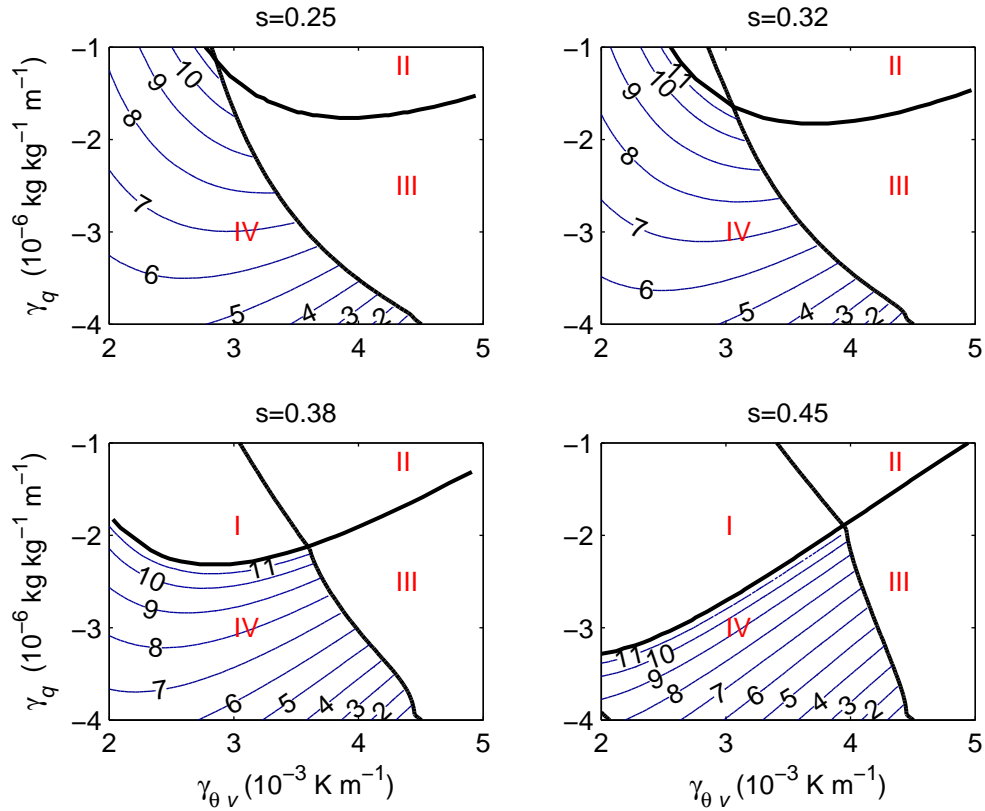


**Figure 18. LCL crossing time under different soil moisture and atmospheric conditions. Labeled contour lines represent the hour after sunrise that LCL crossing occurs. No crossing occurs in regions I-III. Classification of regime I, II, III, and IV is described in Table 3.**

**Table 3 Regime classification of atmospheric conditions as in Figure 18 and Figure 19 based on the LCL crossing and the CAPE at the time of the crossing (or end of the day if there is no crossing).**

| Regime | LCL Crossing | CAPE |
|--------|--------------|------|
| I | No | >400 J kg$^{-1}$ |
| II | No | <400 J kg$^{-1}$ |
| III | Yes | <400 J kg$^{-1}$ |
| IV | Yes | >400 J kg$^{-1}$ |

The values of CAPE at the time of LCL crossing corresponding to Figure 18 are presented in Figure 19. As can be seen, the CAPE and the LCL crossing time show different patterns with respect to atmospheric conditions. While the ABL can cross the LCL earlier under either wetter or drier soil (Figure 18), the CAPE seems always larger under wetter soil conditions (Figure 19). Besides the soil conditions, the free atmosphere can also influence the intensity of convection and the CAPE becomes larger when the lower atmosphere is wetter and more unstable (small $\gamma_q$ and small $\gamma_{\theta_v}$). The empirical CAPE threshold does not qualitatively change the general location of regimes I, II, III, and IV. For example, if the threshold becomes 300 J Kg$^{-1}$, the boundaries between regimes I and II and between regimes III and IV will follow the CAPE contours and slightly move to the right, leading to a corresponding expansion of regimes I and IV and a contraction of regimes II and III. If the threshold is increasing to 500 J Kg$^{-1}$, the boundaries will slightly move to the left and have opposite effects on the area of the regime.

Due to these contrasting patterns between the CAPE and the LCL crossing, we will analyze their joint dynamics next to understand the possible conditions that favor convective precipitation.
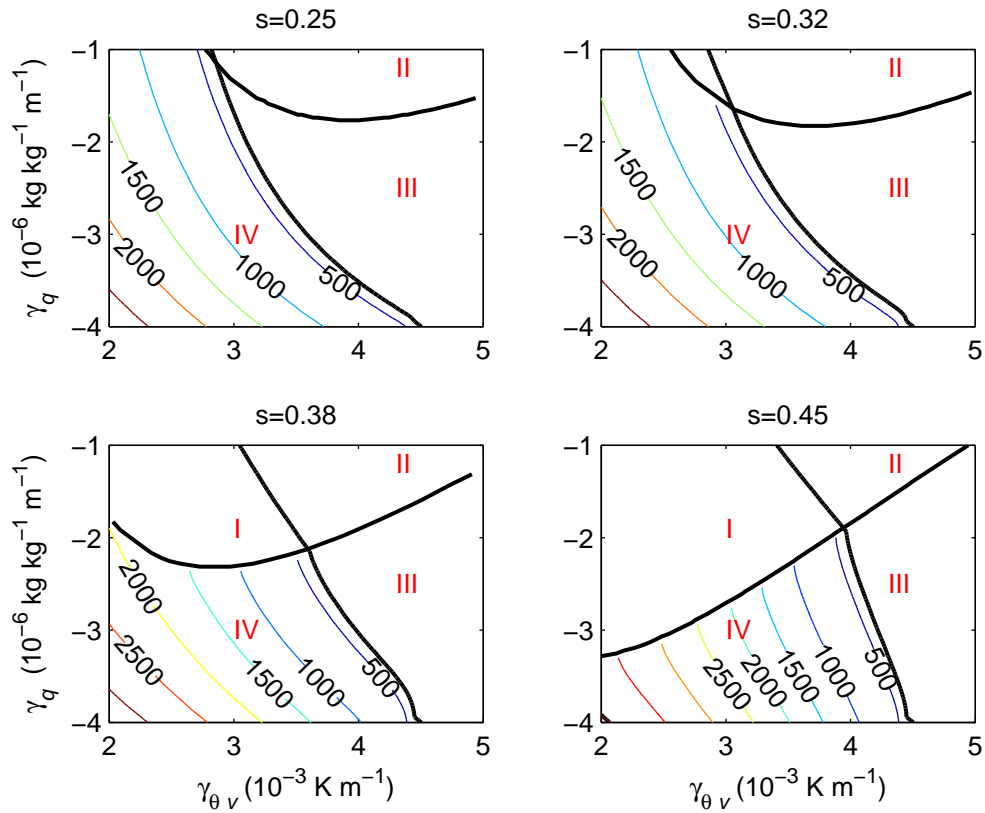


**Figure 19. CAPE levels at the LCL crossing time for four different soil moisture conditions as a function of free atmospheric conditions. The thick solid lines divide the atmospheric conditions into four regimes I, II, III, and IV based on the LCL crossing and the CAPE, which are explained in Table 1. Contours in regime IV represent the CAPE at the time of LCL crossing in units of J kg$^{-1}$. Note that the CAPE contours do not follow the crossing time contours of Figure 18.**

## 4.3.4 Soil moisture sensitivity to the moist convection

As shown in the previous sections, earlier LCL crossings are not necessarily accompanied by larger CAPE and in general both of the two indicators should be taken into consideration. Given their possible contrasting tendencies, it may be expected that the strongest convection will be triggered when a specific soil moisture value is such that it corresponds to the highest CAPE while still allows the ABL to cross the LCL during the daytime. We will indicate this soil moisture corresponding to maximum convection as $s_{max}$ and study its behavior as a function of free atmospheric conditions.

Figure 20 shows the LCL crossing time (solid lines) and the corresponding CAPE (dash lines) as a function of soil moisture under four types of atmospheric conditions. Figure 20 (a) shows that ABL can cross LCL only when soil is dry ($s < 0.34$), while CAPE increases as the soil becomes wetter, indicating the dry soil could potentially trigger the strongest deep convection ($s_{max} = 0.34$). Figure 20 (b) shows the similar pattern for an intermediate value of $s_{max}$. Figure 20 (c) and (d) show another type of atmospheric condition under which ABL always crosses LCL and CAPE increases as the soil become wetter, suggesting the wettest soil could trigger the strongest deep convection ($s_{max} = 0.5$).
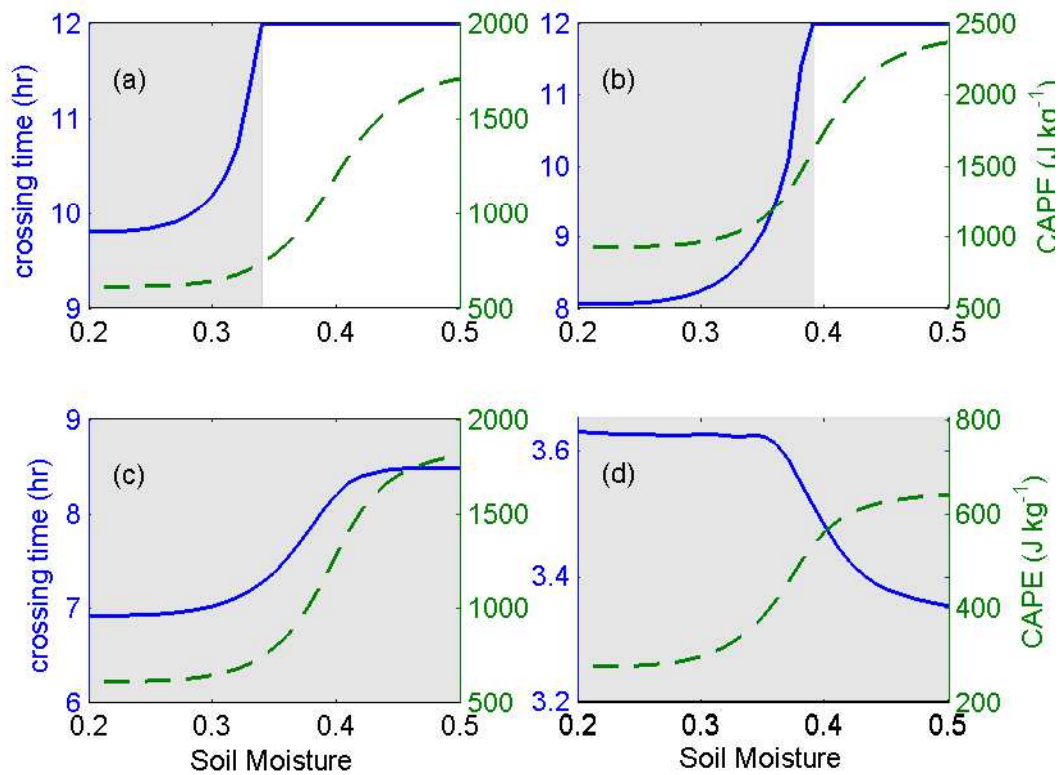
**Figure 20. LCL crossing time (solid lines) and CAPE (dash lines) as a function of soil moisture for four typical atmosphere conditions (a: $\gamma_{\theta_v}$ =2.7×10⁻³, $\gamma_q$ =-1.5×10⁻⁶; b: $\gamma_{\theta_v}$ =2.7×10⁻³, $\gamma_q$ =-2.4×10⁻⁶; c: $\gamma_{\theta_v}$ =3.3×10⁻³, $\gamma_q$ =-3×10⁻⁶; d: $\gamma_{\theta_v}$ =4×10⁻³, $\gamma_q$ =-3.5×10⁻⁶; these four cases are also represented in Figure 21 as star, circle, "x", and plus). The shaded area is the region where ABL is able to reach the LCL at the daytime.**

The soil moisture corresponding to the maximum convection ($s_{max}$) could be further used to classify the sensitivity of soil moisture to the moist convection. If $s_{max}$ is small (as in Figure 20 (a)), the specified atmosphere can be classified as a "dry soil advantage" atmosphere. If $s_{max}$ is large (as in Figure 20 (c and d)), the atmosphere can be classified as a "wet soil advantage" atmosphere. The intermediate case of Figure 20 (b)

can be classified as a "transitional" atmosphere. Other than comparing the simulated

rainfall occurrence only under the extreme wet and dry soil moisture cases (Findell and

Eltahir 2003b), this $s_{max}$ tests the whole range of soil moisture to provide a more accurate

soil moisture condition corresponding to maximum convection. This accurate $s_{max}$

involves a tradeoff between LCL crossing and the intensity of the convection and helps

identifying the nonlinearity of the feedbacks in the land-atmosphere interaction.

Based on the analysis of $s_{max}$, the atmospheric conditions can be divided into four

different zones as shown in Figure 21 and summarized in Table 4: in zone A, the ABL

cannot cross LCL under any soil moisture condition; in zone B, the ABL can cross LCL

under any soil moisture condition but the CAPE at the time of crossing is lower than 400

J kg$^{-1}$; in zone B', the ABL can cross LCL under certain soil moisture condition but CAPE

at the time of crossing is low; only in zone C, can the ABL cross LCL in the daytime with

a maximum CAPE larger than 400 J kg$^{-1}$, so that $s_{max}$ can be found. Unlike the

classification of atmosphere regimes in section 3.3 (Table 3), which is based on one

specified soil moisture condition, the classification of atmospheric zones in this section

(Table 4) considers the whole range of soil moisture to identify the state corresponding

to the maximum convection ($s_{max}$).

Figure 21 also marks four example atmospheric conditions as the star, circle, "x",

and plus, which are corresponding to the conditions illustrated in Figure 20 (a, b, c, and

d). As can be seen, when the unstable free atmosphere is dry near the surface but wet in

the higher altitude (large $\gamma_q$ and small $\gamma_{\theta_v}$, around the star mark), $s_{max}$ is small and a

negative feedback can be identified between the soil moisture and the moist convection.

When the lower atmosphere is moist (small $\gamma_q$, around the "x" and the plus), $s_{max}$ is

large and a positive feedback can be identified. When the lower atmosphere is unstable

and moist (small $\gamma_{\theta_v}$ and small $\gamma_q$, around the circle mark), $s_{max}$ is between dry and wet,

showing the nonlinear behavior of the feedback.
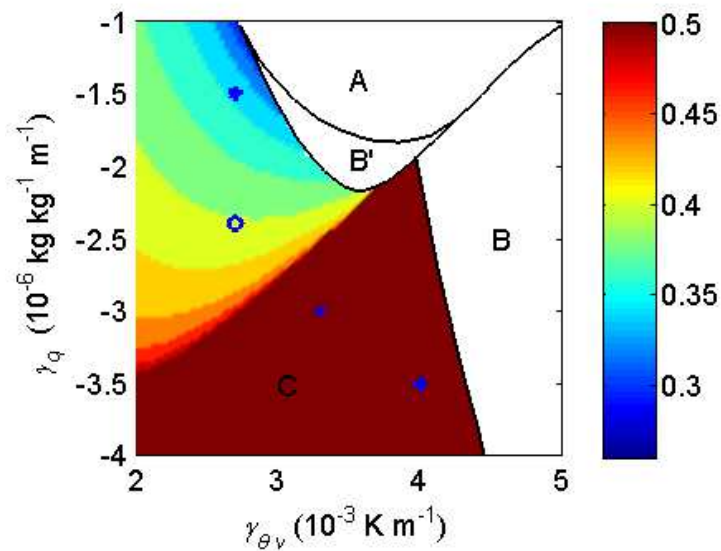


**Figure 21. Soil moisture corresponding to the maximum convection ($s_{max}$) under various atmospheric conditions. The star, circle, "x", and plus represent four corresponding atmosphere conditions in Figure 20 (a, b, c, and d). The thick solid lines divide the atmospheric conditions into four different zones A, B, B', and C, which are explained in Table 4.**

**Table 4 Atmospheric zones as in Figure 21 based the LCL crossing, and maximum CAPE at the time of the crossing.**

| Zone | LCL Crossing | Maximum CAPE |
|------|--------------|--------------|
| A | No, for any soil moisture | - |
| B | Yes, for any soil moisture | <400 J kg$^{-1}$ |
| B′ | Yes, for a range of soil moisture | <400 J kg$^{-1}$ |
| C | Yes, for a range of soil moisture | >400 J kg$^{-1}$ |

## 4.3.5 Moist convection under other atmospheric conditions

The atmospheric conditions treated above are under clear sky conditions and are limited to the regression relationships of temperature and humidity profiles as in Figure 14. Other conditions, such as those scatter points lying away from regression relationships or under cloudy sky, may show some variations in terms of the LCL crossing and CAPE.

When early morning clouds are above the newly-developed boundary layer, part of the solar radiation can be reflected and absorbed by the liquid water in the cloud. The reduction of radiation could not only delay the initiation of moist convection but also reduce the intensity of convection. As a result, the area of the atmospheric zone C, representing the possible deep convection zone, will shrink, indicating more difficulty to trigger deep convection.

If the atmospheric conditions are warmer than usual (e.g. increase $\theta_{f0}$), but with the same specific humidity profiles, the atmosphere will have a higher water vapor saturation capacity so that the LCL is higher and CAPE is lower than usual. For these

reasons, it is more difficult to trigger deep convection under the warmer-than-usual

atmosphere. Similarly, if the atmospheric conditions are wetter than usual (e.g. increase

$q_{f0}$), but with the same temperature profiles, the atmosphere needs less water vapor to

become saturated so that the LCL is lower and CAPE can be higher than usual. The

wetter-than-usual atmosphere more easily triggers deep and strong convection.


## *4.4 Conclusions*

In this study, we embedded a soil-plant system within a mixed-layer model to

study the possible conditions that could lead to deep convection with consideration of

both the initiation of moist convection (LCL crossing) and the convective energy (CAPE

threshold). Based on the free atmosphere conditions in Central Facility, Southern Great

Plains, we found that a dry atmosphere tends to suppress moist convection and stable

atmosphere tends to have less convective energy. Moist convection can be triggered

earlier when the atmosphere is more stable and wetter, which allows the ABL to grow

slowly but efficiently accumulate moisture, thus facilitating the LCL crossing. CAPE is

found to be always larger over the wetter surface, which provides abundant moisture

content to lower the LCL and increase the buoyancy of the lifted air parcel.

By combining a CAPE threshold condition to the traditional binary criterion of

crossing/no-crossing of the LCL, our analysis defines four different atmospheric regimes

and map their existence as a function of the boundary conditions (i.e., soil moisture and

properties, plant and free atmosphere parameters), contributing to illustrate the complicated dependence of boundary-layer dynamics and deep convection on soil moisture and atmospheric conditions. We also investigated the soil moisture corresponding to the maximum potential convection (i.e., the largest CAPE at time of LCL crossing), which provides an improved criterion to identify which soil moisture condition favors the strongest convection following the spirit of the work by Findell and Eltahir (2003b). Such a distinction contributes to make more precise previous categorization of atmospheric conditions (e.g., Juang et al. (2007a); Siqueira et al. (2009); Gentine et al. (2013)) regarding the so-called dry or wet soil-advantage for triggering convection. For example, while previous work identified the dry soil advantage only in terms of LCL crossing (e.g., Figure 20 c), from our analysis it become clear that these atmospheric conditions should instead be identified as wet soil advantage when considering also that CAPE is always higher under wet soil conditions.

Finally, it should be kept in mind that this study has been focused on the development of the ABL and CAPE only up to the LCL crossing and has been limited to the linearized sounding profiles. It will be interesting in future work to go beyond these simplifications and especially to include the dynamics of the cloud-topped boundary layer to link the CAPE at LCL crossing to the actual onset and development of free convection. With longer timescales in mind, the result of this work may be used to extend add physical content in terms of simplified representations of convective rainfall

74

to the rainfall parameterization in stochastic soil moisture models (D'Odorico and

Porporato 2004; Porporato and D'Odorico 2004; Yin et al. 2014).

# 5. An Analysis of Cloud-Topped Atmospheric Boundary Layer

## 5.1 Introduction

While cloud free mixed-layer models have been extensively used for simulating atmospheric convection, land-atmosphere interaction, air pollutant transport, and other activities within the lowest part of the atmosphere (Garratt 1992; Juang et al. 2007a; Porporato 2009; Siqueira et al. 2009; Konings et al. 2010), these models are no longer valid when the top of the boundary layer reach the lifting condensation level (LCL) and convective cloud is formed. Cloud-topped boundary layer models, such as developed by Lilly (1968), are needed for modeling the emergence of cloud and its influence on the radiation and boundary-layer dynamics. These clouds not only influence the local boundary-layer development but also remain the largest source of uncertainty in global climate system due to the dual role that they play in the earth's energy budget system: shading the solar radiation and absorbing longwave radiation (Zhang et al. 2013). Consequently, it is important to address all important radiation components and feedbacks in the cloud when the top of the boundary layer becomes saturated.

Among all the effects due to the emergence of cloud, the radiative and evaporative cooling effects are thought to be two important factors that could significantly influence the turbulence kinetic energy in the boundary layer (Stull 1988;

Garratt 1992; Shao et al. 1997). Radiative cooling near the cloud top due to the net longwave radiation loss to the atmosphere creates upside-down thermals of cold air for the entrainment of relatively buoyant air into the mixed layer. This cooling effect has been parametrized to model the boundary-layer growth in many cloud-topped boundary layer models (Lock 1998; Lock and Macvean 1999; Moeng et al. 1999; Pelly and Belcher 2001; Lilly 2002b, 2002a). However, research on the effects of evaporative cooling on boundary-layer growth is focused on the buoyancy change during the mixing between the dry air in the free atmosphere and cloud in the top of the boundary layer, which is termed cloud-top entrainment instability (CTEI) (Deardorff 1980; Randall 1980). Less effort has been putting into modeling the effects of instability on the boundary layer development. Since both radiative and evaporative cooling effects show similar upside-down pattern of thermal, it is possible that there might be some coherent parameterization structure which is suitable for both of the evaporative and radiative cooling.

In this study, we try to summarize each components of radiation within the cloud and explore the similarity in parametrizing the radiative and evaporative cooling effects on the boundary-layer growth. The cloud-topped boundary layer model is then used to analyze the transition from shallow to deep convection when the top the boundary layer become unstable according to the CTEI criteria. Based on the development of the boundary layer and clouds, this chapter is organized as follows:

77

section 2 reviews the cloud free ABL, section 3 introduces the cloud-topped boundary layer, section 4 analyzes the different outcome when the top of the boundary layer becomes unstable, section 5 explains cumulus development and cloud mixing with surrounding dry air.

## *5.2 Cloud-free ABL*

When atmosphere boundary layer (ABL) does not reach the lifting condensation level (LCL), the atmosphere is clear without cumulus. The behaviors of this atmosphere can be modeled by zero-order mixed-layer or slab models assuming constant potential temperature and specific humidity throughout the ABL (Betts 1973; Tennekes 1973; Porporato 2009).

In the mixed layer model, the vertical profiles of $\theta$ and $q$ are assumed to be constant within the boundary layer and have instant inversion $\Delta\theta$ and $\Delta q$ at the top of the boundary layer,

$$\Delta\theta = \theta_f(h) - \theta$$
$$\Delta q = q_f(h) - q \tag{49}$$

where the subscript $f$ indicates the variables in the free atmosphere.

For potential temperature within ABL ($\theta$), the first law of thermodynamics gives,

$$\rho c_p h \frac{d\theta}{dt} = H + \rho c_p \Delta\theta \frac{dh}{dt}, \tag{50}$$

where $\rho$ is the air density, $c_p$ is the specific heat of air, $h$ is the height of ABL, $H$ is sensible heat flux. For specific humidity within ABL ($q$), the law of conservation of mass gives,

$$\rho h \frac{dq}{dt} = E + \rho \Delta q \frac{dh}{dt} , \tag{51}$$

where $E$ is evapotranspiration.

At the top of the mixed layer, the virtual potential temperature flux is often modeled as (Tennekes 1973),

$$-(\overline{w'\theta_v'})_h = \beta_0 A_0 + \beta_1 A_1 = \beta_0 \frac{T_0 u_*^3}{gh} + \beta_1 (\overline{w'\theta_v'})_s , \tag{52}$$

where $g/T_0$ is the buoyancy parameter, $u_*$ is the surface friction velocity, and $\beta_0$ and $\beta_1$ are parameters. The first term on the right-hand side is the contribution to the entrainment from mechanical turbulence while the second is the contribution from the buoyancy-driven turbulence. A linear combination of these two turbulences is used to parameterize the buoyancy flux at the top of the boundary layer. Equations (52) close the equations (49)-(51) and can be used to simulate the dynamics of the boundary layer before the initiation of cloud.

## *5.3 Cloud-topped Boundary Layer*

When ABL reach the LCL, the top of the boundary layer becomes saturated. The emergence of cloud redistribute both the longwave and shortwave radiation. This

change could significantly influence the entrainment at the top of the boundary layer

and the boundary-layer dynamics. In this section, we first summarize the radiation in

the cloud and then analyze parametrization for evaporative and radiative cooling effects

on the growth of ABL.

## 5.3.1 Energy Budget
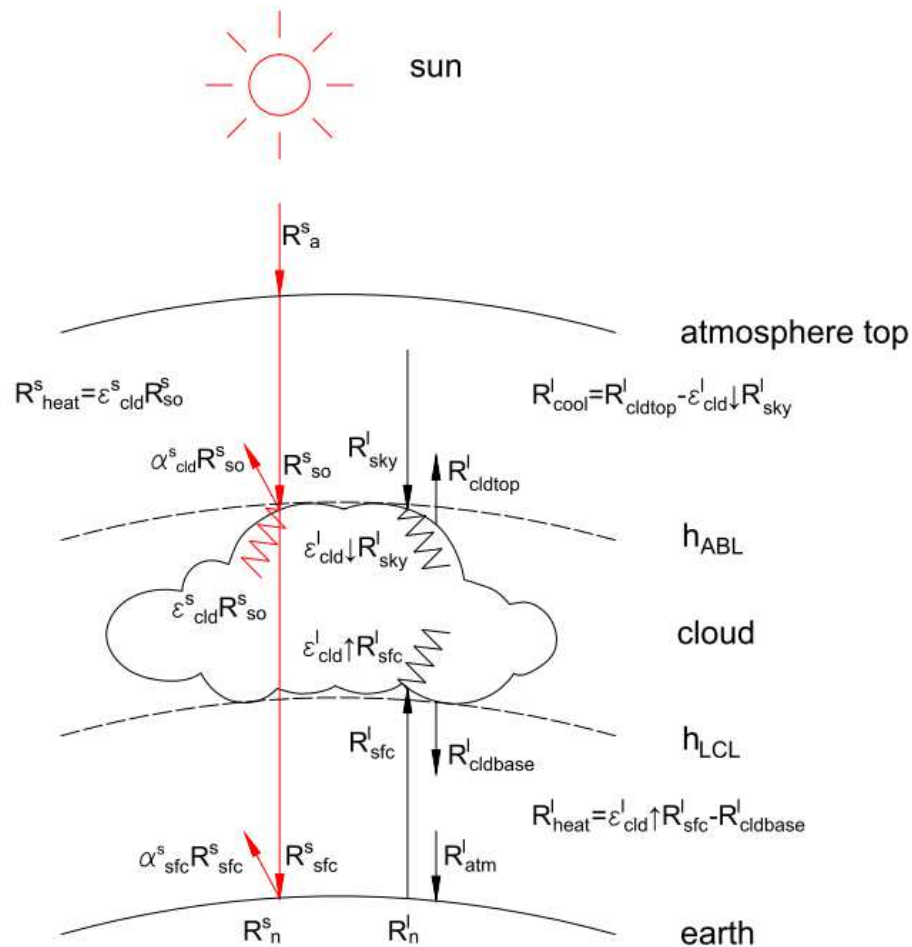


**Figure 22 Components of radiation (red arrows are shortwave radiation, black arrows are longwave radiation)**

*Shortwave radiation*

Figure 22 shows various components of radiation. The extraterrestrial solar radiation ($R_a^s$) is the local solar radiation at the top of the atmosphere, which is a function of solar constant and the angle between the sun's rays and the normal to the surface. Even in the clear sky, only a fraction of the radiation can penetrate the atmosphere ($R_{so}^s$). On cloudy days, the radiation is reflected and absorbed by the water in the cloud and the rest ($R_{sfc}^s$) reaches the earth's surface,

$$R_{sfc}^s = R_{so}^s(1 - \alpha_{cld}^s - \varepsilon_{cld}^s) , \tag{53}$$

where $\alpha_{cld}^s$ is cloud shortwave albedo and $\varepsilon_{cld}^s$ is cloud shortwave absorptivity, both of which are generally determined by the liquid water in the cloud and solar zenith angle but could be also related to the other cloud characteristics such as cloud drop-size (Stephens 1978), and $R_{sfc}^s$ is the rest of the solar radiation reaching the earth's surface. This solar radiation is also reflected on the ground, and the remaining is net shortwave radiation ($R_n^s$),

$$R_n^s = (1 - \alpha_{sfc}^s)R_{sfc}^s , \tag{54}$$

where $\alpha_{sfc}^s$ is surface shortwave albedo.


*Longwave radiation*

Besides shortwave radiation, longwave radiation also plays an important role in the energy budget. Net longwave radiation ($R_n^l$) in Figure 22 is the outgoing longwave radiation from earth's surface ($R_{sfc}^l$) deducted by the downward longwave radiation from the above atmosphere ($R_{atm}^l$).

$$R_n^l = R_{sfc}^l - R_{atm}^l.$$ (55)

The outgoing radiation ($R_{sfc}^l$) is proportional to the four power of absolute temperature of earth surface, while the incoming radiation from the above atmosphere ($R_{atm}^l$) is not only influenced by sky temperature but also controlled by absorbers and emitters such as water vapor, carbon dioxide, and ozone.

*Soil heat flux*

Both the net shortwave and longwave radiations can be utilized in heating the soil ($G$), and the rest is the net available energy ($Q$), which is then partitioned into latent and sensible heat flux,

$$Q = (R_n^s - R_n^l) - G = H + \lambda E,$$ (56)

where $E$ is evapotranspiration, $\lambda$ is latent heat of vaporization, $H$ is sensible heat flux.

*Radiation exchange in cloud*

Within the cloud, there are three types of cooling or heating effects: the heating effects from the shortwave radiation absorption at the cloud top ($R^s_{heat}$), the longwave radiative cooling at the cloud top ($R^l_{cool}$), and the longwave radiative heat at the cloud base ($R^l_{heat}$). These effects due to the emergence of cloud may be important to the cloud-topped boundary layer and are discussed here in detail.

Near the cloud top, the absorption of shortwave radiation depends on the incoming solar radiation and the shortwave emissivity,

$$R^s_{heat} = \varepsilon^s_{cld} R^s_{so},$$ (57)

where $\varepsilon^s_{cld}$ is the shortwave absorptivity as in (53). This shortwave heating is not alone near the cloud top and coexists with the longwave radiative cooling, which is the sum of upward and downward longwave radiation,

$$R^l_{cool} = R^l_{cldtop} - \varepsilon^{l\downarrow}_{cld} R^l_{sky},$$ (58)

where $\varepsilon^{l\downarrow}_{cld}$ is the downward longwave absorptivity, and $R^l_{cldtop}$ is the cloud top upward longwave radiation, which is determined by the upward longwave emissivity ($\varepsilon^{l\uparrow}_{cld}$) and the temperature near the cloud top ($T_{cldtop}$),

$$R^l_{cldtop} = \varepsilon^{l\uparrow}_{cld} \sigma T^4_{cldtop}.$$ (59)

According to Kirchhoff's law of thermal radiation, the upward or downward longwave absorptivity equal their corresponding emissivity and both can be modeled as functions of liquid water path (Stephens 1978),

$$\varepsilon_{cld}^{l\uparrow} = 1 - \exp(-a_0^{\uparrow}W)$$

$$\varepsilon_{cld}^{l\downarrow} = 1 - \exp(-a_0^{\downarrow}W),$$

(60)

where $a_0^{\downarrow}$ and $a_0^{\uparrow}$ are the mass absorption coefficient for the longwave radiation, and $W$

is the liquid water path in the cloud,

$$W = \int_{P_{ABL}}^{P_{LCL}} q_L / g \, dp \,,$$

(61)

where $q_L$ is the liquid water content, $p_{LCL}$ and $p_{ABL}$ are the pressure at cloud base (LCL)

and cloud top (ABL top) respectively, and $g$ is the gravitational acceleration. The overall

radiation at the cloud top usually has the cooling effect,

$$R_{cool} = R_{cool}^{l} - R_{heat}^{s} \,,$$

(62)

This cooling effect can accelerate the entrainment of the cloud-top ABL and play an

important role in controlling the transition from shallow to deep convection.

Near the cloud base, the longwave radiative heating ( $R_{heat}^{l}$ ) is much less than the

longwave radiative cooling at the cloud top ( $R_{cool}^{l}$ ) under most circumstances. This

heating source may slightly warm up the boundary layer but has negligible impacts on

the turbulence generation (Stage and Businger 1981; Rogers et al. 1985; Stull 1988).

Similar to the longwave radiative cooling ( $R_{cool}^{l}$ ) near cloud top, the net heating ( $R_{heat}^{l}$ )

near the cloud base is the difference between the upward longwave radiation absorption

( $\varepsilon_{cld}^{l\uparrow} R_{sfc}^{l}$ ) and the downward longwave radiation loss ( $R_{cldbase}^{l}$ ).

$$R_{heat}^{l} = \varepsilon_{cld}^{l\uparrow} R_{sfc}^{l} - R_{cldbase}^{l}, \qquad (63)$$

where downward radiation loss near the cloud base is determined by the downward

longwave emissivity ($\varepsilon_{cld}^{l\downarrow}$) and the temperature near the cloud base ($T_{cldbase}$),

$$R_{cldbase}^{l} = \varepsilon_{cld}^{l\downarrow} \sigma T_{cldbase}^{4}, \qquad (64)$$

## 5.3.2 Vertical Profiles

When the top of the mixed layer reaches the LCL, the boundary-layer dynamics

and turbulence generation are modulated by radiation within the cloud, latent heat

transfer, and water phase changes. In this case, liquid water potential temperature and

the total water content are still conserved under both dry and moist adiabatic processes

and are often used to study the cloud-topped ABL (Lilly 1968; Stage and Businger 1981;

Driedonks and Duynkerke 1989; Pelly and Belcher 2001). For the boundary layer

purpose, the liquid water potential temperature can be expressed with sufficient

accuracy as,

$$\theta_{L} = \theta - \lambda / c_{p} q_{L}, \qquad (65)$$

and the total water content is defined as,

$$q_{t} = q_{L} + q, \qquad (66)$$

where $q_{L}$ is the liquid water content.

In the mixed layer model, the vertical profiles of $\theta_L$ and $q_t$ are assumed to be constant within the boundary layer ($z < h$) and have sharp jumps $\Delta\theta_L = \theta_{Lf}(h) - \theta_L$ and $\Delta q_t = q_{tf}(h) - q_t$ at the top of the boundary layer ($z = h$). In the sub-cloud layer ($z < z_{LCL}$), the potential temperature ($\theta$) equals the liquid water potential temperature ($\theta_L$), while specific humidity ($q$) equals total water content ($q_t$). In the cloud layer ($z_{LCL} < z < h$), the latent heat release (LHR) from condensation (CDS) warms up the air and thus leads to the difference between $\theta$ and $\theta_L$ and the condensation itself results in the difference between $q$ and $q_t$. These differences peak at the top of the boundary layer and can be expressed as,

$$\Delta\theta = \Delta\theta_L - \lambda/c_p q_L(h)$$

$$\Delta q = \Delta q_t + q_L(h)$$

(67)

where $q_L(h)$ is the liquid water content at the top of the boundary layer. In the cloud layer, liquid water and water vapor coexist, indicating the air is saturated,

$$q(z) = q_{sat}(T(z)), \qquad (68)$$

where $q_{sat}$ is saturated specific humidity at corresponding temperature which is determined from the Clausius-Clapeyron relationship. From above equations (65)-(68), one can find that the sounding profiles follow dry adiabatic process in the sub-cloud layer and follow moist adiabatic process in the cloud layer.

**Figure 23. Schematic representation of the vertical profiles of liquid water potential temperature and total water content for the mixed-layer CTBL model**

### 5.3.3 Conservation Equations

Following Garratt (1992), the conservation of liquid water potential temperature in the cloud-topped boundary layer is,

$$\rho c_p h \frac{d\theta_L}{dt} = \rho c_p (\overline{\theta_L ' w'})_{sfc} + \rho c_p \Delta\theta_L \frac{dh}{dt} - R_{cool}^l + R_{heat}^s + R_{heat}^l , \qquad (69)$$

where $\theta_L$ is the mean liquid water potential temperature throughout the boundary layer, $R_{cool}^l$, $R_{heat}^s$, and $R_{heat}^l$ are the three sources of radiation within the cloud as discussed in the previous section, and the near-surface turbulent flux of liquid water

potential temperature is simply sensible heat flux since there is no near-surface liquid

water flux ($(q_L')_{sfc} = 0$),

$$\rho c_p \overline{(\theta_L' w')}_{sfc} = \rho c_p \overline{(\theta' w')}_{sfc} - \rho \lambda \overline{(q_L' w')}_{sfc} = \rho c_p \overline{(\theta' w')}_{sfc} = H \; . \tag{70}$$

Similarly, the conservation of total specific humidity in the cloud-topped

boundary layer is,

$$\rho h \frac{dq_t}{dt} = E + \rho \Delta q_t \frac{dh}{dt} , \tag{71}$$

where $q_t$ is the mean total water content throughout the boundary layer.

### 5.3.4 Evaporative cooling

Other than the radiative cooling as discussed in previous section, evaporative

cooling due to the mixing of dry air and saturated air across the boundary layer top

could also play an important role in the boundary layer growth. On one hand,

evaporative cooling, similar to the radiative cooling, creates upside-down thermals of

cold air for the entrainment of relatively buoyant air into the mixed layer (Garratt 1992;

Lilly 2002a). On the other hand, during the entrainment process, mixed air can have

heavier density than its mixing components under certain conditions, making the cloud

unstable even when the buoyancy inversion still exists (Lilly 1968; Deardorff 1980;

Randall 1980). Before studying both of these effects, we first summarize factors that

influence the amount of evaporative cooling rate.

From physical point of view, the evaporative cooling rate ($R_V$) should be proportional to the vaporized liquid water content and the speed of mixing,

$$R_V \propto \left( \lambda / c_p q_{LV} \right) \times \left( \frac{dh}{dt} \right),$$ (72)

where $dh/dt$ is the ABL growth rate, representing the speed of mixing, and $q_{LV}$ is the vaporized liquid water content, which is the change of liquid water content before and after the mixing. The vaporization occurs at the cloud top, where the liquid water content before mixing is the liquid water content below the inversion ($q_L(h)$), and the liquid water content after the mixing is the liquid water content from the mixed air ($q_{LM}$),

$$q_{LV} = q_L(h) - q_{LM},$$ (73)

To further find the liquid water content after mixing ($q_{LM}$), conserved variable thermodynamic diagram (Stull 1988) is used. Consider one unit mass of mixed air consisting of $\chi$ units of air above the inversion with humidity and temperature states [$q_{tf}(h)$, $\theta_{Lf}(h)$] and 1-$\chi$ units of air below the inversion with the states [$q_t(h)$, $\theta_L(h)$]. The final states of mixed total water content ($q_{tM}$) is,

$$q_{tM} = \chi q_{tf}(h) + (1 - \chi) q_t(h),$$ (74)

and the mixed liquid water potential temperature is,

$$\theta_{LM} = \chi \theta_{Lf}(h) + (1 - \chi) \theta_L(h),$$ (75)

For typical stratocumulus clouds, the mixed air is saturated only when $\chi$ is very small ($\chi < 0.1$) (Albrecht et al. 1985). During the growing of the cloud-topped boundary

layer, various type of cloud mixing are expected with $\chi$ ranged from 0 to 1. It is possible that only a small amount of the mixing with small value of $\chi$ has remaining liquid water that are not vaporized, which can be calculated by the states of humidity and temperature from (74) and (75). Most of the mixing ends up with unsaturated air, indicating most of the liquid water in the cloud are vaporized,

$$q_{LM} \approx 0 . \tag{76}$$

Substitution of (76) and (73) into (72) shows the evaporative cooling rate ($R_V$) is related to the cloud-top liquid water content.

## 5.3.5 Entrainment

In the absence of cloud, mechanic turbulence ($A_0$) and surface buoyancy flux ($A_1$) and are the primary driving forces for the free convection and the buoyancy flux at the top of the boundary layer is parameterized in (52). When cloud is formed, the radiative divergence in the cloud combined with evaporative cooling due to the dry air entrainment from free atmosphere moderates the boundary-layer dynamics and entrainment flux. Due to the emergence of cloud, we are expecting to model the buoyancy flux at the top of boundary layer as,

$$-(\overline{w'\theta_v'})_h = f(A_0, A_1, A_2, A_3) , \tag{77}$$

where $A_2$ is the radiative cooling near the top of the cloud ($A_2 = R_{cool}/\rho c_p$) and $A_3$ is the evaporative cooling due to the dry air entrainment from free atmosphere ($A_3 = R_V$), both

90

of which could enhance the buoyancy flux at the top of the boundary layer and possibly accelerate the boundary layer growth.

Combining with the mechanical turbulence and buoyancy-driven turbulence as in (52), the radiative cooling and evaporative cooling due to the cloud emergence may contribute to the entrainment at the cloud top. Following the simple entrainment scheme as was conducted by Tennekes (1973) for the cloud-free boundary layer, we parameterize the entrainment for the cloud-topped boundary layer as a linear combination from all the possible contributions,

$$
\begin{aligned}
-(\overline{w'\theta_v'})_h &= \beta_0 A_0 + \beta_1 A_1 + \beta_2 A_2 + \beta_3 A_3 \\
&= \beta_0 \frac{T_0 u_*^3}{gh} + \beta_1 (\overline{w'\theta_v'})_s + \beta_2 \frac{R_{cool}}{\rho c_p} + \beta_3 \frac{\lambda q_{LV}}{c_p}\left(\frac{dh}{dt}\right),
\end{aligned}
\tag{78}
$$

where $\beta_2$ and $\beta_3$ are the parameters.

With thin inversion layer assumption, the integration of heat flux budget equations (with vertical advection term included) across the inversion gives a simple form of buoyancy flux for entrainment (Garratt 1992; Lock and Macvean 1999; Moeng et al. 1999; Lilly 2002a),

$$
-(\overline{w'\theta_v'})_h = \Delta\theta_v\left(\frac{dh}{dt} - w_L\right),
\tag{79}
$$

where $(\overline{w'\theta_v'})_h$ is the buoyancy flux at the inversion, $w_L$ is the mean large-scale vertical motion, and $\theta_v$ is virtual potential temperature which provides a measurement of air density.

Substitution (79) into (78) gives,

$$\frac{dh}{dt}\left(\Delta\theta_v - \beta_3 \frac{\lambda}{c_p} q_{LV}\right) = \beta_0 \frac{T_0 u_*^3}{gh} + \beta_1 (\overline{w'\theta_v'})_s + \beta_2 \frac{R_{cool}}{\rho c_p} + \Delta\theta_v w_L.$$  (80)

This governing equation for boundary-layer growth rate closes the whole system for the cloud-topped boundary layer. Given the initial boundary-layer temperature and humidity and the free atmosphere conditions, thermodynamic and energy budget equations can be used to calculate the cloud-topped boundary layer profiles, including LCL, inversion layer, cloud states, and long- and short-wave radiation flux, with which boundary-layer growth rate can be evaluated from equation (80). This growing rate, plus a latent-sensible heat flux partitioning scheme (e.g. soil-plant-atmosphere continuum), gives the increment of the boundary-layer temperature and humidity from equations (69) and (71) and so the whole evolution of the boundary layer.

Parameterizing the entrainment flux as a linear combination of every possible contribution factors as in (78) not only gives a simple and easy-to-track format for the boundary-layer growth but also helps understanding the cloud-top instability. By defining the expression in the bracket of the left hand side of equation (80) as adjusted virtual potential temperature inversion strength,

$$(\Delta\theta_v)_{adj} = \Delta\theta_v - \beta_3 \frac{\lambda}{c_p} q_{LV},$$  (81)

one can expect the growth rate of the boundary layer becomes infinity and the top of the cloud become unstable, when the adjusted virtual potential temperature inversion approaches the singularity point $(\Delta\theta_v)_{adj} = 0$.

This adjusted virtual potential temperature inversion strength $(\Delta\theta_v)_{adj}$ is similar to the cloud-top entrainment instability (CTEI) defined by Randall (1980) and Deardorff (1980) and refined by many others (see Appendix C). They show that under certain conditions the density of a mixed air from below and above the cloud top with proper mixing fraction $\chi$ can be larger than the density of either of the mixing components and thus leads to the self-sustained downdraughts. These CTEI criteria such as those in (C7), (C8), and (C9) are sensitive to the cloud-top liquid water content, making these criteria similar to the adjusted virtual potential temperature inversion defined in (81). Since both the CTEI and $(\Delta\theta_v)_{adj}$ serve the same purpose to judge the stability of the cloud-topped boundary layer, the well-studied CTEI criteria could tentatively replace $(\Delta\theta_v)_{adj}$ as we did here to model the boundary layer growth before the parameter $\beta_3$ in $(\Delta\theta_v)_{adj}$ is fully investigated.

Each contribution factor listed in (78) has various impacts on the entrainment flux and their corresponding parameters may have certain uncertainties. In the early morning, mechanic turbulence generated from surface shear stress has significant contribution to the entrainment flux and typical values of 2.5 and 5 for the corresponding parameter $\beta_0$ are found in the literature (Tennekes 1973; Driedonks

1982). After the morning transient, the buoyancy-generated turbulence from surface heat

flux could dominate the growth of the boundary layer and its parameter $\beta_1$ may range

from 0.1 to unity with a typical value of 0.2 (Ball 1960; Tennekes 1973; Stull 1976). When

the boundary layer reaches the LCL, radiative and evaporative cooling from cloud top

may accelerate the entrainment even though the surface heat flux is reduced due to the

shaded solar radiation from cloud. The linear parametrization scheme of radiative

cooling effects on entrainment rate has been used by in many studies with parameter $\beta_2$

varied from 0.28 to 0.63 (Lock and Macvean 1999; Pelly and Belcher 2001; Lilly 2002a).

The corresponding parameter $\beta_2$ and parameter $\beta_1$ should have close values as the

profiles of radiative cooling flux and surface heating flux are approximately the mirror

images (Lock and Macvean 1999; Lilly 2002a). The last entrainment parameter $\beta_3$ for

evaporative cooling is related to the instability of the boundary layer and can be

estimated in reference to the CTEI. Given that multiple criteria were suggested in many

studies (Nicholls and Turton 1986; Duynkerke 1993; Lilly 2002b; Yamaguchi and Randall

2008), it is likely that the parameters $\beta_3$ also has uncertainties as the other

parameters $\beta_0$, $\beta_1$, and $\beta_2$.


## 5.3.6 Model Testing

In the preceding section, we present a simple entrainment scheme for modeling

the boundary-layer growth and discuss the uncertainties of entrainment parameters. In

this section, we further test how these uncertainties will influence the cloud-topped

boundary-layer dynamics. Specifically, we focus on the period from the cloud initiation

to the time when the top of the boundary layer becomes unstable and test the

uncertainties of entrainment parameters for radiative and evaporative cooling effects.

We extend the model testing of cloud-free boundary layer in Chapter 4 to cloud-

topped boundary layer. The initial slope and surface values of temperature and

humidity are found in the radiosonde date in the summer early morning (0530 local

time) in Central Facility, Southern Great Plains (CF-SGP). The parameter $\beta_2$ for

radiative cooling could be varied from 0.28 to 0.63 in the research conducted by Lilly

(2002a), while CTEI from Nicholls and Turton (1986) and Duynkerke (1993) represent

two typical cloud-top mixing scheme. Here we test two sets of parametrization, one set

(S1) with $\beta_2 = 0.28$ and $(\Delta\theta_v)_{adj} = \Delta_{NT}$ and the other set (S2) with $\beta_2 = 0.63$ and

$(\Delta\theta_v)_{adj} = \Delta_D$. These two sets of parametrization provide two extreme scenarios that

describe the weak (S1) and strong (S2) effects of evaporative and radiative cooling on

cloud-top entrainment and boundary-layer growth rate.

Figure 24 and Figure 25 compare the timing from cloud initiation to cloud

breakup under different atmospheric conditions and soil moisture levels. In general, the

time needed to break up the cloud from its emergence is half hour to one hour. When

atmosphere is more unstable and wetter (smaller $\gamma_\theta$ and $\gamma_q$), it takes shorter time for

cloud to break up. The parametrization scheme S1, accounting for weak cooling effects

on boundary-layer growth, takes longer time to proceed to the cloud breakup than scheme S2. However, the timing for both schemes are close in most atmospheric and soil moisture conditions, except on the edge of transition from breakup and no breakup where it suddenly takes much longer time for the cloud to break up.
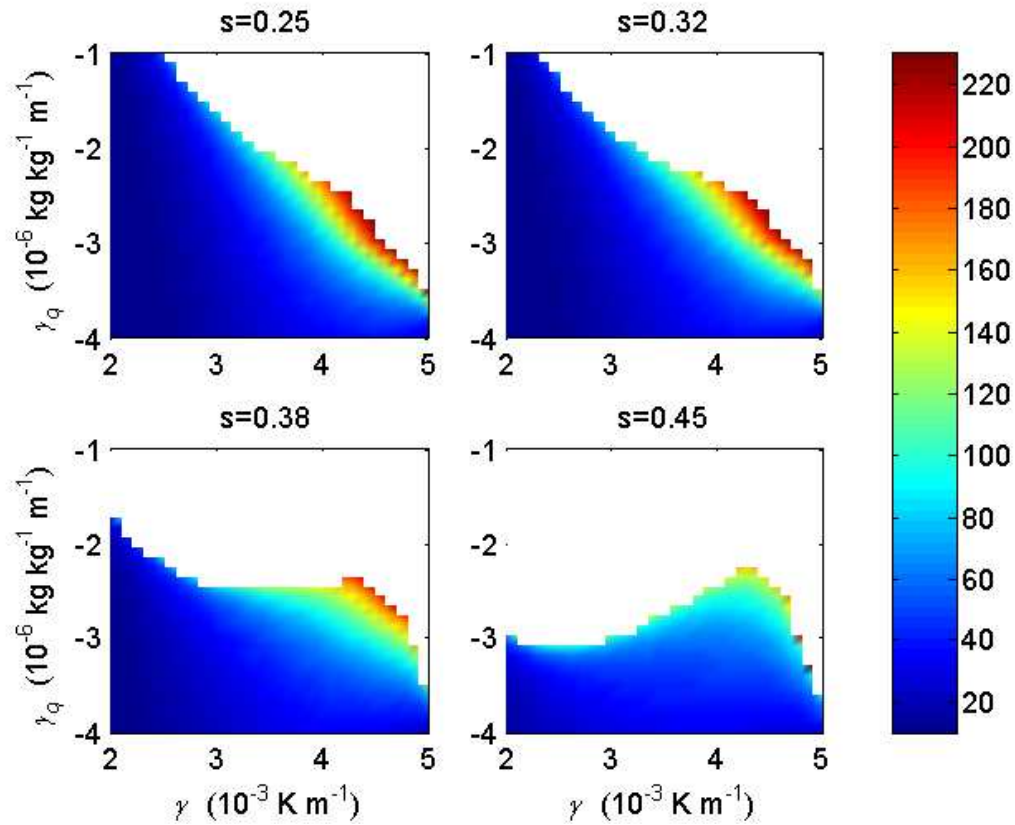


**Figure 24. Time between LCL crossing and cloud breakup as a function of soil moisture and free atmospheric parameters for S1 parametrization ( $\beta_2$ = 0.28 and $(\Delta \theta_v)_{adj} = \Delta_{NT}$ ). The color in the plots represents the minutes after the cloud initiation that cloud-topped boundary layer become unstable and the blank space indicates there is no cloud breakup or LCL crossing.**
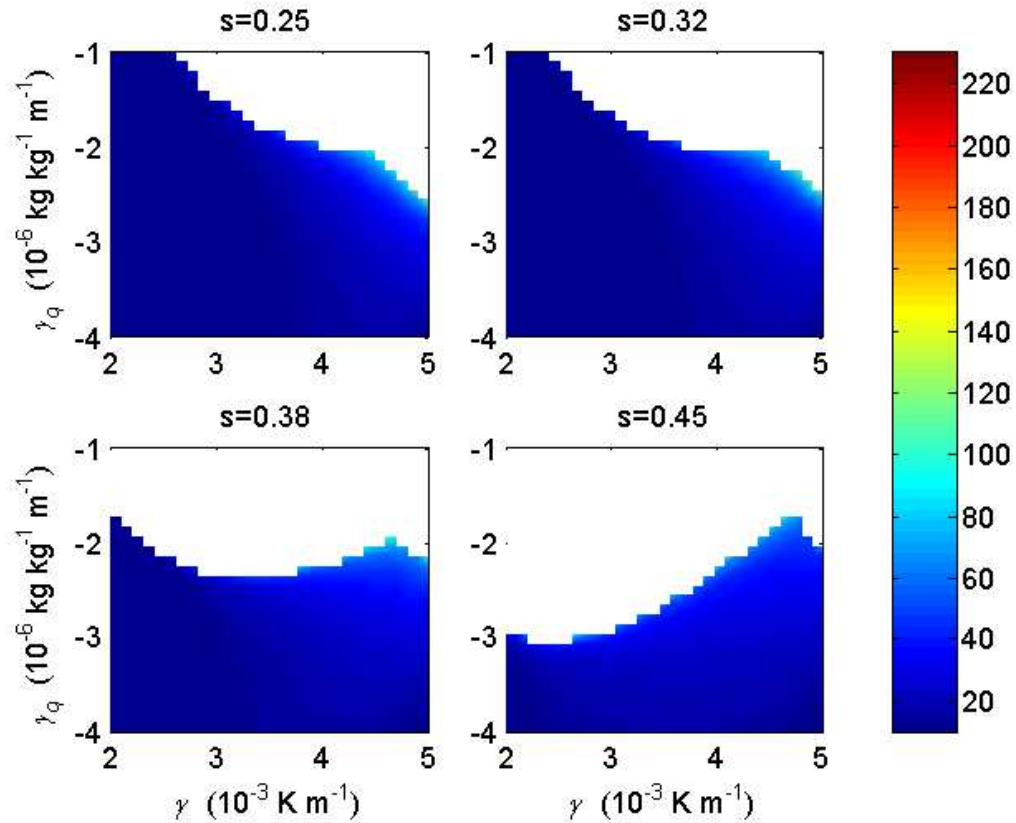
**Figure 25. As in Figure 24, but for S2 parametrization ( $\beta_2$ = 0.63 and $(\Delta\theta_v)_{adj} = \Delta_D$ )**

## *5.4 Transition to cloud dissipation or deep convection*

The preceding section dealt with cloud-topped boundary layer up till the cloud top becomes unstable with remaining unanswered question regarding the following evolution of boundary layer. While the CTEI studies indicate possible cloud dissipation after the cloud top meets the CTEI criteria and becomes unstable (Kuo and Schubert 1988; Yamaguchi and Randall 2008), an unstable cloud-topped boundary layer is also

one of the stage which must be passed by for the transition from shallow to deep convection. In this section, we discuss possible controls that lead to either cloud dissipation or deep convection.

When the cloud top nearly meets the CTEI criteria or $(\Delta\theta_v)_{adj}$ approaches zero, the boundary layer will grow significantly faster according to (80), indicating the value of $dh/dt$ is very large and

$$\xi = \frac{dt}{dh}, \tag{82}$$

becomes small. Substitution of (82) into (69) gives,

$$h\frac{d\theta_L}{dh} = \Delta\theta_L + \xi\left[(\overline{\theta_L'w'})_{sfc} - R_{cool}^l + R_{heat}^s + R_{heat}^l\right]. \tag{83}$$

By applying perturbation theory, the leading order equation for (83) is,

$$h\frac{d\theta_L}{dh} = \Delta\theta_L = \theta_L - \theta_{Lf}(h), \tag{84}$$

which has analytical solution,

$$\theta_L(h) = \frac{\theta_{LR}h_R + \int_{h_R}^{h}\theta_{Lf}(z)dz}{h}, \tag{85}$$

where $h_R$ is the height of boundary layer at the beginning of the transition. Likewise, the leading order equation for total water content is,

$$h\frac{dq_t}{dh} = \Delta q_t = q_t - q_{tf}(h), \tag{86}$$

and its analytical solution is,

$$q_t(h) = \frac{q_{tR}h_R + \int_{h_R}^{h} q_{tf}(z)dz}{h} \,.$$ (87)

From physical point of view, these leading order solutions for boundary-layer

states only account for the cloud-top entrainment while neglect the contribution from

surface heat flux and radiation within the cloud layer due to the short-time transition.

These solutions will then help identify the cloud evolution during the transition period

as analyzed next.

The cloud depth ($h_{cld}$) is defined as the distance from cloud base to the boundary

layer top,

$$h_{cld} = h - z_{LCL} \,.$$ (88)

Differentiating (88) with respect to boundary-layer height shows the change of cloud

depth is closely related to the cloud base dynamics,

$$\frac{dh_{cld}}{dh} = 1 - \frac{dz_{LCL}}{dh} \,.$$ (89)

To further analyze LCL, we focus specific humidity at the LCL, which is saturated and

equals the total specific humidity in the well-mixed boundary layer,

$$q_t = q_{sat} = \varepsilon \frac{e_{sat}(T_{LCL})}{P(z_{LCL})} \,,$$ (90)

where $T_{LCL} = \Gamma_d z_{LCL} + T_0$ is simply the temperature profile of the dry adiabatic process

starting from near-surface temperature $T_0$, which is also equal to the liquid water

potential temperature in the boundary layer $\theta_L$. Differentiating equation (90) with respect to $h$,

$$\frac{dq_t}{dh} = \varepsilon \frac{e_{sat}'(T_{LCL})}{P(z_{LCL})} \frac{d(\Gamma_d z_{LCL} + \theta_L)}{dh} - \varepsilon \frac{e_{sat}(T_{LCL})P'(z_{LCL})}{P^2(z_{LCL})} \frac{dz_{LCL}}{dh}. \tag{91}$$

Using Clausius-Clapeyron equation $de_{sat}/dT = \lambda e_{sat}/(R_v T^2)$, and hydrostatic equation $dP/dz = -Pg/(RT)$,

$$\frac{dq_t}{dh} = \varepsilon \frac{\lambda e_{sat}(T_{LCL})}{P(z_{LCL})R_v T_{LCL}^2} \left( \Gamma_d \frac{dz_{LCL}}{dh} + \frac{d\theta_L}{dh} \right) + \varepsilon \frac{e_{sat}(T_{LCL})g}{P(z_{LCL})RT_{LCL}} \frac{dz_{LCL}}{dh}. \tag{92}$$

Substitution of $q_{sat} = \varepsilon e_{sat}/P$ into (92) gives,

$$\frac{dq_t}{dh} = \left[ \Gamma_d \frac{\lambda q_{sat}}{R_v T_{LCL}^2} + \frac{q_{sat}g}{RT_{LCL}} \right] \frac{dz_{LCL}}{dh} + \frac{\lambda q_{sat}}{R_v T_{LCL}^2} \frac{d\theta_L}{dh}, \tag{93}$$

Substitution of $dz_{LCL}/dh$ in (93) into (89) yields a governing equation for the cloud depth evolution,

$$\frac{dh_{cld}}{dh} = 1 - \frac{\dfrac{dq_t}{dh} - \dfrac{\lambda q_{sat}}{R_v T_{LCL}^2} \dfrac{d\theta_L}{dh}}{\Gamma_d \dfrac{\lambda q_{sat}}{R_v T_{LCL}^2} + \dfrac{q_{sat}g}{RT_{LCL}}}, \tag{94}$$

where $q_{sat}$ equals $q_t$ as indicated in (90). With substitution of (84) and (86) into (94), this governing equation can be used to predict the cloud evolution during the transition period. Specifically, negative $dh_{cld}/dh$ indicates cloud tends to dissipate while positive value suggests cloud tends to grow.

The transition discussed above is under the condition when $(\Delta\theta_v)_{adj}$ is approaching zero, making an unstable cloud top and significantly increase the boundary layer growth. However, small or negative $(\Delta\theta_v)_{adj}$ only allows dry air actively entrain into the cloud layer while development of cumulonimbus from cumulus requires direct force from buoyancy, meaning that cloud need to grow to a certain depth such that boundary layer is above the LFC. After becoming active, the cloud is controlled by convective buoyancy involving strong lateral entrainment and detrainment as discussed next.

## 5.5 Cumulus Dynamics

### 5.5.1 Idealized Parcel Model

In absence of background shear, adverse perturbation pressure gradient, and mixing with surrounding air, the external force on the parcel will is only the buoyancy. The movement of the air parcel is governed by Newton's second law of motion. From Lagrangian viewpoint,

$$\frac{dw}{dt} = B(z),$$
(95)

where $w$ is vertical velocity,

$$\frac{dz}{dt} = w, \tag{96}$$

and $B$ is buoyancy, which is defined as percentage excess of the surrounding virtual potential temperature (or density) over that of the air parcel,

$$B(z) = g \frac{\theta_v(z) - \theta_{v,srd}(z)}{\theta_{v,srd}(z)}. \tag{97}$$

Equations (95) and (96) can be used to plot a phase plane to help explain the air movement in the atmosphere. For example, one specific atmospheric condition is given in Figure 26. There are negative buoyancy between the ABL (around 1 km) and LFC (around 2.5 km) and positive buoyancy between LFC and LNB (around 8 km). Negative buoyancy can also be found above the LNB. These different types of buoyancy will either accelerate or decelerate the air parcel during its adiabatic lifting. The phase plane following (95) and (96) and the specified vertical distribution of buoyancy in Figure 26 is given in Figure 27. As can be seen, an air parcel on the ground with velocity less than $w_1$ cannot overshoot to the LFC and will finally return back the ground. Parcel with speed larger than $w_1$ will overcome CIN and reach to the LNB. This velocity $w_1$ is therefore termed escape speed. Parcel with zero speed from LFC will accelerate to $w_2$ when reaching LNB. For a parcel to move in the reversed direction, the touchdown speed $w_3$ is required to overcome the CAPE to touch the ground. From the symmetrical characteristics of the phase plane, we can expect $w_3$ is the same as $w_2$. Parcel with downward speed less than $w_3$ will not reach the ground but periodically move up and

down around LNB. These characteristic speed $w_1$, $w_2$, and $w_3$ can be found by solving equations (95) and (96). Rewrite (95) as,

$$\frac{dw}{dz}\frac{dz}{dt} = B(z), \tag{98}$$

and substitute (96) into (98),

$$w\frac{dw}{dz} = B(z), \tag{99}$$

which can be integrated analytically from LFC to LNB,

$$w^2\Big|_{LFC}^{LNB} = 2\int_{LFC}^{LNB}B(z)dz = 2CAPE. \tag{100}$$

By assuming the parcel released from LFC has no initial speed, the CAPE speed $w_2$ or touchdown speed $w_3$ can be found as,

$$w_2 = w_3 = \sqrt{2CAPE}. \tag{101}$$

Similarly, the escape speed $w_1$ can be find as,

$$w_1 = \sqrt{2CIN}. \tag{102}$$

This idealized parcel model shows the general concept of CAPE and CIN plays in the atmospheric convection. In reality, cumulus convection is much more complicated due to perturbation pressure, mixing, and water phase change, which we will try to explain next using simplified cumulus dynamic models.
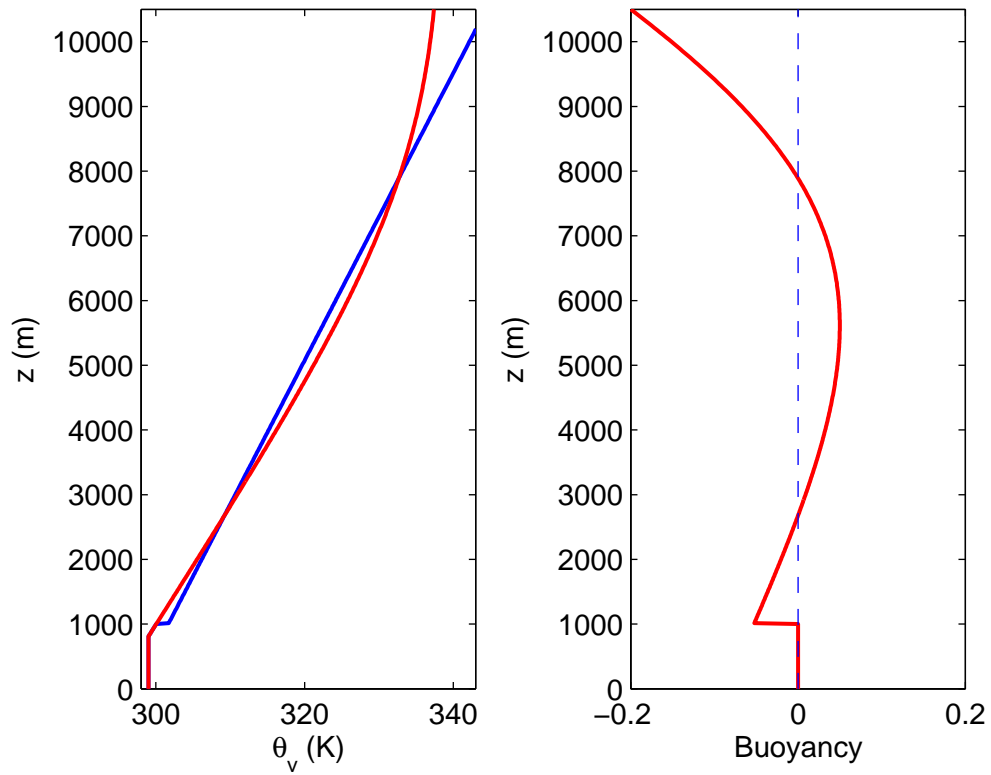
**Figure 26. Atmospheric conditions for analyzing phase plan in Figure 27. The green lines in the left figure are temperature profiles and red lines are the temperature follows moist adiabatic process. The red lines in the right figure are the corresponding buoyancy.**
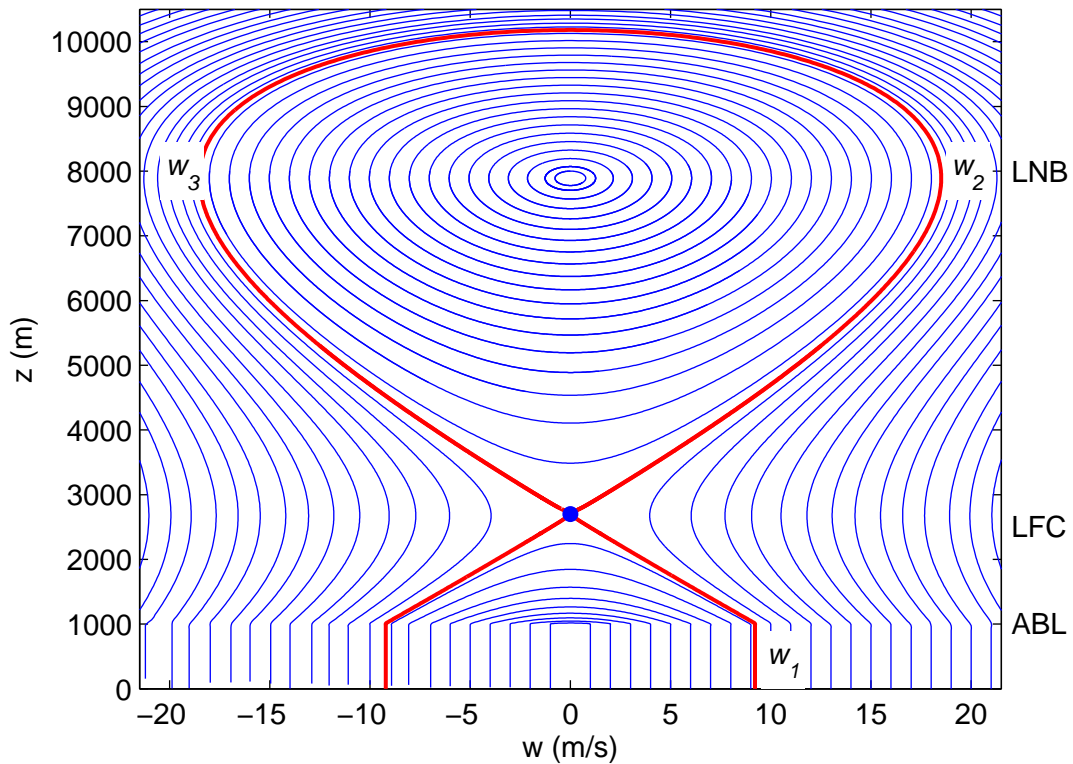
**Figure 27. Phase plane of vertical velocity and height.** $w_1$ **is escape velocity, which is the minimum speed an air parcel needed to escape the LFC and reach the LNB.** $w_2$ **is the CAPE velocity, which is the speed an air parcel can gain if all the CAPE is convert to kinetic energy.** $w_3$ **is touchdown velocity, which is the minimum speed an air parcel needed to overcome the CAPE to hit the ground.**

## 5.5.2 One-dimensional Lagrangian Cumulus Model

In reality, air parcel needs more momentum to overcome the CIN and has less

velocity when overshooting the LNB. In this section, we use the simple one-dimensional

Lagrangian cumulus model to address the background shear, adverse perturbation

pressure gradient, and mixing which are not considered in the previous idealized parcel model.

Considering a rising cloud mixing with surrounding air, (Stommel 1947) suggested some quantity in the cloud $A_{cld}$ can be estimated as,

$$\frac{DA_{cld}}{Dt} = \left(\frac{DA_{cld}}{Dt}\right)_S - \frac{1}{m}\left(\frac{Dm}{Dt}\right)_{ent}(A_{srd} - A_{cld}),\tag{103}$$

where $D/Dt$ indicates the derivative follows the parcel of the fluid, $(DA_{cld}/Dt)_S$ is the rate of change of $A_{cld}$ if it is an adiabatic process, and $1/m(DA_{cld}/Dt)_{ent}$ is lateral entrainment rate. Letting $A$ be the conserved variable $\theta_L$ and vertical velocity, (103) yields,

$$\frac{D\theta_{L,cld}}{Dt} = -\frac{1}{m}\left(\frac{Dm}{Dt}\right)_{ent}(\theta_{L,srd} - A_{L,cld}),\tag{104}$$

and,

$$\frac{Dw_{cld}}{Dt} = -D_R + B - \frac{1}{m}\left(\frac{Dm}{Dt}\right)_{ent}w_{cld},\tag{105}$$

where $B$ is buoyancy and $D_R$ is a parameterization for vertical pressure gradient (Starr Malkus and Scorer 1955). Note that $D/Dt$ can be written as $wD/Dz$ with $w=D\underline{z}/Dt$ as the vertical velocity, equations (104) and (105) are often expressed as,

$$\frac{D\theta_{L,cld}}{Dz} = -\Lambda(\theta_{L,srd} - \theta_{L,cld}),\tag{106}$$

and

$$w\frac{Dw}{Dz} = -D_R + B - \Lambda w^2,\tag{107}$$

where $\Lambda = 1/m(Dm/Dz)_{ent}$. This one-dimensional Lagrangian cloud model can be used to calculate the properties in the cloud if vertical pressure gradient $D_R$ and lateral entrainment $\Lambda$ are available, which are usually obtained by conducting some laboratory experiment (Stommel 1947; Starr Malkus and Scorer 1955; Turner 1962; Ferrier and Houze 1989).

The rising cloud described by the one-dimensional Lagrangian model could not move as fast as the one described by the idealized parcel model. First, the vertical pressure gradient $D_R$ could reduce the momentum of the cloud. Second, some of the rising cloud will evaporate when mixing with the surrounding unsaturated air, leading to the reduction of buoyancy and thus the vertical velocity.

## 5.6 Discrete Cumulus

The previous models do not address the discrete structure of cloud in the atmosphere, which may presented in the form of rolls or cells. However, these patches of cloud usually is the place where strong convections and thunderstorms are often initiated. Unfortunately, the development of these discrete cloud structure is poorly understood due to a lack of observational data and the complicated system of the convective atmosphere. Here, we try to analyze possible feedbacks of these discrete cumulus using the simple mixed-layer model to sense role of vertical motion in the cloud development.

Atmospheric convection always involves vertical air motion, described as updraft or downdraft, which favors or disfavors the boundary-layer development and cloud formation. In some conditions, these two types of air motion is horizontally well-mixed and no particular region could favor cloud formation. In slightly unstable convective conditions, regions can be dominated by either updraft or downdraft, giving rise to horizontal convective rolls. These rolls could evolve into cellular patterns when atmosphere become more unstable.

The onset of convective rolls are often analyzed by the non-dimensional parameter $\varsigma$,

$$\varsigma = \frac{h}{L} = -\frac{khg(\overline{w'\theta_v'})_{sfc}}{\overline{\theta_v}u_*^2} , \tag{108}$$

where $h$ is inversion height and $L$ is Monin Obukhov length. Previous studies have shown that rolls can be found when $h/L$ ranges from -25 to -5 (Etling and Brown 1993; Weckwerth et al. 1997; Miao and Chen 2008). The updraft velocities are usually less than 1 m/s in the convective rolls (Stull 1988) and could be around 1m/s in typical cellular pattern of convection before the cloud become buoyant and active. To qualitatively analyze the influence of vertical motion on the process of cloud formation, here we simply model the updraft velocities ($w_L^u$) in convergence zone as a function of the parameter $\varsigma$ as,

$$w_L^u = \begin{cases} 0 & \varsigma > -5 \\ \left(1 - \dfrac{\varsigma + 25}{20}\right) w_{max} & -25 < \varsigma < -5, \\ w_{max} & \varsigma < -25 \end{cases} \quad (109)$$

Note that equation (109) does not mean there is no vertical velocity for $\varsigma > -5$. The convection under such condition is so weak that no distinguishable updraft or downdraft zone is formed. The constant updraft velocity for $\varsigma < -25$ is only for analysis purpose, under which condition the simulation is already close to the end of cloud formation process.

To model the effects rolls or cells on cloud formation, we focus on a convective roll or cell with distinguishable updraft and downdraft zones, where the corresponding variables are noted with superscripts $u$ and $d$. Due to the air circulation in the updraft and downdraft zones, the conserved variables in each zones are assumed to be equal. Following this assumption, the conservation equation for liquid water potential temperature in (69) can be rewritten as,

$$A\rho c_p \bar{h} \frac{d\theta_L}{dt} = A\rho c_p (\overline{\theta_L ' w'})_{sfc} + A^u \rho c_p \Delta\theta_L^u \frac{dh^u}{dt} + A^d \rho c_p \Delta\theta_L^d \frac{dh^d}{dt} + A^u R_3^u + A^d R_3^d, \quad (110)$$

where $A^u$ and $A^d$ are area of updraft and downdraft zone and $A$ is total area ($A = A^u + A^d$). $R_3$ is the sum of three radiation components in the cloud ($R_{cool}^l$, $R_{heat}^s$, and $R_{heat}^l$), and $\bar{h}$ is the average boundary layer height,

$$\bar{h} = \frac{A^u}{A} h^u + \frac{A^d}{A} h^d. \quad (111)$$

109

The vertical velocity and area satisfy the continuity equation,

$$A_u w_L^u = A_d w_L^d . \qquad (112)$$

Likewise, total water content equation as in (71) can be rewritten as

$$A \rho \bar{h} \frac{dq_t}{dt} = AE + A^u \rho \Delta q_t^u \frac{dh^u}{dt} + A^d \rho \Delta q_t^d \frac{dh^d}{dt} , \qquad (113)$$

Surface heat fluxes in downdraft and updraft zones are influenced by the structure of the discrete cloud and solar zenith angle but could tend to be equal due to the scattering and reflecting of solar lights. For simplicity, only one surface heat flux variable is used in (110) for both zones. The boundary-layer growth rate as in (80) becomes,

$$\frac{dh^u}{dt} (\Delta \theta_v^u)_{adj} = \beta_0 \frac{T_0 u_*^3}{g h^u} + \beta_1 (\overline{w' \theta_v'})_s + \beta_2 \frac{R_{cool}^u}{\rho c_p} + \Delta \theta_v^u w_L^u , \qquad (114)$$

and

$$\frac{dh^d}{dt} (\Delta \theta_v^d)_{adj} = \beta_0 \frac{T_0 u_*^3}{g h^d} + \beta_1 (\overline{w' \theta_v'})_s + \beta_2 \frac{R_{cool}^d}{\rho c_p} + \Delta \theta_v^d w_L^d . \qquad (115)$$

Equations (109)-(115) describe the boundary-layer evolution for both updraft and downdraft regions. An example is shown in Figure 28 where the boundary layer height and cloud depth in updraft zone, downdraft zone, and zones where there is no distinguishable convergence or divergence zone. As can be seen, the convective rolls or cells are initiated about one and a half hour after the sunrise. The updraft momentum helps the boundary layer grow and the downdraft wind suppress the growth of the

boundary layer as simulated by the last term in (114) and (115), leading to the earlier emergence of convective cloud. Since the rolls or cells well mix the air in the convective zones, although the moisture in the downdraft zones does not generate cloud due to the low boundary layer height, the moisture will transfer to the updraft zone to increase the cloud depth in the remote area. These interactions and feedbacks allow the convergent zones generate earlier and deeper discrete cloud.
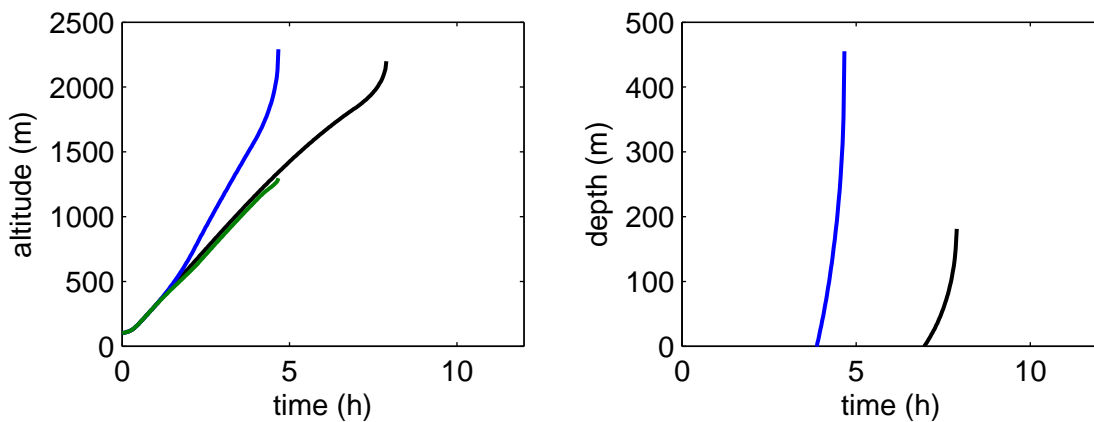


**Figure 28. Boundary-layer height (left) and cloud depth (right) evolution in updraft zone (blue), downdraft zone (green), and in a region where no distinguishable updraft or downdraft zone is formed (black).**

## *5.7 Summary*

In this chapter, we reviewed each component of radiation in the cloud and parametrized the both evaporative and radiative cooling effects on entrainment as upside-down thermal in a similar way as the parameterization of the surface heat flux.

The parameterization of evaporative cooling is closely related to the cloud-top

entrainment instability studied by Randall (1980) and Deardorff (1980). We further used

the cloud-topped boundary layer model to study the transition to either cloud

dissipation or deep convection by analytically expressing the cloud depth as a function

of boundary-layer height. Finally, both idealized and one-dimensional Lagrangian

models are presented to explain the cloud buoyancy and its impacts on the maximum

height reached by a convective cloud.

# 6. Conclusions

In this dissertation, we investigate the land-atmosphere interaction by first statistically analyzing the seasonal variation of soil moisture – rainfall feedback strength (chapter 2), then applying mixed-layer models to interpret diurnal heat flux partitioning and strength of moist convection (chapter 3 and 4), and finally developing cloud-topped mixed-layer models to simulate the boundary-layer dynamics after the cloud formation (chapter 5).

The stochastic water balance model, with the consideration of seasonal variation soil moisture – rainfall feedback, can be used to simulate seasonal transition of soil moisture probabilistic structure. The theoretical model results show periodical transition of soil moisture, which tends to exhibit bimodal behavior until the soil moisture – rainfall feedback strength becomes weak toward the end of the growing season. Greater likelihood of wet-to-wet and dry-to-dry transitions are also observed from spring to summer soil moisture probabilistic structure, indicating the importance of water storage in spring and climatic persistence.

In addition to the statistical analysis of soil moisture – rainfall feedback, mixed-layer models are investigated to explore the essential physics in the complicated system of land-atmosphere interaction. Penman-Monteith approach for the separation of evaporation is adopted in the boundary-layer system and facilitates the derivation of approximate analytical solutions. This method separates the surface latent heat flux as

two components (i.e. equilibrium evaporation and evaporation due to vapor pressure deficit) and further explains their roles in controlling boundary-layer growth.

The mixed-layer model is then coupled with soil-plant-atmosphere continuum models to analyze both the timing of cloud formation and the intensity of moist convection. This pattern of joint behaviors defines four regimes for possible convection in terms of cloud/no-cloud formation and low/high convection intensity. The analysis shows both dry and wet soil can be conducive to early moist convection depends on atmospheric conditions but convection always tends to be stronger under wetter soil conditions.

To overcome the limitation of cloud-free mixed layer models previously used for understanding land-atmosphere interaction, we finally move to cloud-topped boundary layer models, which not only address the change of cloud-top radiation but also connect the cloud-top entrainment instability as defined by Deardorff (1980) and Randall (1980) to the boundary-layer entrainment rate. The transition to either cloud dissipation or deep convection after the top of the boundary layer becomes unstable is theoretically investigated by the evolution of cloud depth, which is closely related to the temperature and humidity states below and above the inversion.

While the cloud-free and cloud-topped mixed-layer models are important for theoretically analyzing the land-atmosphere interaction, we have not yet included advection and large-scale circulation. The boundary layer could have different behaviors

at various locations such as Inter Tropical Convergence Zone (ITCZ) and continental temperate regions, where the convergence/divergence could significantly modify the entrainment rate and further influence the growth of the boundary layer. In the future, we are expecting to develop stochastic mixed layer models and link advection and large-scale circulation to external forcing, which may be associated with slow varying states such as sea surface temperature. These simplified models could help us further understand the complicated climate system in terms of land-ocean-atmosphere interaction, potentially making theoretical contribution to seasonal weather prediction and global climate change modeling.

## Appendix A: Thermodynamic background and definition of pseudoadiabatic processes

Since adiabatic lifting implies no heat exchange between the air parcel and the surrounding atmosphere, the first law of thermodynamics implies that the work done by changing the specific volume of air parcel ($d\alpha$) against the surrounding pressure ($P$) is completely going into internal energy ($c_v dT$),

$$c_v dT = -P d\alpha, \tag{A1}$$

where $c_v$ is the specific heat at constant volume and $dT$ is the change of the temperature. Using the Mayer's relation between specific heats

$$c_p - c_v = R, \tag{A2}$$

where $c_p$ is specific heat at constant pressure and the differential form of the ideal gas law

$$RdT = d(\alpha P) = P d\alpha + \alpha dP, \tag{A3}$$

allows one to write for the dry adiabat,

$$c_p dT = \alpha dP = \frac{1}{\rho_a} dP, \tag{A4}$$

where $c_p dT$ is the change of enthalpy for the perfect gas.

In a moist pseudoadiabatic process, where the heat capacity of liquid water is neglected, the latent heat release from condensed liquid water content ($dq_L$) provides extra enthalpy for the air parcel, so that

$$c_p dT = \frac{1}{\rho_a} dP + \lambda dq_L .$$
(A5)

Since condensation takes place at the saturation curve, $dq_L$ can be expressed as,

$$dq_L = -dq_{sat}(T,P) .$$
(A6)

Using the ideal gas law and substituting (A6) into (A5), one obtains an ordinary

differential equation for the moist pseudoadiabatic process,

$$c_p dT = \frac{RT}{P} dP - \lambda dq_{sat}(T,P) .$$
(A7)

By approximating the gas constant of the air parcel using that of dry air,

$$q_{sat}(T,P) = \frac{R}{R_v} \frac{e_{sat}(T)}{P} \approx \varepsilon \frac{e_{sat}(T)}{P} ,$$
(A8)

where $\varepsilon$ is the ratio of gas constant of dry air to that of water vapor, $e_{sat}$ is saturation

water vapor pressure, which is governed by the parcel temperature following the

relationship described in the Clausius-Clapeyron equation,

$$\frac{de_{sat}}{dT} = \frac{\lambda e_{sat}}{R_v T^2} .$$
(A9)

Differentiating the saturation specific humidity in (A7) with the approximation (A8) and

the Clausius-Clapeyron equation (A9), one can find the temperature change with respect

to pressure  (Emanuel 1994; Tsonis 2002),

$$\frac{dT}{dP} = \frac{1}{P} \frac{RT + \lambda q_s}{c_p + \frac{\lambda^2 q_s}{R_v T^2}} .$$
(A10)

In practice, the adiabatic lapse rate is often expressed as the rate of temperature change with increase in altitude. To obtain these types of lapse rate, one may assume that the surrounding atmosphere is in hydrostatic equilibrium, in which case

$$\frac{dP}{dz} = -\frac{Pg}{RT_{srd}},$$ (A11)

where $T_{srd}$ is the temperature of the surrounding air. With this, assuming the surrounding air and the parcel air have the same temperature (i.e. $T = T_{srd}$) and substituting (A11) into (A4) yields another form of dry adiabatic lapse rate , i.e.,

$$\Gamma_{dry} = \frac{dT}{dz} = -\frac{T}{T_{srd}}\frac{g}{c_p} \approx -\frac{g}{c_p},$$ (A12)

while substituting (A11) into (A10) yields another form of moist pseudoadiabatic lapse rate,

$$\Gamma_{moist} = \frac{dT}{dz} = -\frac{g}{c_p}\frac{RT + \lambda q_s}{1 + \frac{\lambda^2 q_s}{c_p R_v T^2}}\frac{1}{RT_{srd}} \approx -\frac{g}{c_p}\frac{1 + \frac{\lambda q_s}{RT}}{1 + \frac{\lambda^2 q_s}{c_p R_v T^2}}.$$ (A13)

It is worth mentioning that the approximation in equations (A12) and (A13) may become inaccurate due to the assumption of $T_{srd} = T$, especially when the surrounding air and parcel air have significant temperature difference (e.g. atmospheric condition with large CAPE).

# Appendix B: Analytical determination of the LCL evolution

During a dry adiabatic lifting process, no water vapor is condensed and thus the specific humidity of the air parcel remains constant. At the lifting condensation level (LCL), the air parcel just becomes saturated but its specific humidity still equals the initial value ($q_0$),

$$q_{LCL} = \varepsilon \frac{e_{sat}(T_{LCL}(P_{LCL}))}{P_{LCL}} = q_0,$$

(B1)

where $e_{sat}(\bullet)$ the saturation water vapor pressure as a function of temperature can be derived from Clausius-Clapeyron equation. Assuming constant latent heat of vaporization $\lambda$ in (A9), the Clausius-Clapeyron equation can be written in the integrated form as,

$$e_{sat}(T) = e_{sat}(T_{ref}) \exp\left[\frac{\lambda}{R}\left(\frac{1}{T_{ref}} - \frac{1}{T}\right)\right],$$

(B2)

where $T_{ref}$ and $e_{sat}(T_{ref})$ are the reference temperature and the saturation vapor pressure at the reference temperature, respectively. Since the air parcel follows the dry adiabatic process from near-surface initial temperature $T_0$, the temperature at LCL $T_{LCL}(P_{LCL})$ can be found by integrating equation (A4),

$$T_{LCL} = T_0 \left(\frac{P_{LCL}}{P_0}\right)^{R/c_p}.$$

(B3)

Finally, the pressure at the LCL can be analytically solved from equations (B1), (B2), and (B3), yielding the closed form

$$P_{LCL} = \frac{(\lambda R)^{c_p / R}}{\left\{ -c_p R_v T_0 W \left[ -\frac{q_0 \lambda R}{\varepsilon e_{sat}(T_{ref}) c_p R_v T_0} \exp\left( -\frac{\lambda R}{c_p R_v T_{ref}} \right) P_0^{R/c_p} \right] \right\}^{c_p / R}} P_0 ,$$
(B4)

where $W[\bullet]$ is the Lambert W function (Corless et al. 1996). Without any empirical parameters and coefficients, equation (B4) provides an analytical solution for the LCL as a function of near-surface temperature ($T_0$) and humidity ($q_0$), which are assigned as the temperature ($\theta_{BL}$) and humidity ($q_{BL}$) in the boundary layer in this study. This expression can be easily computed using numerical routines and the Lambert W function has been implemented in many software applications such as Maple, GP, Matlab, and Mathematica.

To obtain the altitude of the LCL, one needs to transfer the pressure level to the height level by assuming atmosphere in hydrostatic equilibrium. This one-to-one pressure-altitude relationship can be obtained from (A11) and (A12) by approximating the temperature profiles below the LCL as dry adiabatic profiles,

$$P(z) = P_0 \left( \frac{T(z)}{T_0} \right)^{-\frac{g}{R\Gamma_{dry}}} ,$$
(B5)

with (B5), the altitude of the LCL can be transferred from equations (B4),

$$z_{LCL} = -\frac{T_0}{\Gamma_{dry}} + \frac{\lambda R}{gR_v W\left[\dfrac{\lambda R\Gamma_{dry}}{gR_v T_0}\left(\dfrac{P_0 q_0}{\varepsilon e_{ref}}\right)^{-\frac{R\Gamma_{dry}}{g}} \exp\left(\dfrac{\lambda R\Gamma_{dry}}{gR_v T_{ref}}\right)\right]}.$$

(B6)

# Appendix C: Cloud-Top Entrainment Instability

Cloud-top entrainment instability (CTEI) is a criterion for judging the instability of the cloud top, which was first defined by (Lilly 1968), refined by Randall (1980) and Deardorff (1980) and further developed by Kuo and Schubert (1988), Siems et al. (1990), MacVean and Mason (1990), Duynkerke (1993), Nicholls and Turton (1986) and many others. They show that under certain condition the density of a mixed air from below and above the cloud top with proper mixing fraction $\chi$ can be larger than the air density before the mixing and thus leads to the self-sustained downdraughts.

The nonlinear behaviors of mixing is explained in Figure 29, showing an air parcel (subscript M) is mixed from two air parcels 1 and 2 (subscript 1 and 2). If no water phase is changed during the mixing, the potential temperature and specific humidity of one unit mass of mixed air parcel from $\chi$ unit mass of parcel 2 and 1- $\chi$ unit mass of parcel 1 can be expressed as (Figure 29 a),

$$\theta_M = (1-\chi)\theta_1 + \chi\theta_2 , \qquad (C1)$$

and,

$$q_M = (1-\chi)q_1 + \chi q_2 . \qquad (C2)$$

To the first order approximation, the virtual potential temperature of the mixed air parcel is also a linear combination of the states of the two air parcels (Figure 29 c),

$$\theta_{vM} = (1-\chi)\theta_{v1} + \chi\theta_{v2} . \qquad (C3)$$

If there is water phase change during the mixing, conserved variables such as liquid water potential temperature and total water content should be used in the thermodynamic diagram such that the mixing states will fall on the mixing line as shown in Figure 29 (b) and can be expressed as,

$$\theta_{LM} = (1-\chi)\theta_{L1} + \chi\theta_{L2}, \tag{C4}$$

and,

$$q_{LM} = (1-\chi)q_{L1} + \chi q_{L2}. \tag{C5}$$

However, the virtual potential temperature is no longer conserved during the moist mixing as the evaporative cooling can reduce the temperature of the mixed air parcel. The virtual potential temperature of the mixed air parcel is thus a nonlinear function of mixing fraction $\chi$ and the states of mixing components (i.e. temperature, humidity and pressure states). This nonlinear relationship can be found by implicitly solving equations (C4), (C5), (65), and (66) with Clausius-Clapeyron equation for judging the saturation state of the mixed air parcel,

$$\theta_{vM} = \theta_{vM}(\chi, q_1, q_2, \theta_1, \theta_2, P_M), \tag{C6}$$

where $P_M$ is the surrounding pressure at which the air parcels are mixed. Its approximate analytical function, which assumes $\theta_{vM}$ is constituted of two piecewise linear functions, can be found from (Yamaguchi and Randall 2008) and (Kuo and Schubert 1988). Under some conditions, the mixed air parcel have lower virtual potential

temperature than both the parcel 1 and 2 (Figure 29 d), indicating the mixed air parcel

has heavier density than its corresponding mixing components.
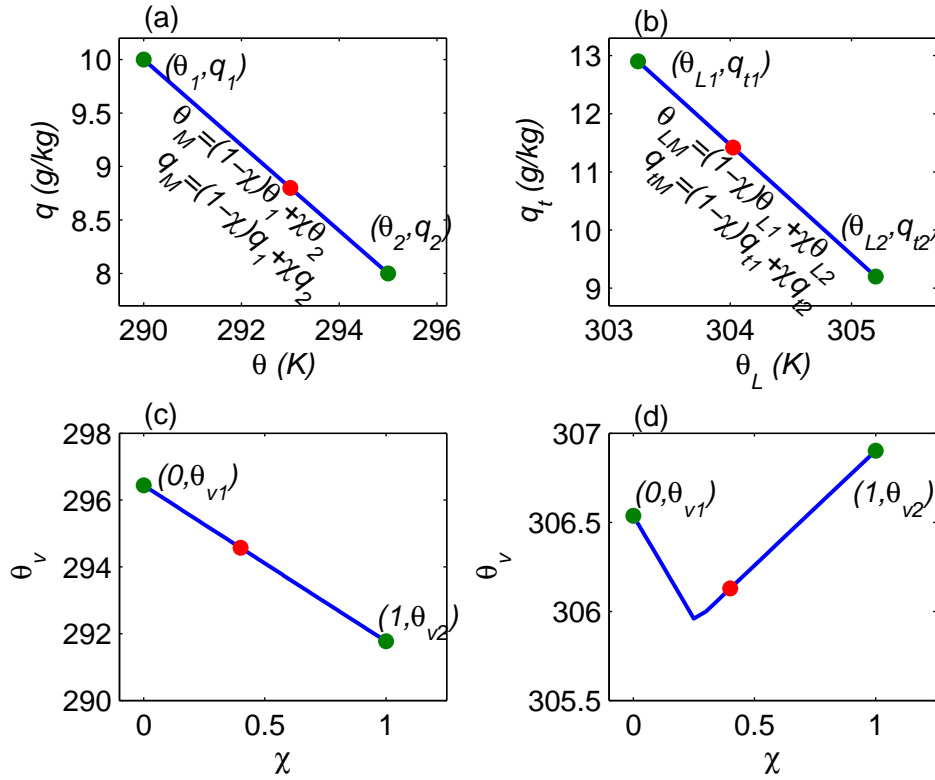


**Figure 29. Thermodynamic diagram (a, b) and virtual potential temperature as a function of mixing fraction (c, d). During the dry mixing process where there is no condensation or evaporation (a, c), temperature and humidity states of the resulting mixture parcel fall on the mixing line. During the moist mixing where there is evaporation (b, d), liquid water potential temperature and total water content are still conserved (b), but the virtual potential temperature shows nonlinear behavior during the mixing (d).**

This air parcel mixing pattern also exists in the boundary-layer top entrainment, where relatively cold and wet air just below the boundary-layer inversion usually mixes with relatively warm and dry air above the inversion. In absence of evaporation or condensation such as in cloud-free boundary layer, the mixed air always has higher virtual potential temperature than the air below the inversion as shown in Figure 29 (c). In the case of the cloud-topped boundary layer, it is likely that under certain condition the light-density air above the inversion after mixing with cloud in certain ratio could have heavier mixed air than the cloud, thus leading to self-sustained downdraughts and an unstable cloud-topped boundary layer. It is possible for cloud-topped boundary layer become dynamic unstable even under the condition that air in the free atmosphere is lighter than the cloud top atmosphere. For this reason, Randall (1980) and Deardorff (1980) defined an unstable cloud-topped boundary layer, given that,

$$\min\{\theta_{vM}(\chi) - \theta_{v1}\} < 0,\tag{C7}$$

where $\theta_{v1}$ is now the virtual potential temperature just below the inversion and $\chi$ is ranged from 0 to 1. This criterion for judging the stability of cloud is termed as could-top entrainment instability (CTEI). However, for typical stratocumulus clouds, $\chi$ needs to be small enough to satisfy (C7) (Albrecht et al. 1985). For this reason, some other criteria have been proposed. For example, by assuming $\chi$ is uniform distributed, Nicholls and Turton (1986) suggested the mixed air should have average virtual potential temperature lower than that of cloud to turn into unstable states,

125

$$\Delta_{NT} = 2 \int_0^1 \left( \theta_{vM}(\chi) - \theta_{v1} \right) d\chi < 0, \tag{C8}$$

where and constant 2 makes $\Delta_{NT} = \Delta \theta_v$ so that it is also valid in the cloud-free boundary layer. By assuming $(\theta_{vM} - \theta_{v1})/\chi$ is uniformly distributed, Duynkerke (1993) suggested the criterion should be,

$$\Delta_D = \int_0^1 \frac{\theta_{vM} - \theta_{v1}}{\chi} d\chi < 0. \tag{C9}$$

All these criteria serves as purpose in judging the stability of cloud-topped boundary layer and are close to the functionality of adjusted buoyancy inversion strength $(\Delta \theta_v)_{adj}$ as defined in (81).

# References

Al-Kaisi, M., L. J. Brun, and J. W. Enz, 1989: Transpiration and evapotranspiration from maize as related to leaf area index. *Agric For Meteorol*, **48,** 111-116.

Albrecht, B. A., R. S. Penc, and W. H. Schubert, 1985: An Observational Study of Cloud-Topped Mixed Layers. *J Atmos Sci*, **42,** 800-822.

Alfieri, L., P. Claps, P. D'Odorico, F. Laio, and T. M. Over, 2008: An analysis of the soil moisture feedback on convective and stratiform precipitation. *J Hydrometeorol*, **9,** 280-291.

Allen, R. G., L. S. Pereira, D. Raes, and M. Smith, 1998: Crop evapotranspiration-Guidelines for computing crop water requirements-FAO Irrigation and drainage paper 56. *FAO, Rome*, **300**.

Ball, F. K., 1960: Control of Inversion Height by Surface Heating. *Q J R Meteorolog Soc*, **86,** 483-494.

Ball, J. T., I. E. Woodrow, and J. A. Berry, 1987: A Model Predicting Stomatal Conductance and its Contribution to the Control of Photosynthesis under Different Environmental Conditions. *Progress in Photosynthesis Research*, J. Biggins, Ed., Springer Netherlands, 221-224.

Battan, L. J., 1973: *Radar observation of the atmosphere.* Univ. of Chicago Press.

Betts, A. K., 1973: Non-precipitating cumulus convection and its parameterization. *Q J R Meteorolog Soc*, **99,** 178-196.

Betts, A. K., 1994: Relation between equilbrium evaporation and the saturation pressure budget. *Boundary Layer Meteorol*, **71,** 235-245.

Betts, A. K., 2009: Land-Surface-Atmosphere Coupling in Observations and Models. *J Adv Model Earth Syst*, **1**.

Betts, A. K., J. H. Ball, A. C. M. Beljaars, M. J. Miller, and P. A. Viterbo, 1996: The land surface-atmosphere interaction: A review based on observational and global modeling perspectives. *J Geophys Res Atmos*, **101,** 7209-7225.

Brubaker, K. L., and D. Entekhabi, 1995: An Analytic Approach to Modeling Land Atmosphere Interaction .1. Construct and Equilibrium Behavior. *Water Resour Res*, **31,** 619-632.

Brutsaert, W., 1998: Land-surface water vapor and sensible heat flux: Spatial variability, homogeneity, and measurement scales. *Water Resour Res*, **34,** 2433-2442.

——, 2005: *Hydrology: an introduction.* Cambridge University Press.

Burke, C. J., 1945: Transformation of Polar Continental Air to Polar Maritime Air. *J Meteor*, **2,** 94-112.

Carson, D. J., 1973: The development of a dry inversion-capped convectively unstable boundary layer. *Q J R Meteorolog Soc*, **99,** 450-467.

Clapp, R. B., and G. M. Hornberger, 1978: Empirical Equations for Some Soil Hydraulic-Properties. *Water Resour Res*, **14,** 601-604.

Corless, R. M., G. H. Gonnet, D. E. G. Hare, D. J. Jeffrey, and D. E. Knuth, 1996: On the LambertW function. *Adv Comput Math*, **5,** 329-359.

D'Odorico, P., and A. Porporato, 2004: Preferential states in soil moisture and climate dynamics. *PNAS*, **101,** 8848-8851.

Daly, E., and A. Porporato, 2007: Intertime jump statistics of state-dependent Poisson processes. *Phys Rev E*, **75,** 011119-011119.

Daly, E., A. Porporato, and I. Rodriguez-Iturbe, 2004: Coupled Dynamics of Photosynthesis, Transpiration, and Soil Water Balance. Part I: Upscaling from Hourly to Daily Level. *J Hydrometeorol*, **5,** 546-558.

De Bruin, H. A. R., 1983: A Model for the Priestley-Taylor Parameter $\alpha$. *Journal of Climate and Applied Meteorology*, **22,** 572-578.

Dean, A. R., R. S. Schneider, R. L. Thompson, J. Hart, and P. D. Bothwell, 2009: The conditional risk of severe convection estimated from archived NWS/Storm Prediction Center mesoscale objective analyses: Potential uses in support of forecast operations and verification. *23rd Conf. on Weather Analysis and Forecasting/19th Conf. on Numerical Weather Prediction*, Omaha, NE, Amer. Meteor. Soc., 6A.5.

Deardorff, J. W., 1980: Cloud Top Entrainment Instability. *J Atmos Sci*, **37,** 131-147.

Dirmeyer, P. A., and K. L. Brubaker, 2007: Characterization of the global hydrologic cycle from a back-trajectory analysis of atmospheric water vapor. *J Hydrometeorol*, **8,** 20-37.

Dominguez, F., P. Kumar, X. Liang, and M. Ting, 2006: Impact of atmospheric moisture storage on precipitation recycling. *J Clim*, **19,** 1513-1530.

Driedonks, A. G. M., 1982: Models and observations of the growth of the atmospheric boundary layer. *Boundary Layer Meteorol*, **23,** 283-306.

Driedonks, A. G. M., and P. G. Duynkerke, 1989: Current problems in the stratocumulus-topped atmospheric boundary layer. *Boundary Layer Meteorol*, **46,** 275-303.

Duynkerke, P. G., 1993: The Stability of Cloud Top with Regard to Entrainment: Amendment of the Theory of Cloud-Top Entrainment Instability. *J Atmos Sci*, **50,** 495-502.

Ek, M., and L. Mahrt, 1994: Daytime Evolution of Relative Humidity at the Boundary-Layer Top. *Mon Weather Rev*, **122,** 2709-2721.

Ek, M. B., and A. A. M. Holtslag, 2004: Influence of Soil Moisture on Boundary Layer Cloud Development. *J Hydrometeorol*, **5,** 86-99.

Eltahir, E. a. B., 1998: A Soil Moisture–Rainfall Feedback Mechanism: 1. Theory and observations. *Water Resour Res*, **34,** 765-765.

Emanuel, K. A., 1994: *Atmospheric convection.* Oxford University Press.

Entekhabi, D., I. Rodriguez-Iturbe, and R. L. Bras, 1992: Variability in large-scale water balance with land surface-atmosphere interaction. *J Clim*, **5,** 798-813.

Etling, D., and R. A. Brown, 1993: Roll vortices in the planetary boundary layer: A review. *Boundary Layer Meteorol*, **65,** 215-248.

Ferguson, I. M., J. A. Dracup, P. B. Duffy, P. Pegion, and S. Schubert, 2010: Influence of SST Forcing on Stochastic Characteristics of Simulated Precipitation and Drought. *J Hydrometeorol*, **11,** 754-769.

Ferrier, B. S., and R. A. Houze, 1989: One-Dimensional Time-Dependent Modeling of GATE Cumulonimbus Convection. *J Atmos Sci*, **46,** 330-352.

Findell, K. L., and E. A. B. Eltahir, 1997: An analysis of the soil moisture-rainfall feedback, based on direct observations from Illinois. *Water Resour Res*, **33,** 725-735.

——, 2003a: Atmospheric controls on soil moisture-boundary layer interactions. Part II: Feedbacks within the continental United States. *J Hydrometeorol*, **4,** 570-583.

——, 2003b: Atmospheric Controls on Soil Moisture–Boundary Layer Interactions. Part I: Framework Development. *J Hydrometeorol*, **4,** 552-569.

Findell, K. L., P. Gentine, B. R. Lintner, and C. Kerr, 2011: Probability of afternoon precipitation in eastern United States and Mexico enhanced by high evaporation. *Nat Geosci*, **4,** 434-439.

Garratt, J. R., 1992: *The atmospheric boundary layer.* Cambridge University Press.

Gentine, P., A. A. M. Holtslag, F. D'Andrea, and M. Ek, 2013: Surface and Atmospheric Controls on the Onset of Moist Convection over Land. *J Hydrometeorol*, **14,** 1443-1462.

Guo, Z., and Coauthors, 2006: GLACE: The Global Land–Atmosphere Coupling Experiment. Part II: Analysis. *J Hydrometeorol*, **7,** 611-625.

Jarvis, P. G., 1976: The Interpretation of the Variations in Leaf Water Potential and Stomatal Conductance Found in Canopies in the Field. *Phil Trans R Soc B*, **273,** 593-610.

Juang, J.-Y., and Coauthors, 2007a: Hydrologic and atmospheric controls on initiation of convective precipitation events. *Water Resour Res*, **43,** W03421.

Juang, J. Y., and Coauthors, 2007b: Eco-hydrological controls on summertime convective rainfall triggers. *Global Change Biol*, **13,** 887-896.

Katul, G., R. Leuning, and R. Oren, 2003: Relationship between plant hydraulic and biochemical properties derived from a steady-state coupled water and carbon transport model. *Plant Cell Environ*, **26,** 339-350.

Kirkpatrick, C., E. W. McCaul Jr, and C. Cohen, 2011: Sensitivities of simulated convective storms to environmental CAPE. *Mon Weather Rev*, **139,** 3514-3532.

Konings, A. G., G. G. Katul, and A. Porporato, 2010: The rainfall-no rainfall transition in a coupled land-convective atmosphere system. *Geophys Res Lett*, **37,** L14401.

Koster, R. D., M. J. Suarez, R. W. Higgins, and H. M. Van den Dool, 2003: Observational evidence that soil moisture variations affect precipitation. *Geophys Res Lett*, **30,** 1241.

Koster, R. D., and Coauthors, 2004: Regions of strong coupling between soil moisture and precipitation. *Science*, **305,** 1138-1140.

Koster, R. D., and Coauthors, 2006: GLACE: The Global Land–Atmosphere Coupling Experiment. Part I: Overview. *J Hydrometeorol*, **7,** 590-610.

Kuo, H.-C., and W. H. Schubert, 1988: Stability of cloud-topped boundary layers. *Q J R Meteorolog Soc*, **114,** 887-916.

Laio, F., A. Porporato, L. Ridolfi, and I. Rodriguez-Iturbe, 2001: Plants in water-controlled ecosystems: active role in hydrologic processes and response to water stress: II. Probabilistic soil moisture dynamics. *Adv Water Resour*, **24,** 707-723.

Laio, F., A. Porporato, L. Ridolfi, and I. Rodriguez-Iturbe, 2002: On the seasonal dynamics of mean soil moisture. *J Geophys Res*, **107,** 4272-4272.

Lilly, D. K., 1968: Models of cloud-topped mixed layers under a strong inversion. *Q J R Meteorolog Soc*, **94,** 292-309.

Lilly, D. K., 2002a: Entrainment into Mixed Layers. Part I: Sharp-Edged and Smoothed Tops. *J Atmos Sci*, **59,** 3340-3352.

——, 2002b: Entrainment into Mixed Layers. Part II: A New Closure. *J Atmos Sci*, **59,** 3353-3361.

Lock, A. P., 1998: The parametrization of entrainment in cloudy boundary layers. *Q J R Meteorolog Soc*, **124,** 2729-2753.

Lock, A. P., and M. K. Macvean, 1999: The parametrization of entrainment driven by surface heating and cloud-top cooling. *Q J R Meteorolog Soc*, **125,** 271-299.

Lyons, T. J., 2002: Clouds prefer native vegetation. *Meteorol Atmos Phys*, **80,** 131-140.

MacVean, M. K., and P. J. Mason, 1990: Cloud-Top Entrainment Instability through Small-Scale Mixing and Its Parameterization in Numerical Models. *J Atmos Sci*, **47,** 1012-1030.

Mahmood, R., and Coauthors, 2014: Land cover changes and their biogeophysical effects on climate. *Int J Climatol*, **34,** 929-953.

McNaughton, K. G., 1976: Evaporation and advection I: evaporation from extensive homogeneous surfaces. *Q J R Meteorolog Soc*, **102,** 181-191.

Miao, S., and F. Chen, 2008: Formation of horizontal convective rolls in urban areas. *Atmos Res*, **89,** 298-304.

Moeng, C.-H., P. P. Sullivan, and B. Stevens, 1999: Including Radiative Effects in an Entrainment Rate Formula for Buoyancy-Driven PBLs. *J Atmos Sci*, **56,** 1031-1049.

Muller, C. J., L. E. Back, P. A. O'Gorman, and K. A. Emanuel, 2009: A model for the relationship between tropical precipitation and column water vapor. *Geophys Res Lett*, **36,** L16804-L16804.

Nicholls, S., and J. D. Turton, 1986: An observational study of the structure of stratiform cloud sheets: Part II. Entrainment. *Q J R Meteorolog Soc*, **112,** 461-480.

Pelly, J. L., and S. E. Belcher, 2001: A Mixed-Layer Model Of The Well-Mixed Stratocumulus-Topped Boundary Layer. *Boundary Layer Meteorol*, **100,** 171-187.

Pielke, R. A., and Coauthors, 2007: An overview of regional land-use and land-cover impacts on rainfall. *Tellus B*, **59,** 587-601.

Pielke, R. A., and Coauthors, 2011: Land use/land cover changes and climate: modeling analysis and observational evidence. *Wiley Interdiscip Rev Clim Change*, **2,** 828-850.

Pinty, J.-P., P. Mascart, E. Richard, and R. Rosset, 1989: An investigation of Mesoscale Flows Induced by Vegetation Inhomogeneities Using an Evapotranspiration Model Calibrated Against HAPEX-MOBILHY Data. *J Appl Meteorol*, **28,** 976-992.

Pitman, A. J., 2003: The evolution of, and revolution in, land surface schemes designed for climate models. *Int J Climatol*, **23,** 479-510.

Porporato, A., 2009: Atmospheric Boundary-Layer Dynamics with Constant Bowen Ratio. *Boundary Layer Meteorol*, **132,** 227-240.

Porporato, A., and P. D'Odorico, 2004: Phase Transitions Driven by State-Dependent Poisson Noise. *Phys Rev Lett*, **92,** 110601.

Priestley, C. H. B., and R. J. Taylor, 1972: On the Assessment of Surface Heat Flux and Evaporation Using Large-Scale Parameters. *Mon Weather Rev,* **100,** 81-92.

Randall, D. A., 1980: Conditional Instability of the First Kind Upside-Down. *J Atmos Sci,* **37,** 125-130.

Raupach, M. R., 2001: Combination theory and equilibrium evaporation. *Q J R Meteorolog Soc,* **127,** 1149-1181.

Rigby, J. R., J. Yin, J. Albertson, and A. Porporato, 2015: Approximate Analytical Solution to Diurnal Atmospheric Boundary-Layer Growth Under Well-Watered Conditions. *Boundary Layer Meteorol,* **156,** 73-89.

Rodriguez-Iturbe, I., D. Entekhabi, and R. L. Bras, 1991: Nonlinear Dynamics of Soil Moisture at Climate Scales 1. Stochastic Analysis. *Water Resour Res,* **27,** 1899-1906.

Rodríguez-Iturbe, I., and A. Porporato, 2005: *Ecohydrology of water-controlled ecosystems: soil moisture and plant dynamics.* Cambridge University Press.

Rogers, D. P., J. A. Businger, and H. Charnock, 1985: A numerical investigation of the JASIN atmospheric boundary layer. *Boundary Layer Meteorol,* **32,** 373-399.

Salvucci, G. D., J. A. Saleem, and R. Kaufmann, 2002: Investigating soil moisture feedbacks on precipitation with tests of Granger causality. *Adv Water Resour,* **25,** 1305-1312.

Santanello, J. A., M. A. Friedl, and W. P. Kustas, 2005: An Empirical Investigation of Convective Planetary Boundary Layer Evolution and Its Relationship with the Land Surface. *J Appl Meteorol,* **44,** 917-932.

Santanello, J. A., C. D. Peters-Lidard, S. V. Kumar, C. Alonge, and W.-K. Tao, 2009: A Modeling and Observational Framework for Diagnosing Local Land–Atmosphere Coupling on Diurnal Time Scales. *J Hydrometeorol,* **10,** 577-599.

Savenije, H. H. G., 1995: New definitions for moisture recycling and the relationship with land-use changes in the Sahel. *J Hydrol,* **167,** 57-78.

Scanlon, T. M., and J. D. Albertson, 2004: Canopy scale measurements of CO2 and water vapor exchange along a precipitation gradient in southern Africa. *Global Change Biol,* **10,** 329-341.

Schubert, S. D., M. J. Suarez, P. J. Pegion, R. D. Koster, and J. T. Bacmeister, 2008: Potential predictability of long-term drought and pluvial conditions in the US Great Plains. *J Clim*, **21,** 802-816.

Shao, Q., D. A. Randall, C.-H. Moeng, and R. E. Dickinson, 1997: A method to determine the amounts of cloud-top radiative and evaporative cooling in a stratocumulus-topped boundary layer. *Q J R Meteorolog Soc*, **123,** 2187-2213.

Siems, S. T., C. S. Bretherton, M. B. Baker, S. Shy, and R. E. Breidenthal, 1990: Buoyancy reversal and cloud-top entrainment instability. *Q J R Meteorolog Soc*, **116,** 705-739.

Silverman, B. W., 1981: Using kernel density estimates to investigate multimodality. *Journal of the Royal Statistical Society. Series B*, **43,** 97-99.

Siqueira, M., G. Katul, and A. Porporato, 2009: Soil Moisture Feedbacks on Convection Triggers: The Role of Soil–Plant Hydrodynamics. *J Hydrometeorol*, **10,** 96-112.

Stage, S. A., and J. A. Businger, 1981: A Model for Entrainment into a Cloud-Topped Marine Boundary Layer. Part I: Model Description and Application to a Cold-Air Outbreak Episode. *J Atmos Sci*, **38,** 2213-2229.

Starr Malkus, J., and R. S. Scorer, 1955: THE EROSION OF CUMULUS TOWERS. *J Meteor*, **12,** 43-57.

Stéfanon, M., P. Drobinski, F. D'Andrea, C. Lebeaupin-Brossier, and S. Bastin, 2013: Soil moisture-temperature feedbacks at meso-scale during summer heat waves over Western Europe. *Clim Dyn*.

Stephens, G. L., 1978: Radiation Profiles in Extended Water Clouds. II: Parameterization Schemes. *J Atmos Sci*, **35,** 2123-2132.

Stommel, H., 1947: ENTRAINMENT OF AIR INTO A CUMULUS CLOUD. *J Meteor*, **4,** 91-94.

Stull, R. B., 1976: The Energetics of Entrainment Across a Density Interface. *J Atmos Sci*, **33,** 1260-1267.

Stull, R. B., 1988: *An introduction to boundary layer meteorology.* Kluwer Academic Publishers.

Taylor, C. M., R. A. M. de Jeu, F. Guichard, P. P. Harris, and W. A. Dorigo, 2012: Afternoon rain more likely over drier soils. *Nature*, **489,** 423-426.

Tennekes, H., 1973: A Model for the Dynamics of the Inversion Above a Convective Boundary Layer. *J Atmos Sci*, **30,** 558-567.

Teuling, A. J., R. Uijlenhoet, and P. A. Troch, 2005: On bimodality in warm season soil moisture observations. *Geophys Res Lett*, **32,** L13402-L13402.

Tsonis, A. A., 2002: *An introduction to atmospheric thermodynamics.* Cambridge University Press.

Turner, J. S., 1962: The 'starting plume' in neutral surroundings. *Journal of Fluid Mechanics*, **13,** 356-368.

Weckwerth, T. M., J. W. Wilson, R. M. Wakimoto, and N. A. Crook, 1997: Horizontal Convective Rolls: Determining the Environmental Conditions Supporting their Existence and Characteristics. *Mon Weather Rev*, **125,** 505-526.

Yamaguchi, T., and D. A. Randall, 2008: Large-Eddy Simulation of Evaporatively Driven Entrainment in Cloud-Topped Mixed Layers. *J Atmos Sci*, **65,** 1481-1504.

Yin, J., A. Porporato, and J. Albertson, 2014: Interplay of climate seasonality and soil moisture-rainfall feedback. *Water Resour Res*, **50,** 6053-6066.

Zhang, M., and Coauthors, 2013: CGILS: Results from the first phase of an international project to understand the physical mechanisms of low cloud feedbacks in single column models. *J Adv Model Earth Syst*, **5,** 826-842.

# Biography

Jun Yin was born in Guangde, Anhui, China. He earned a Bachelor of Science degree in water conservancy and hydropower engineering and a Master of Science degree in Hydrology and Water Resources from Zhengzhou University in 2006 and 2009. Jun Yin began his Ph.D. study with Professor John Albertson and Professor Amilcare Porporato in the Department of Civil and Environmental Engineering at Duke University in the fall of 2009.